

Successive laser crystallization of doped and undoped *a*-Si:H

vorgelegt von
Dipl.-Phys. Philipp Lengsfeld
aus Berlin

Vom Fachbereich 4 (Physik)
der Technischen Universität Berlin
zur Erlangung des akademischen Grades
Doktor der Naturwissenschaft
-Dr. rer. nat.-
genehmigte Dissertation

Berlin 2001

D 83

Tag der Einreichung der Dissertation: 14. Dezember 2000

Tag der wissenschaftlichen Aussprache: 5. April 2001

Promotionsausschuss:

Vorsitzender:	Prof. Dr. Dieter Zimmermann
1. Bericht:	Prof. Dr. Wolfgang Richter
2. Bericht:	Prof. Dr. Walther Fuhs

Table of contents

ZUSAMMENFASSUNG.....	5
1 INTRODUCTION.....	7
2 EXCIMER LASER CRYSTALLIZATION.....	11
2.1 General features of excimer lasers.....	11
2.2 The three crystallization regimes.....	12
3 EXPERIMENTAL	15
3.1 Starting material.....	15
3.2 Laser crystallization.....	17
3.3 Characterization methods.....	19
3.4 Raman spectroscopy	22
4 TERMINOLOGY OF THIN FILM SILICON MODIFICATIONS.....	25
5 RESULTS	29
5.1 Successive crystallization.....	29
5.2 Structural properties of undoped poly-Si	40
5.3 Influence of doping on the crystallization process and resulting material.....	58
6 DISCUSSION	79
6.1 Si-H dissociation during successive crystallization	79
6.2 Structure of laser crystallized poly-Si	86
6.3 Raman spectra of heavily doped poly-Si: Fano effect revisited	91
7 SUMMARY	103
8 REFERENCES.....	105

Zusammenfassung

In dieser Arbeit werden die sukzessive Laserkristallisierung von undotiertem und dotiertem amorphen Silizium und die Eigenschaften der resultierenden Schichten untersucht. Die wichtigsten Ergebnisse sind:

- Im Zuge der sukzessiven Kristallisierung entsteht ein 2-Schichtsystem. Von der Oberfläche erstreckt sich eine kristallisierte Schicht in den Film. Die Kristallinität dieser oberen Schicht zeigt eine starke Tiefenabhängigkeit. An der Grenze zum Substrat verbleibt eine amorphe Restschicht.
- Die sukzessive Kristallisierung ist verbunden mit einer Dehydrogenisierung der Proben. Im Zuge dieser Dehydrogenisierung nimmt die Si-H-Bande bei 2000 cm^{-1} schneller ab als die Wasserstoffbande bei 2100 cm^{-1} . Vollständig kristallisierte Proben können noch bis zu 4 at. % Wasserstoff enthalten.
- Die schnellere Abnahme der Si-H-Bande kann mit der Annahme erklärt werden, dass in amorphem Silizium hoher Qualität die Wasserstoffbande bei 2100 cm^{-1} durch platelet-artige Wasserstoffcluster erzeugt wird. In diesen Clustern ist der Wasserstoff stärker gebunden als in Si-H-Bindungen.
- Undotiertes polykristallines Silizium (poly-Si), hergestellt mit sukzessiver Laserkristallisierung im super lateral growth- (SLG)-Regime, hat Korngrößen im Bereich $3\text{-}4\text{ }\mu\text{m}$ und besitzt eine geringe Rauigkeit. Die Versetzungsdichte ist in den meisten Körnern gering. Die Körner haben eine $\{111\}$ -Vorzugsorientierung in Richtung der Oberflächennormale. Die Körner von poly-Si, welches außerhalb des SLG-Regimes kristallisiert wurde, besitzen keine Vorzugsorientierung. Die Texturbildungsmechanismen werden mit Hilfe eines Modells erklärt, das ursprünglich für die Festphasenkristallisierung entwickelt wurde. Laut Ramanmessungen sind die laserkristallisierten Schichten verspannt.
- Die Dotierung des Ausgangsmaterials hat einen erheblichen Einfluss auf den Kristallisationsprozess. Durch starke P-Dotierung wird die Schwellenergie der Kristallisierung und die Laserenergie zur Erreichung des SLG-Regimes verringert.

Im Falle der B-Dotierung werden diese beiden charakteristischen Kristallisierungsparameter erhöht. Die Ursache für diese Beeinflussung des Kristallisierungsprozesses liegt wahrscheinlich in einer Änderung der thermischen Eigenschaften der Proben begründet.

- Stark dotierte poly-Si Proben, kristallisiert im SLG-Regime, zeigen ebenfalls eine {111}-Vorzugsorientierung der Körner. Die freien Ladungsträgerkonzentrationen in hochdotierten Proben sind größer als $5 \times 10^{20} \text{ cm}^{-3}$.
- Die hohe Konzentration freier Ladungsträger hat starke Auswirkungen auf die Ramanspektren der poly-Si Proben. Die LO-TO-Phononenlinie wird auf Grund des Fano-Effekts asymmetrisch verbreitert.
- Die Ramanspektren von stark B dotiertem mikrokristallinem Silizium ($\mu\text{-Si}$) zeigen nicht die für hochdotiertes p-Typ poly-Si typische Fanoverbreiterung.

1 Introduction

Polycrystalline silicon (poly-Si) is viewed as a very attractive material for thin film electronic devices. Research and development of poly-Si presently concentrates on two objectives. The first is to use poly-Si thin film transistors (TFT's) in active matrix liquid crystal displays (AMLCD's) [1]. On the other hand, a growing interest is directed to the development of high-efficiency low-cost poly-Si thin film solar cells [2]. In both cases the aim is to fabricate the devices on low-cost substrates such as glass or plastics. This choice of substrates limits the process temperature to < 600 °C. The key factor for the attractiveness of poly-Si is the large grain size, in case of TFT applications [1] as well as for photovoltaic applications, where large-grained material seems to be mandatory to achieve silicon solar cell efficiencies in the range of 15 % and above [2].

In order to fabricate poly-Si with a lateral grain size exceeding 500 nm at low process temperatures it is necessary to employ some sort of crystallization method. The typical starting material for the crystallization process is amorphous silicon (*a*-Si) or hydrogenated amorphous silicon (*a*-Si:H) which can be deposited at low temperature by various deposition techniques such as plasma enhanced chemical vapor deposition (PECVD), low-pressure chemical vapor deposition (LPCVD) or sputtering. The details on preparation and properties of *a*-Si and *a*-Si:H can be found in Refs. [3-5]. Two common approaches to crystallize *a*-Si are solid phase crystallization (SPC) [6, 7] and metal induced crystallization (MIC) [8]. SPC is based on isothermal annealing of *a*-Si at temperatures of about 600 °C. MIC is based on the effect that certain metals in contact with amorphous silicon induce the transformation from the amorphous to the crystalline phase at temperatures well below the eutectic temperature of the metal-silicon system. A review of MIC is given in Ref. [9]. SPC and MIC can produce thin film poly-Si on foreign substrates with large grains [7, 10, 11]. However, SPC suffers from long processing times and a large dislocation density in the grains [2, 12]. In case of MIC the intrinsic doping of the silicon during the process imposes considerable restrictions on possible device applications.

A presently widely used method to prepare poly-Si on foreign substrates is laser crystallization. Laser crystallization is a much faster process than SPC and MIC and can produce large grained poly-Si with a low dislocation density, see e.g. [13]. The basic principle of laser crystallization is the transformation from amorphous to crystalline silicon by melting the silicon for a very short time. Poly-Si with large grains results from the subsequent solidification. A general review of laser crystallization of semiconductors is given in Ref. [14]. Strictly speaking, laser crystallization is not a low temperature process as the silicon is heated well above 900 °C. However, the high temperatures are only sustained for a very short time. Due to the short time scale the thermal strain on the low-temperature substrates does not lead to severe damage or destruction of these substrates.

Laser crystallization of amorphous silicon has been a subject of intense research for a considerable time. A widely discussed subject was, for instance, the appearance and mechanisms of explosive crystallization [15]. Laser crystallization of *a*-Si can be performed using a variety of lasers and different techniques [16-18]. However, excimer laser crystallization (ELC) is by far the most widely used method at the moment [13, 19, 20]. The principal advantage of excimer lasers is the strong absorption of UV light in silicon. In consequence, most of the laser energy is deposited close to the surface of the thin film and the thermal strain on the substrate is much lower than in case of lasers with longer wavelength [21]. The basic transformation processes for excimer laser crystallization are divided into three crystallization regimes depending on the applied laser fluences and are relatively well understood [19, 22, 23]. The basic features of excimer laser crystallization and the existing models on the transformation process will be reviewed in section 2.

There are still a number of unsolved questions regarding the laser crystallization process and the properties of the resulting poly-Si. One of these questions is the role of hydrogen in the laser crystallization process. Usually, hydrogen which can be present in the starting material amorphous silicon is regarded as incommodious by the groups who perform laser crystallization, as the explosive outdiffusion of hydrogen during the crystallization process can damage the films. Therefore, hydrogen is usually removed prior to laser crystallization by annealing the films in a conventional vacuum furnace. On the other hand, the question of hydrogen in disordered silicon has been a major field of re-

search in the last decades [24]. Post-hydrogenation of poly-Si significantly reduces the defect density in the material [25]. Mei *et al.* introduced the successive crystallization procedure which can be employed for the crystallization of *a*-Si:H films containing large amounts of hydrogen without a preannealing step [26]. In this work this successive crystallization method is reexamined in order to gain more insight into the problem of how hydrogen is involved in the crystallization process and what can be learned about the question of hydrogen bonding in disordered silicon.

The technological aim of our group is to produce large-grained poly-Si which can be used as a back contact layer in solar cells and at the same time serve as a seeding layer for a subsequent low-temperature Si homoepitaxy [2]. In order to achieve this, it is not only necessary to determine the grain size of the poly-Si. The questions of what types of grain boundaries separate the grains and what kind of orientation the grains possess are also of fundamental importance. Since low-temperature Si homoepitaxy strongly depends on the orientation of the wafer (see, e. g. [27] and references therein) the orientation of the grains of the poly-Si is a crucial question with regard to the envisaged application. A contact layer in a solar cell has to be doped. Therefore, the influence of doping on the crystallization process is also of interest. All these questions will be treated in detail in this work and a model for the texture formation in case of excimer laser crystallization will be given.

Raman spectroscopy is a standard characterization method in the field of thin film silicon [5]. Therefore, this method was extensively used in this work. The investigation of heavily doped laser crystallized samples with Raman spectroscopy revealed some very interesting features which were known to occur in crystalline silicon [28-30] but whose relevance for the field of thin film silicon especially regarding the differences between microcrystalline silicon ($\mu\text{c-Si}$) and poly-Si were up to now not fully recognized. The Raman measurements on heavily doped poly-Si and $\mu\text{c-Si}$ and the interpretation of the observed asymmetric broadenings of the phonon line shape in terms of Fano resonances [31] in the case of poly-Si are the last main topic of this work. The results add a new aspect to the controversy whether $\mu\text{c-Si}$ with a high crystallinity and poly-Si are different materials, or not. It will be shown that there are indeed fundamental differences between $\mu\text{c-Si}$ and poly-Si. Raman spectra of heavily doped samples can provide a tool for the distinction between poly-Si and $\mu\text{c-Si}$.

2 Excimer laser crystallization

In this chapter the general features of excimer lasers and the existing knowledge of the transformation kinetics of the excimer crystallization process will be reviewed.

2.1 General features of excimer lasers

Excimer lasers are the most effective and powerful UV light sources available today. To generate excimer laser radiation, a transient high voltage discharge is produced in a tube containing the laser gas. According to the gas used, laser radiation is obtained at wavelengths between 157 - 351 nm (Table 2.1). All excimer lasers are pulsed lasers.

Table 2.1: Different excimer laser gases and their wavelength λ .

Laser gas	XeF	XeCl	KrF	KrCl	ArF	F ₂
λ (nm)	351	308	248	222	193	157

For the crystallization process the essential advantage of an excimer laser is the strong absorption of the UV light in silicon. In case of $\lambda = 308$ nm the penetration depth is about 8 nm for amorphous and crystalline silicon. Thus, in contrast to IR laser crystallization or conventional furnace annealing all the absorbed energy is deposited in the film close to the surface. In addition, due to the short excimer laser pulse width, which typically ranges from 20 ns to 50 ns, the silicon film is rapidly heated above the melting point and solidifies quickly. Typical solidification times are on the order of some hundred nanoseconds. Thus, the time scale of the thermal strain on the substrate is very short. Therefore, excimer laser crystallization provides a process that is compatible with low-temperature glass substrates as well as other temperature sensitive materials, such as plastics. In addition, excimer laser crystallization is also well suited to produce hybrid amorphous and poly-Si material in close proximity [32, 33]. Due to the rapid heat up and cool down of the process neighboring material and devices can maintain their

integrity while selected regions are being crystallized. In addition to crystallization, excimer laser processing is used to fabricate contact layers for devices such as thin film transistors (TFT's) [13].

2.2 The three crystallization regimes

Due to the advantageous features of excimer laser crystallization regarding possible device fabrication a lot of work has been done to study the kinetics and the transformation mechanisms of the process. Previous studies on the details of the transformation scenarios show that excimer laser crystallization of amorphous and crystalline silicon films on foreign substrates divides into three transformation regimes with respect to the applied laser fluence [19]. These are the low and high energy density regimes and in between those two, the so-called super lateral growth (SLG) regime.

Low energy density regime (partial melting)

The low energy density regime describes the situation when the incident energy density of the laser pulse is sufficient to induce melting of the amorphous or crystalline silicon films. The laser fluence E_L is larger than the threshold energy of crystallization E_T but is low enough that a continuous layer of solid Si remains at the maximum extend of primary melting. Therefore, this energy range is also referred to as the partial melting regime. For irradiation of amorphous silicon (*a*-Si) it is characterized by a combination of explosive crystallization [15] and vertical solidification. Explosive crystallization can be triggered at the onset, or near the end of melting depending on the presence or absence of microcrystals, respectively. Typical grain sizes on the order of up to twice the film thickness can be achieved [13].

High energy density regime (complete melting)

In the high energy density regime the incident energy density is sufficiently high to lead to a complete melting of the film. Hence, this energy range is also referred to as the complete melting regime. Epitaxial regrowth from the substrate is not possible due to

the amorphous structure of the glass. Experimentally, it is observed that the grain size of the films crystallized in this regime is less than 200 nm [13]. A widely used explanation for this behavior assumes that a deep supercooling of the melt leads to homogeneous nucleation [34]. The deep supercooling is caused by (i) an extremely rapid cooling of the liquid Si (l-Si), (ii) the relatively ineffective role which the l-Si/SiO₂ interface plays in terms of catalyzing heterogeneous nucleation of crystalline Si [35, 36], (iii) the statistical nature of nucleation, and (iv) the small volumes associated with the thin films. The theory of the spontaneous nucleation in a supercooled melt as an explanation for the crystallization mechanism in the complete melting regime is not yet universally accepted in the literature. Another explanation is a dramatic increase in the number of nucleation sites due to surface damage and roughening of the substrate [37-39]. However, recent detailed work by Hatano *et al.*, who investigated the excimer laser crystallization process by employing various *in situ* methods supports the model of the homogeneous nucleation in a supercooled melt [40].

Super lateral growth regime (near complete melting)

Im *et al.* identified the third transformation regime in a narrow experimental window at the transition between the two major regimes [22, 23]. Crystallization in this energy range leads to the formation of large-grained polycrystalline silicon [22, 39, 41-44], with grain sizes many times larger than the film thickness. The transformation scenario associated with this regime was described in terms of a near-complete melting of the silicon [22, 23, 42]. In this model, it is argued that at the maximum point of melting the unmelted portion of the underlying Si no longer forms a continuous layer but instead consists of islands of solid that are separated by small local regions of completely molten silicon. The unmelted islands act as solidification seeds [22, 23], from which a lateral grain growth commences. This energy range is also referred to as the near-complete melting regime. The resulting grain size can exceed the film thickness by up to a factor of 30. Since the grain size is much larger than in the two major transformation regimes, Im and Kim [23] coined the name *super lateral growth* regime.

Ultimately, the maximum extend to which the lateral growth can proceed is limited by nucleation. It follows that laterally growing fronts originating from the unmelted solids

can only meet and form grain boundaries if the seeds are sufficiently closely located to each other so that nucleation is avoided. According to the SLG model, the following factors are responsible for determining the extend of lateral growth (SLG distance). The SLG distance will increase with increasing film thickness, increasing substrate temperature, decreasing thermal conductivity of the substrate, and increasing laser pulse duration [23]. It has been shown that the energy density to achieve super lateral growth E_{SLG} increases with increasing film thickness, increasing pulse duration, increasing thermal conductivity of the substrate, decreasing substrate temperature, and increasing concentration of microcrystals in as-deposited amorphous silicon [23].

3 Experimental

This chapter contains a brief review of the experimental methods used in this work. It starts with the description of how the starting material was prepared. This is followed by a detailed description of the excimer laser setup. The last two sections of this chapter briefly describe all the characterization methods used in this work. These sections focus on the experimental details rather than on the actual physical principals of these characterization methods, which can be found in the literature. Raman backscattering measurements are described in a separate section as this is a method which was extensively used in the course of this work.

3.1 Starting material

In most cases the starting material for the crystallization experiments was hydrogenated amorphous silicon (a -Si:H) prepared by the decomposition of pure silane (SiH_4) with plasma enhanced chemical vapor deposition (PECVD). Almost all samples used in this work were deposited on quartz substrates. The substrates were cleaned employing a standard RCA-process [45] before loading them into the deposition chamber. The films were deposited under standard conditions which are known to produce device grade amorphous silicon. These standard conditions are summarized in Table 3.1. A brief review of the deposition of a -Si:H by PECVD can be found elsewhere [5]. Doping was achieved by mixing SiH_4 with either phosphine (PH_3) or diborane (B_2H_6) for n-type or p-type doping, respectively. The nominal gas phase doping was varied from 100 ppm up to 10.000 ppm.

For some experiments hydrogenated microcrystalline silicon (μc -Si:H) samples were used. The μc -Si:H samples were also deposited by PECVD. The standard parameters for the deposition of undoped μc -Si:H films are also listed in Table 3.1. Again, doping was achieved by mixing SiH_4 with PH_3 or B_2H_6 . However, when the standard parameters were used the crystallinity of the doped samples determined by Raman backscattering measurements was rather small. To grow highly doped μc -Si:H with a

Raman crystallinity of more than 50 % the hydrogen dilution had to be increased to 99 % or higher and the rf power had to be increased to 180 mW/cm² or even 200 mW/cm².

Table 3.1: Standard conditions of *a*-Si:H and μ c-Si:H deposition

Deposition parameters	Undoped <i>a</i> -Si:H	Undoped μ c-Si:H
T _{Substrate} (°C)	230	230
p (mbar)	0.23	0.4
P (mW/cm ²)	120	160
[H ₂]/([H ₂] + [SiH ₄]) (%)	0	98
r (Å/s)	≈ 2	≈ 0.3

For some experiments *a*-Si:H and μ c-Si:H films deposited by electron cyclotron resonance chemical vapor deposition (ECR-CVD) and *a*-Si films prepared by reactive magnetron sputtering in Ar atmosphere were used. Details on the ECR-CVD method can be found in Ref. [46], while magnetron sputtern of *a*-Si is reviewed in Ref. [47].

3.2 Laser crystallization

Excimer laser crystallization setup. The principal setup of the laser crystallization apparatus is shown in Fig. 3.1. The heart of the experiment is the XeCl excimer laser (Lambda Physik, Compex 205i), operating at a wavelength of 308 nm. The laser can achieve a maximum fluence of $\approx 900 \text{ mJ/cm}^2$. In the experiments of this work, the laser was operated with frequencies in the range of 1 - 20 Hz.

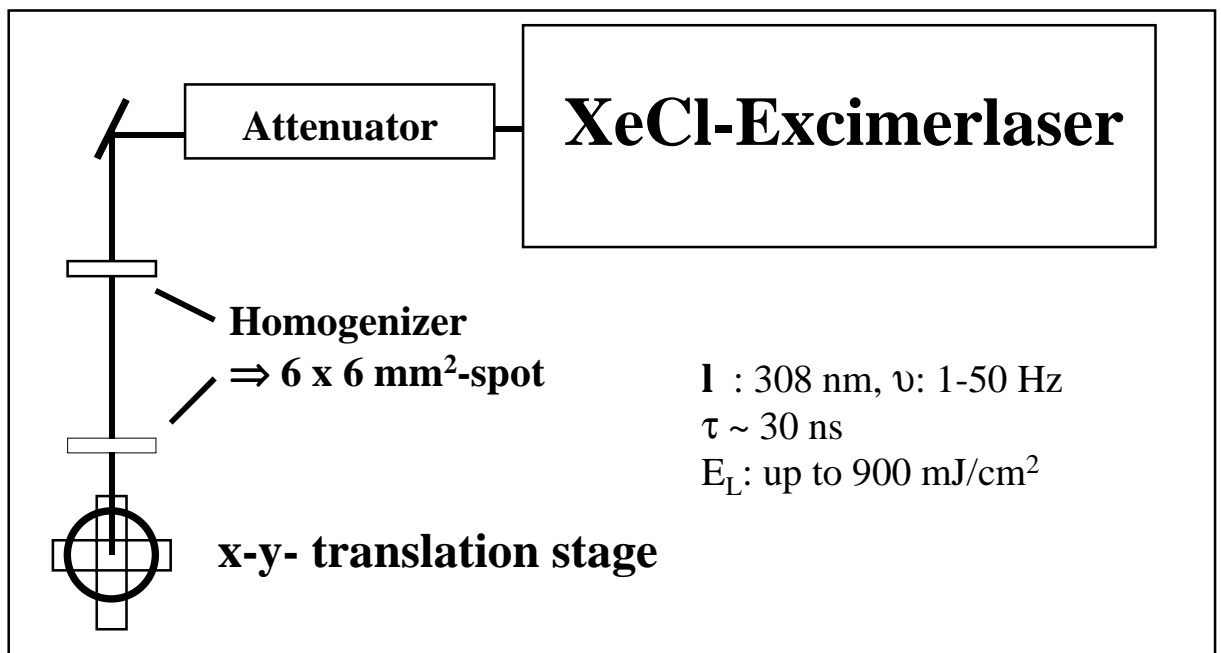


Fig. 3.1: The excimer laser crystallization setup.

The pulse width τ of the laser pulse is approximately 30 ns. However, the actual pulse profile shown in Fig. 3.2 consists of two intensity peaks. Since the $6 \text{ mm} \times 23 \text{ mm}$ spot emitted by the laser is inhomogeneous an optical homogenizer is used to create an uniform $6 \text{ mm} \times 6 \text{ mm}$ laser spot. The laser fluence E_L is tuned with an optical attenuator. To ensure an accurate measurement of E_L two things have to be remembered. Firstly, E_L is not constant over longer periods of time since the laser fluence critically depends on the condition of the laser gas, which changes in the course of time and operation. Secondly, the area of the laser spot enters into the value of E_L . Hence, it is important to measure the area of the laser spot accurately. The sides of the laser spot can be meas-

ured with an accuracy of ± 0.1 mm, which in consequence leads to an uncertainty for the measurement of the area of the laser spot of about ± 1.2 mm². Thus, the absolute values of E_L have an uncertainty of about ± 5 mJ/cm² for moderate fluences (100 - 200 mJ/cm²) and ± 12 mJ/cm² for higher laser fluences (400 - 600 mJ/cm²). The relative values of E_L are not affected as long as the optical setup is not modified or readjusted.

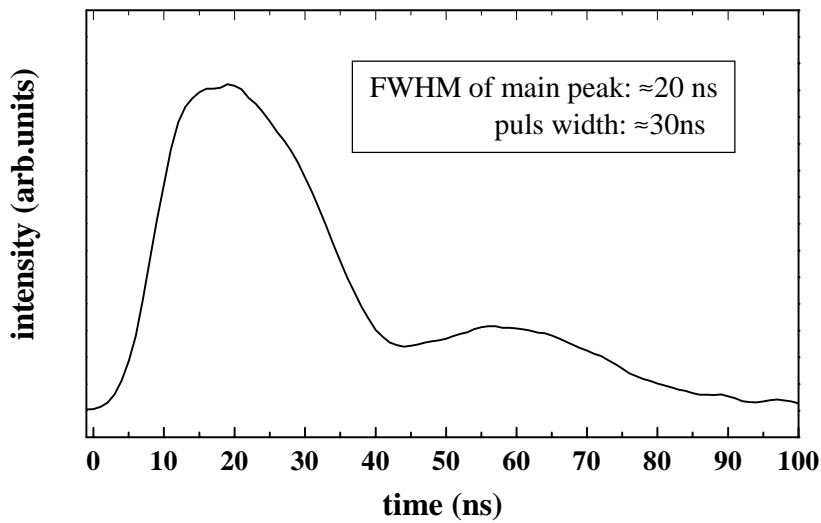


Fig. 3.2: Pulse profile of the excimer laser pulse.

The samples are crystallized in a vacuum chamber, which is mounted on a x-y translation stage. Crystallization of large areas is achieved by moving the sample beneath the beam. However, due to the rather large laser spot size, some experiments were performed only by crystallizing spots. All crystallization experiments were performed at room temperature in vacuum with a pressure of $< 9 \times 10^{-5}$ mbar. Most crystallization experiments were performed using multiple shot crystallization with a shot density of 100 shots per area. In the case of crystallization of large areas the velocity of the x-y translation stage was adjusted depending on the frequency of the laser used in order to ensure an overlap between subsequent laser pulses which results in a shot density of 100 shots per area.

***In situ* time resolved reflectivity (TRR).** TRR measurements give information on the details of the actual crystallization process. Since metallic liquid silicon has a much higher reflectivity than amorphous and crystalline silicon the change in reflectivity can be used to determine parameters like the threshold energy of melting E_T and the melt duration during the process. In order to measure the TRR a HeNe laser with a wavelength of 632.8 nm and output power of 2 mW was focused on the sample, where the excimer laser spot hits the surface. The reflected beam of the HeNe laser is focused on a fast Si photo diode. For data acquisition a digital oscilloscope with a sampling rate of 1 GHz is used. The trigger is supplied by a second photo diode which picks up stray light from the optical path.

3.3 Characterization methods

Structural characterization

SEM. Information on the grain size of laser crystallized poly-Si was obtained from plain view scanning electron microscopy (SEM) micrographs, using a REM S-4100 (Hitachi) with a cold field emission cathode. To obtain a good contrast between grains and grain boundaries it is necessary to perform Secco etching [48] of the crystallized films. The Secco etch solution consists of one volume part $K_2Cr_2O_7$ in H_2O (44.133 g/l) and two volume parts of 49 % HF. Secco etch preferably etches the grain boundaries in polycrystalline silicon. Additionally, the SEM is equipped with a Si(Li)-Q detector (Noran) which can be used for X-ray microanalysis energy-dispersive spectrometry (EDS).

AFM. In order to gain information on the roughness atomic force microscopy (AFM) measurements were performed on some laser crystallized poly-Si samples. The AFM measurements were performed with a Topometrix Explorer 2000 in the non-contact mode using silicon tips with a tip radius smaller than 10 nm. For detailed descriptions of the physical principals and the experimental details of AFM measurements see Ref. [49].

XRD. To determine the orientations of the grains X-ray diffraction (XRD) measurements were performed in symmetric θ - 2θ geometry with a Bruker D8 Advance

diffractometer operating with $\text{CuK}\alpha$ radiation ($\lambda = 1.5418 \text{ \AA}$). The diffractograms were recorded while the samples were rotated around the substrate normal. The sample size for the XRD measurements was about $20 \text{ mm} \times 20 \text{ mm}$. Due to the small thickness of the investigated samples long accumulation times of up to 15 h were necessary to achieve a good signal to noise ratio. A detailed description of the principles and the experimental details of XRD can be found in Ref. [50].

EBSP. Electron backscattered diffraction patterns (EBSP) analysis is another method which provides information on the orientation of grains by obtaining and analyzing pseudo-Kikuchi patterns in a conventional SEM. A review of this microscopy is given in Ref. [51].¹ The measurements were performed at the University of Erlangen, Germany. The pseudo-Kikuchi patterns were taken in steps of $0.5 \text{ }\mu\text{m}$, which yields for each sample a matrix of several hundred measurements of grain orientations. The EBSP analysis is limited to grains larger than 500 nm . The obtained data on the grain orientations can conveniently be summarized by plotting them in a stereographic triangle. This provides immediate information on whether the grains show a preferential orientation (texture). EBSP analysis can also provide information on the types of grain boundaries present in the samples.

SIMS. Secondary-ion mass spectrometry (SIMS) was used to measure the hydrogen (H) concentration depth profiles in some samples. SIMS measurements were performed using a Cs^+ ion beam. A standard c-Si sample with a H concentration of $1 \times 10^{14} \text{ cm}^{-3}$ was used to calibrate the H concentration. The absolute concentration values are accurate to within a factor of 2, but the relative precision when comparing two profiles is much better. The depth scales were obtained by measuring the depth of the sputtered craters with a mechanical stylus. More information on SIMS measurements can be found elsewhere [52].

TEM. Detailed investigations of the structure of the laser crystallized films were performed on some samples at the University of Erlangen. Transmission electron microscopy (TEM) measurements were carried out using a high resolution microscope operated at 300 kV and a conventional microscope operated at 200 kV . To preserve the

¹ This microscopy is also called Orientation Imaging Mapping (OIM) or Backscattered Kikuchi Diffraction patterns (BKD) analysis.

as-crystallized surfaces the samples were thinned from the back side. Plain view TEM micrographs were used to evaluate grain sizes and intragrain dislocation densities of poly-Si samples. The dislocation density was obtained by analyzing several bright field micrographs taken from an area of $100\ \mu\text{m} \times 100\ \mu\text{m}$. On each spot at least three micrographs were taken to ensure that no dislocation is missed. Again, for a full description of all the relevant physical and technical details see Ref. [53].

Optical and electrical characterization

Reflection and absorption. Reflection spectra were measured with a Perkin-Elmer Lambda 19 UV-VIS-NIR spectrophotometer in the energy range from 0.7 eV to 4.5 eV. The spectrally and diffusely reflected light was recorded by an integrating sphere. To obtain the absorption of the samples spectroscopic ellipsometry measurements were carried out on a Woollam VASE rotating analyzer ellipsometer at an angle of incidence of $77.00^\circ \pm 0.02^\circ$ in the energy range from 0.7 eV to 4.5 eV.

Hall effect measurements. Resistivity ρ , free carrier concentration n or p , and Hall mobility μ_H of the free carriers were measured by standard resistivity and Hall effect measurements in vacuum using the Van der Pauw configuration. The measurements were performed on square $5\ \text{mm} \times 5\ \text{mm}$ samples. Evaporated or sputtered Al and Mg contacts were used as contacts for p- and n-type samples, respectively. All contacts showed ohmic characteristics, which was checked prior to each measurement. Typically, a magnetic field of 0.7 T was applied for the Hall effect measurements. Temperature dependent measurements of ρ , n , and μ_H were performed with a close-cycle Helium cryostat in the temperature range of 20 - 300 K. An excellent review of the principals and experimental details of resistivity and Hall effect measurements, as well as detailed discussions of a variety of measurements and their analysis can be found in Ref. [54].

3.4 Raman spectroscopy

Raman spectroscopy was performed with two goals. Firstly, by measuring the Raman spectra in the range of 100 - 700 cm^{-1} information on the crystallinity was obtained. Secondly, the hydrogen local vibrational modes were measured in the range of 1900 - 2200 cm^{-1} to gain information on the hydrogen bonding configurations in the samples. The physical principles of Raman scattering in solids are described in detail in Ref. [55].

Raman measurements were performed in the back-scattering configuration using a DILOR/ISA LabRAM 010 equipped with an unpolarized HeNe laser for excitation ($\lambda = 632.8 \text{ nm}$). The intensity of the 7 mW HeNe laser was reduced by a factor of 10 using a gray filter. Spectra were usually taken with an objective of magnification 100 which results in a laser spot with a diameter of $\approx 1 \mu\text{m}$. For this reason this setup is usually called micro-Raman spectroscopy. The Raman setup is equipped with a 1800 grooves/mm and a 600 grooves/mm grating which result in a spectral resolution of $\approx 1 \text{ cm}^{-1}$ and $\approx 3 \text{ cm}^{-1}$, respectively. In the range of 100 - 700 cm^{-1} the spectra were recorded using the 1800 grooves/mm grating. The hydrogen modes were measured mostly with the 600 grooves/mm grating because the signal to noise ratio is better. The reduced spectral resolution in this case is tolerable because the hydrogen modes are broad features (FWHM $\approx 60 - 80 \text{ cm}^{-1}$).

As an alternative to the HeNe excitation the 457.9 nm line of an Ar ion laser was used in some cases. However, the spectral resolution is rather poor, being 3 cm^{-1} and 10 cm^{-1} for the 1800 grooves/mm and 600 grooves/mm grating, respectively. Usually different Raman excitation wavelengths are used to probe different volumes of a sample. A measurement with a shorter wavelength gives information from regions closer to the surface, due to the smaller penetration depth of the light. The penetration depth d_p in case of Raman measurements amounts to [56]

$$d_p = \frac{-\ln 0.1}{2\alpha} = \frac{2.3}{2\alpha}. \quad (3.1)$$

In this equation α denotes the absorption coefficient of the laser light in the material. Using equation (3.1) d_p of the two laser wavelengths can be estimated for *a*-Si:H and poly-Si. The values are summarized in Table 3.2. The absorption coefficients were determined by spectroscopic ellipsometry on samples prepared in the course of this work. As can be seen from Table 3.2 it is not possible to probe different regions of a typical 100 nm laser crystallized poly-Si thin film with the two laser wavelengths.

Table 3.2: Penetration depths of the two Raman excitation lasers

	α (633 nm) (cm^{-1})	d_p (633 nm) (nm)	α (458 nm) (cm^{-1})	d_p (458 nm) (nm)
<i>a</i> -Si:H	1.8×10^4	≈ 640	2.7×10^5	≈ 40
poly-Si	3.4×10^3	≈ 3400	4×10^4	≈ 290

4 Terminology of thin film silicon modifications

This work is in some sections concerned with the comparison of different thin film silicon modifications. Therefore, this chapter attempts to give a reference for the way in which the terms for the different thin film modifications will be used. This is necessary, since in the literature the terms nano-, micro- and polycrystalline silicon are not consistently used to describe the investigated material.

The names amorphous silicon (*a*-Si) and crystalline silicon (*c*-Si) are not disputed, the later meaning single crystalline wafers and homoepitaxially grown silicon films, which are also called epitaxial films (*epi*-Si). Amorphous silicon is characterized by a lack of long range order.¹ The nomenclature for all forms of disordered silicon in-between those two extremes is complicated and potentially confusing. In the course of this work the term microcrystalline silicon (μc -Si) is applied for all as-deposited samples with a Raman crystallinity larger than 0 % but less than 100 %. The Raman crystallinity will be properly defined in the next section. It should be noted, that the term microcrystalline suggesting a grain size on the order of some micrometer in diameter is misleading. The actual grain size in μc -Si is typically less than 30 nm.² Depending on the deposition parameters μc -Si can contain a considerable fraction of amorphous silicon. Microcrystalline silicon with high crystallinity often has a residual amorphous layer with a typical thickness of about 10 nm at the interface to the substrate [57]. However, this residual phase can be avoided by special deposition parameters [58, 59].

In the course of this work the term polycrystalline silicon (*poly*-Si) is used exclusively for large grained material with no amorphous phase present. The lateral grain size of *poly*-Si is typically larger than 100 nm, although there are exceptions to this rule. The

¹ The reader should note the distinction between hydrogenated amorphous silicon (*a*-Si:H) and amorphous silicon which does not contain hydrogen (*a*-Si). In this work the term *a*-Si will also be used to refer to amorphous silicon in general, in cases where the hydrogen content is not significant.

² For this reason some groups have renamed this modification to nanocrystalline silicon (*nc*-Si). If one encounters *nc*-Si in the literature one has to bear in mind that usually μc -Si is meant. However, the term *nc*-Si is also used for material with small crystals embedded in an amorphous matrix.

distinction between poly-Si and $\mu\text{-Si}$ with a high Raman crystallinity is difficult but can be made by considering the preparation methods. Microcrystalline silicon is prepared from the gas phase at low temperatures (typically below 500 °C) under strong dilution, in most cases with hydrogen. On the other hand, poly-Si samples are mainly prepared by some kind of crystallization method, usually with *a*-Si as starting material (e.g. laser crystallization, solid phase crystallization, and metal induced crystallization). Poly-Si deposited directly from the gas phase is grown at high temperatures (typically > 600 °C) by employing e.g. low-pressure chemical vapor deposition (LPCVD).

Raman spectroscopy is a standard characterization method in field of thin film silicon [5]. Therefore, this method will also be extensively used in this work. To summarize this section the Raman spectra of the different silicon modifications will now be given as a reference. Fig. 4.1 (d) shows the Raman spectrum of a crystalline Si wafer. The spectrum consists of the one-phonon peak at 521 cm^{-1} of the zone-center transverse optical (TO) phonon in silicon. The line shape is Lorentzian. In silicon the transverse optical (TO) and the longitudinal optical (LO) phonon are degenerate at the zone-center (see e.g. [60]). Therefore, this phonon line will be called LO-TO phonon in this work. Fig. 4.1 (b) shows a spectrum of laser crystallized poly-Si on quartz substrate. In general, the spectra (b) and (d) are very similar.¹ Both spectra can be fitted with a Lorentzian. Fig. 4.1 (a) shows a spectrum of hydrogenated amorphous silicon, the typical starting material of this work, The lack of long range order in *a*-Si has the consequence that the phonons are not localized, which leads to a relaxation of the \mathbf{k} selection rules. In consequence, the one-phonon Raman spectrum of amorphous silicon consists of several broad peaks, caused by the transverse acoustical (TA) phonon ($\approx 150\text{ cm}^{-1}$), the longitudinal acoustical (LA) phonon ($\approx 320\text{ cm}^{-1}$), the longitudinal optical (LO) phonon ($\approx 390\text{ cm}^{-1}$) and most importantly the transverse optical phonon (TO) at $\approx 480\text{ cm}^{-1}$. In Fig. 4.1 (a) only the TO phonon can be seen. As the phonon frequencies in disordered, amorphous silicon are governed by statistical fluctuations the Raman peaks have to be fitted with Gaussians. Fig. 4.1 (c) shows a Raman spectrum of

¹ There are differences in the signal intensity, due to the different thickness (laser crystallized film 100 nm, wafer > 100 μm), a slightly larger full width at half maximum (FWHM) of the LO-TO phonon line of the poly-Si, most certainly caused by the grain size and a frequency shift of $\approx 5\text{ cm}^{-1}$, which will be discussed in section 5.2.

hydrogenated microcrystalline silicon ($\mu\text{c-Si:H}$) deposited by PECVD. This spectrum clearly consists of amorphous and crystalline contributions. The so-called Raman crystallinity is less than 100 %. On the other hand, the Raman crystallinity of the poly-Si shown in Fig. 4.1 (b) is 100 %. However, it is possible to deposit $\mu\text{c-Si:H}$ with higher crystallinity, i.e. with a Raman spectrum more similar to the spectrum of c-Si and poly-Si. In the course of this work undoped silicon, which shows an asymmetrically broadened LO-TO phonon line, i. e. with a Raman crystallinity less than 100 % is called $\mu\text{c-Si}$.

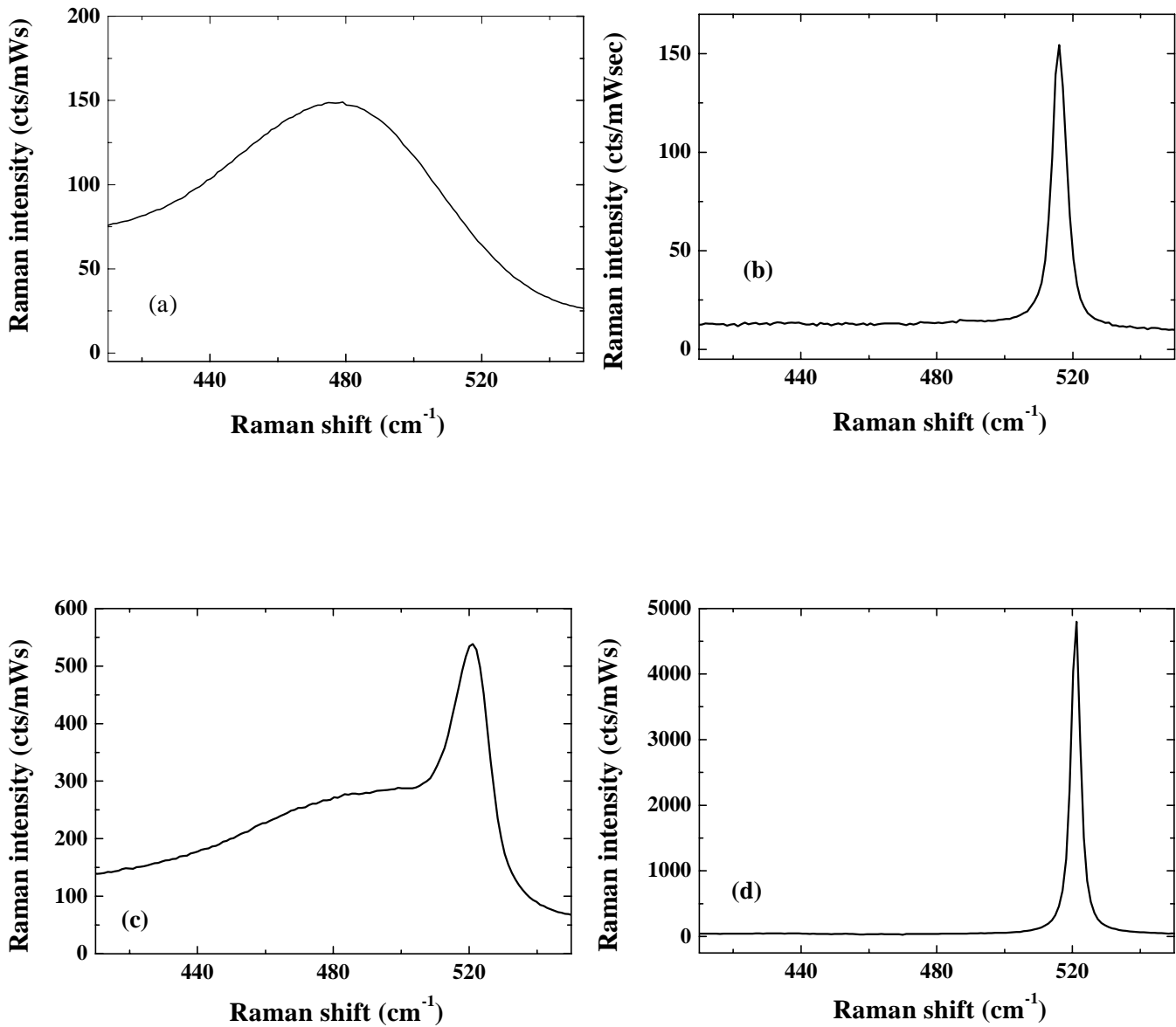


Fig. 4.1: Raman spectra of different silicon modifications: (a) a-Si:H, (b) poly-Si, (c) μ c-Si:H, and (d) c-Si in the vicinity of the LO-TO phonon line of c-Si. All samples are nominally undoped.¹

¹ The units in the figures are counts per mWs. They are given as a reference. These units were determined by measuring the intensity of the Raman laser. They are not provided by the micro-Raman setup and will not be given on the Raman spectra of the following sections.

5 Results

This chapter is divided into three parts. In the first section the results of a detailed investigation of the successive crystallization/dehydrogenation procedure are presented. It will be shown that in the course of the successive crystallization a two-layer system is created with a crystallized layer extending from the surface into the film and a residual amorphous layer at the interface to the substrate. According to SIMS measurements high amounts of hydrogen are still present in the films in the course of successive crystallization. The hydrogen bonding configurations are investigated by Raman spectroscopy and it will be shown that the dissociation of the hydrogen mode at 2000 cm^{-1} is larger than the dissociation of the mode at 2100 cm^{-1} . In the following section the results of the investigations of the structural properties of the resulting poly-Si films are presented. It will be shown that the grain boundaries of the laser crystallized poly-Si are dominated by first and second order twin boundaries. Samples crystallized in the super lateral growth regime exhibit a strong $\{111\}$ -preferential orientation of the grains. In the third section the results on the investigation of the influence of heavy doping on the crystallization process are presented. The structural and electrical properties of the doped samples are investigated. Finally, it will be shown that the heavy doping has a strong influence on the Raman spectra of the laser crystallized poly-Si.

5.1 Successive crystallization

Device grade *a*-Si:H deposited by PECVD usually contains up to 10 at. % hydrogen (H). During laser crystallization hydrogen can cause ablation of the film if the laser energy is too high due to explosive outdiffusion. To prevent ablation a conventional furnace anneal is normally performed prior to the laser crystallization. To remove the hydrogen from the starting material the temperature during the anneal has to be 400 - 500 °C. About four hours are needed to remove the hydrogen from *a*-Si:H with a film thickness of 100 nm. However, electrical and optical properties of poly-Si are dominated by grain boundary defects that have been identified as silicon dangling-

bonds using electron spin resonance (ESR) [61]. To achieve device-grade material it is essential to minimize the dangling-bond density. Commonly, this is achieved by the incorporation of hydrogen which effectively passivates Si dangling bonds and thus improves the electrical properties of the material [62]. Instead of removing H before crystallization and reintroducing it into the poly-Si after the laser crystallization it would be desirable if the crystallization process could be performed with enough hydrogen left in the sample to minimize the defect concentration. A method to perform laser crystallization of *a*-Si:H containing large amounts of H without preannealing the samples was reported by Mei *et al.* [26, 32]. They applied a laser dehydrogenation/crystallization process where the laser treatment is performed in successive runs with an increased laser fluence in each run. This step-by-step crystallization has the additional advantage that the process temperature is kept at room temperature. For this reason this technique was employed for laser crystallization experiments using plastic substrates [63]. In the following section the same technique of a combined crystallization and dehydrogenation process is applied. The resulting specimens are characterized using Raman spectroscopy and SIMS measurements to gain more insight into the mechanism of this process. By closely examining the behavior of hydrogen during the process relevant information concerning the hydrogen bonding in disordered silicon will be generated.

All the samples presented in this section are crystallized in a step-by-step process starting at low laser fluences and using an increased laser fluence in each run. The steps are typically on the order of 30 mJ/cm². All quoted values of the laser fluence E_L are the values of the last step of the respective successive crystallization sequence.

Fig. 5.1 shows Raman backscattering measurements for different steps of a crystallization sequence. The sample thickness is 100 nm. The background signal was subtracted from the data and the spectra are normalized. The crystallinity X_C was determined by the following equation [5]

$$X_C = \frac{I_C}{I_C + \gamma \cdot I_A}, \quad (5.1)$$

where I_C and I_A represent the integrated intensities of the crystalline and amorphous contributions to the spectra, respectively. To take into account the different Raman

scattering cross sections of the amorphous and crystalline phases I_A is multiplied by a correction factor γ . In this work the value 0.8 is taken for γ [64]. The background corrected Raman data were fitted with three Gaussian curves, centered around 480 cm^{-1} , 510 cm^{-1} , and 521 cm^{-1} . This method is described and discussed in detail in Ref. [65]. The amorphous and crystalline contributions are then determined from the integral intensities of the three Gaussian curves

$$\begin{aligned} I_a &= I_{480}, \\ I_c &= I_{510} + I_{521}. \end{aligned} \quad (5.2)$$

The spectrum of the as-deposited film in Fig. 5.1 shows a broad peak at 480 cm^{-1} characteristic for a -Si. After the first step of the crystallization sequence a second peak emerges at 517 cm^{-1} . The Raman spectra show that the sample is partially crystallized.

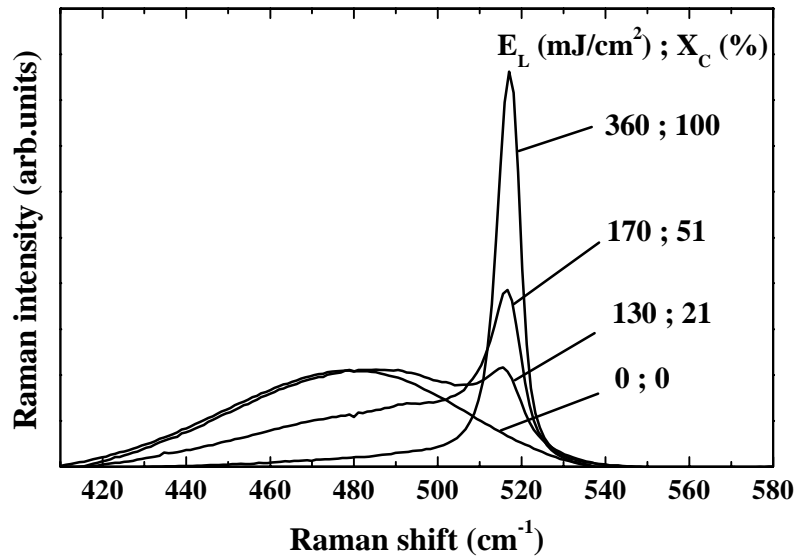


Fig. 5.1: Raman spectra of a sequence of successive crystallization. The final laser fluence and the resulting crystallinity of the sample are given in the figure.

Even at relatively low laser fluences X_C amounts to 21 %. In the following steps of the crystallization sequence the peak at 517 cm^{-1} increases at the expense of the amorphous peak at 480 cm^{-1} and thus X_C increases. The crystallization sequence was ended when the samples were completely crystallized. In that case the Raman spectra consisted of a single peak at 517 cm^{-1} which could be fitted with a Lorentzian. An example of the Ra-

man spectrum of a fully crystallized film is show in Fig. 5.2. It should be noted that for all the samples deposited on quartz substrate the peak position of the LO-TO phonon line deviates from 521 cm^{-1} for single crystalline silicon indicating the presence of stress in the poly-Si. The origin of this shift will be discussed in section 5.2.

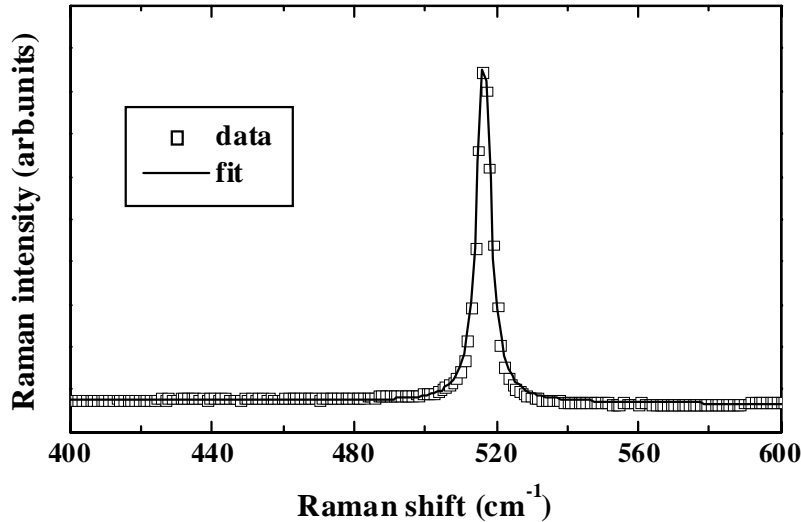


Fig. 5.2: Raman spectrum of a fully crystallized sample. The data can be fitted with a Lorentzian.

According to the Raman spectra the first steps of the crystallization cycle lead to a partial crystallization of the films. The 308 nm laser light of the XeCl excimer laser is completely absorbed in the first few nanometers of the sample. Therefore, it is reasonable to assume that this results in a depth distribution of the crystallinity. In order to test this assumption, partially crystallized films were etched with a wet-chemical etch. Raman measurements were performed before and after the etching.¹ The results of these etching experiments are presented in Fig. 5.3 (a) and (b). The Raman spectra show, that the crystalline LO-TO mode vanishes completely after a certain amount of etching. In both figures the spectra of the etched samples consist only of the broad amorphous peak centered at 480 cm^{-1} . This is observed for samples where the crystallization sequence was terminated early, and at a later stage with the X_C of the sample being low (Fig. 5.3

¹ The wet-chemical etch consisted of a mixture of HNO_3 , H_3PO_4 , HF and H_2O (9:3:0.3:4,5), which etches polycrystalline silicon isotropically.

(a) and high (Fig. 5.3 (b)), respectively. In both cases an amorphous layer can be found at the film-substrate interface after a certain amount of etching.

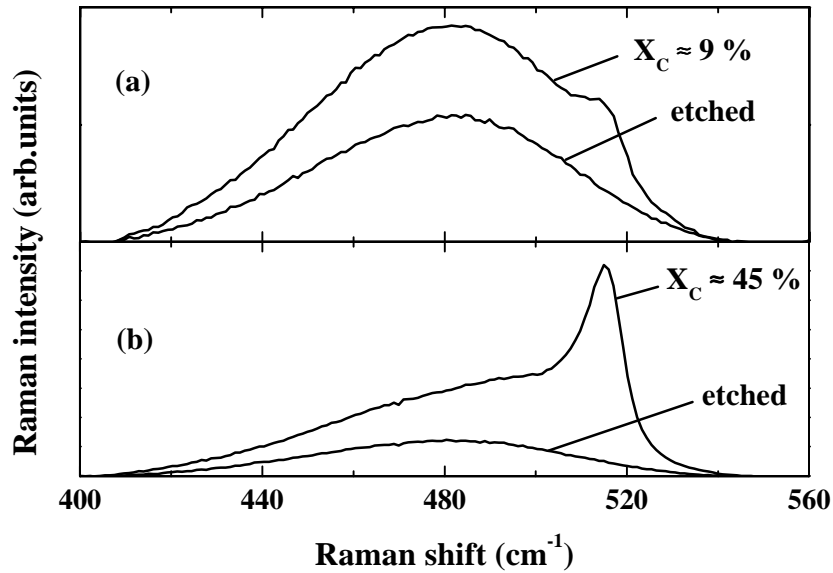


Fig. 5.3: Partially crystallized samples with low (a) and high (b) crystallinity. Raman spectra before and after etching are shown. In both cases a residual amorphous layer exists at the interface to the glass substrate which is revealed after a certain amount of etching.

The Raman data show that in partially crystallized films a two layer system is created. The crystallization starts from the surface and as a result a crystallized layer with $X_C > 0$ extends from the surface into the film. However, near the film-substrate interface an amorphous silicon layer remains. A similar observation was reported by Mei *et al.* who analyzed cross-sectional TEM micrographs of partially crystallized silicon films [26]. Fig. 5.4 shows the deconvoluted crystallinity of a partially crystallized sample as a function of the sample depth. The results shown in Fig. 5.4 were obtained through a step-by-step etching experiment, where Raman measurements were performed after each etching step. The etching depth x was measured with a mechanical stylus. As mentioned in section 3.3 (Table 3.2), the optical penetration depths of the HeNe laser light used for excitation in these Raman experiments exceeds $3\ \mu\text{m}$ and $500\ \text{nm}$ in case of poly-Si and $a\text{-Si:H}$, respectively. Thus, the Raman spectra of the partially crystallized sample always contain the information of the entire two-layer system. The inset of Fig.

5.4 shows the principle of the experiment. The analysis of this structure leads to the following relation for the crystallinity X_C at a position x in the sample

$$X_C(x) = \bar{X}_C (d - x) \cdot \frac{d' - x}{d - x}. \quad (5.3)$$

Here \bar{X}_C is the crystallinity as measured for the two layer system, d' is the thickness of crystallized layer, x is the etching depth, and d the initial thickness of the samples.

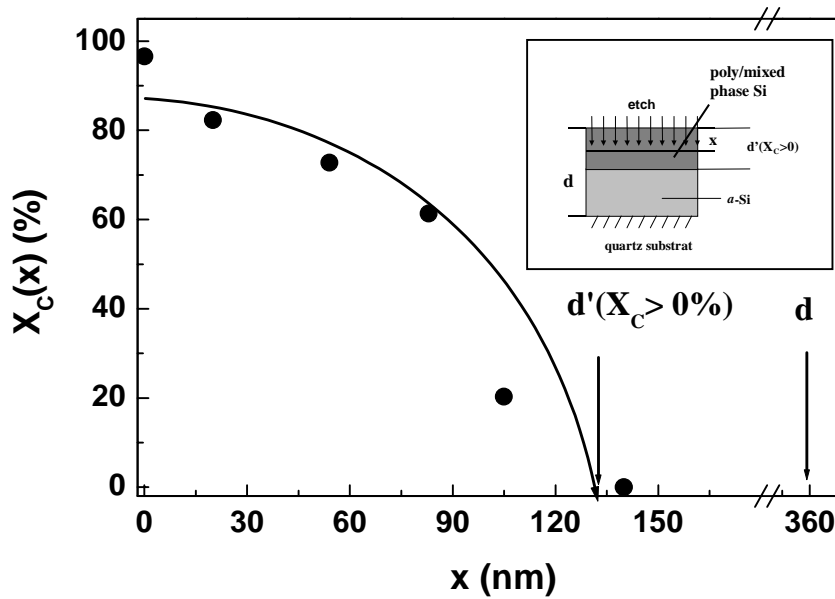


Fig. 5.4: Depth profile of crystallinity of a partially crystallized sample. The inset shows a sketch of the experiment.

The crystallinity in the crystallized layer shows an inhomogeneous depth dependence. Close to the surface the sample is polycrystalline. With increasing depth X_C decreases indicating that the film is mixed phase. Eventually X_C tends to nought when the residual amorphous layer at the film-substrate interface is reached. An analogous observation was made by Brotherton *et al.*, who reported that excimer laser crystallization with moderate laser fluences leads to poly-Si with a stratified microstructure consisting of a large grain layer at the surface and a underlying layer with finer grain material [66].

In order to investigate the differences between the step-by-step crystallization and conventional single step crystallization both crystallization procedures were performed on one and the same sample. The specimen was cut in two pieces. Then, one piece was

subjected to a vacuum anneal at 500 °C for 3 h to remove the hydrogen. Single step crystallization was performed on the dehydrogenated sample and successive crystallization was performed on the as-deposited sample. Special care was taken to ensure that the final laser energy of the successive crystallization and the single step crystallization were identical.

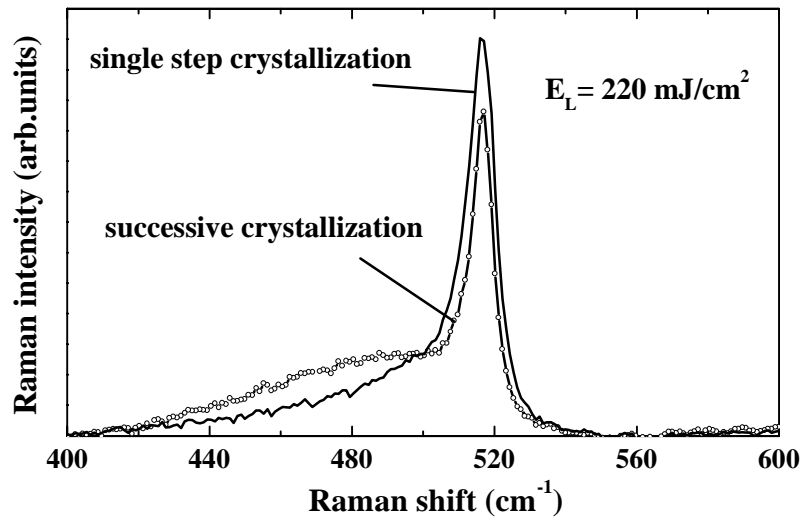


Fig. 5.5: Comparison between single step crystallization and successive crystallization.

The Raman spectra of the resulting films show significant differences for laser fluences in the range of 150 - 260 mJ/cm². One example is shown in Fig. 5.5. The crystallinity of the sample crystallized with the single laser energy is significantly higher than X_C of the sample crystallized with the step-by-step crystallization. This result can be understood if one considers the main feature of the successive crystallization. As demonstrated above the samples are partially crystallized in the course of the successive crystallization procedure. In consequence, the last crystallization step of each successive crystallization procedure is performed on a partially or even fully crystallized film depending on the laser fluence. The different optical and thermal properties of the crystallized top layer which develops in the course of the successive crystallization are the cause for the result shown in Fig. 5.5.

To illustrate the effect of the step-by-step crystallization on hydrogen (H) bonding and concentration Fig. 5.6 shows the Raman spectra of a successive crystallization sequence in the range of 1800 - 2400 cm^{-1} . The evolution of the $(\text{Si-H})_X$ stretching local vibrational modes are shown for the same sample for which the evolution of X_C was measured (see Fig. 5.1). In as-deposited $a\text{-Si:H}$ ($E_L = 0$) the mode of Si-H at approximately 2000 cm^{-1} and the mode of $(\text{Si-H})_X$ at approximately 2100 cm^{-1} can be resolved.

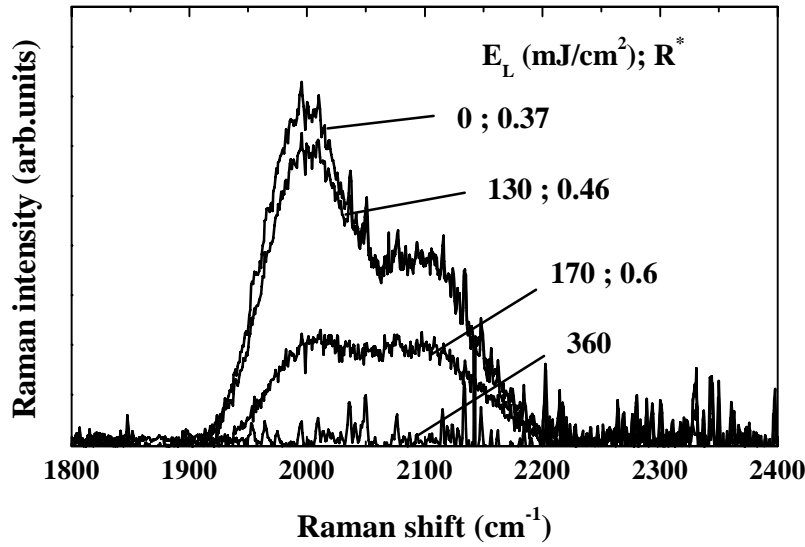


Fig. 5.6: Raman spectra of H modes in the course of successive crystallization. The background signal was subtracted from the original data and the curves are normalized. The final laser fluence and the microstructure parameter R^* are given in the figure.

For hydrogenated amorphous silicon the so-called microstructure parameter R^* is often defined indicating the fraction of H atoms that are not in isolated Si-H bonds [5]

$$R^* = I_{2100} / (I_{2000} + I_{2100}). \quad (5.4)$$

Here I_{2000} and I_{2100} are the integrated intensities of the Raman modes at 2000 cm^{-1} and 2100 cm^{-1} , respectively. For amorphous silicon R^* is usually taken as a figure of merit, with $R^* = 0$ for the structurally best material [5]. In this work R^* is only quoted to give a numerical value for the ratio of the modes at 2000 cm^{-1} and 2100 cm^{-1} so that changes of this ratio can be compared more easily. The values for R^* for the various stages of the crystallization sequence are indicated in Fig. 5.6. In the first cycle of the crystalliza-

tion procedure ($E_L = 130 \text{ mJ/cm}^2$) only a decrease of the mode at 2000 cm^{-1} is observed. R^* increases from an initial value of 0.38 for the as-deposited film to a value of 0.47. In the following cycles with increasing laser fluence the intensity of the mode around 2100 cm^{-1} decreases too. However, the mode at 2000 cm^{-1} decreases faster than the mode at 2100 cm^{-1} , resulting in an even higher value of $R^* = 0.6$ [67]. Removing the crystallized layer of a partially crystallized film by wet-chemical etching does not result in a significant change of R^* . The enhanced dissociation of Si-H in the course of the successive crystallization is an important result and has not been reported so far. This result will be fully discussed in section 6.1.

Absolute H concentrations c_H of the films were obtained from SIMS measurements. Fig. 5.7 shows the c_H depth profiles for several steps of a crystallization sequence.¹ In the as-deposited sample c_H amounts to about 17 at. %. It is important to note that the partially crystallized films still contain a large amount of hydrogen (≈ 7.5 at. %). For moderate laser fluences ($E_L \leq 180 \text{ mJ/cm}^2$) the hydrogen profiles are essentially flat, although the crystallinity is approximately 50 %. A similar observation was reported by Mei *et al.* [26] for 50 nm thick films for laser energies up to 374 mJ/cm^2 . However, for the final step of the crystallization process the c_H profile of the 120 nm thick sample is flat only for the first 30 nm. At greater depth c_H increases up to $2 \times 10^{21} \text{ cm}^{-3}$. The deviation from a flat profile obtained for thinner films indicates the important role of the film thickness with respect to the laser dehydrogenation process. Close to the substrate the H concentration still amounts to $c_H \approx 4$ at. % [68]. This is a factor of 4 more than has been reported previously [26]. Again, this result can be explained by taking into account the main feature of the successive crystallization, i.e. the two-layer system which develops in the course of the successive crystallization. It is rather likely that the crystallized layer acts as a diffusion barrier for the H. There is an ongoing investigation in our group where H evolution measurements are performed on partially crystallized samples to fully resolve this problem. Preliminary results indicate the importance of the two-layer system for the laser dehydrogenation, as the most radical change in the H evolution spectra occurs between the spectrum of as-deposited *a*-Si:H and the spectrum of a partially crystallized sample after the first step of the successive crystallization [69]. The

¹ These SIMS data were not obtained on the sample of Fig. 5.1 and Fig. 5.6.

features of the H evolution spectra of all other samples successively crystallized up to higher fluences are similar to the spectrum of the sample after the first step with the exception that the signal intensity decreases due to the reduced c_H in the samples as a consequence of the laser dehydrogenation.

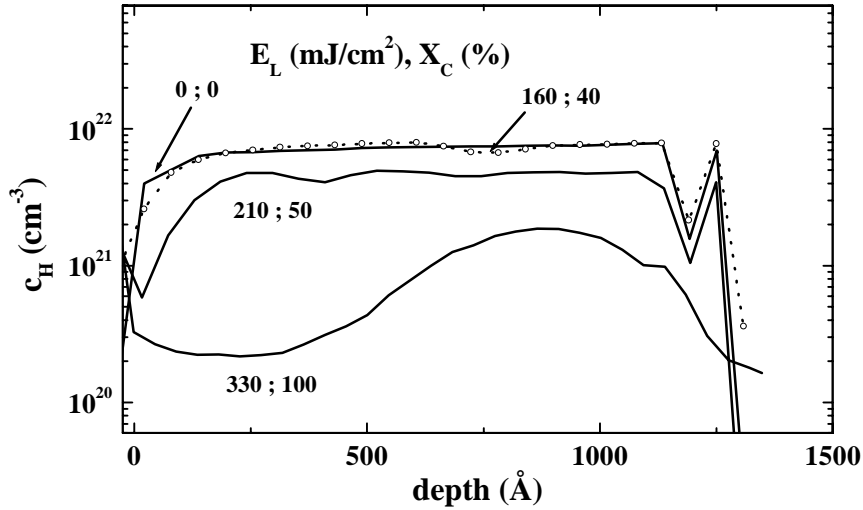


Fig. 5.7: SIMS data on 120 nm samples crystallized with successive crystallization up to the indicated laser fluence. It should be noted that the H concentrations in the course of the successive crystallization and even in the fully crystallized sample are very high.

The high amount of residual hydrogen could be technologically relevant. A fully crystallized 120 nm thick poly-Si sample still contained up to 4 at. % hydrogen. This well exceeds the typical grain boundary defect density of $6 \times 10^{18} \text{ cm}^{-3}$ of poly-Si samples crystallized in the partial melting regime as measured by electron spin resonance (ESR) [70]. This suggests that the residual H concentration could be large enough to minimize grain-boundary defect density in the fully crystallized samples [25]. This hypothesis has to be verified by ESR measurements.

Summary

In summary, successive crystallization leads to the formation of a two-layer system. The crystallinity of a partially crystallized sample exhibits a strong depth dependence. The successive crystallization is accompanied by a dehydrogenation of the samples. In the course of this dehydrogenation the dissociation of Si-H is enhanced compared to the dissociation of differently bonded hydrogen, which manifest itself in the mode at 2100 cm^{-1} . Fully crystallized samples can still contain a residual H concentration of up to 4 at. %.

5.2 Structural properties of undoped poly-Si

For device applications the question of the structural properties of the polycrystalline films is of major interest. This primarily concerns the grain size but also the quality of the grains, namely the dislocation density and the grain boundary type. These properties will strongly influence the electrical characteristics. Finally, the orientations of the grains are of fundamental importance, especially if the specimen shall be used as seed layer for a subsequent epitaxial thickening. The question of texture formation in case of laser crystallized poly-Si is also a fundamental physical problem. All these questions will be addressed in the following section, with the focus mainly on specimens with large grains crystallized in the super lateral growth (SLG) regime.

Fig. 5.8 shows the average grain size $\langle x \rangle$ of a laser crystallized poly-Si sample as a function of E_L . The grain sizes were determined by manual evaluation of SEM micrographs. The investigated areas amounted to $1.8 \mu\text{m} \times 2.4 \mu\text{m}$ in case of small grains ($\langle x \rangle < 500 \text{ nm}$) and to $18 \mu\text{m} \times 24 \mu\text{m}$ in case of larger grains sizes ($\langle x \rangle > 1 \mu\text{m}$). For each sample at least two SEM micrographs were evaluated. The vertical bars in Fig. 5.8 indicate the minimum and maximum grain size found at the specific laser fluence. The three crystallization regimes described in section 2.2 are indicated in the plot. The partial melting regime extends from 200 mJ/cm^2 to about 480 mJ/cm^2 and the full melting regime commences at about 580 mJ/cm^2 . The energy range from about 480 mJ/cm^2 to 580 mJ/cm^2 is the super lateral growth regime. The energy to achieve (maximum) super lateral growth E_{SLG} is $\approx 520 \text{ mJ/cm}^2$. Fig. 5.9 shows three micrographs of poly-Si crystallized in the different crystallization regimes. Fig. 5.9 (a) is a micrograph of a sample crystallized in the partial melting regime. Fig. 5.9 (b) and Fig. 5.9 (c) are the micrographs of a sample crystallized in the SLG regime and the full melting regime, respectively. The focus of this work is on the two regimes that avoid full melting of the specimen. In the full melting regime the thermal strain on the glass is highest, while the grain size is as small as in the partial melting regime. Moreover, the films easily ablate in the full melting regime.

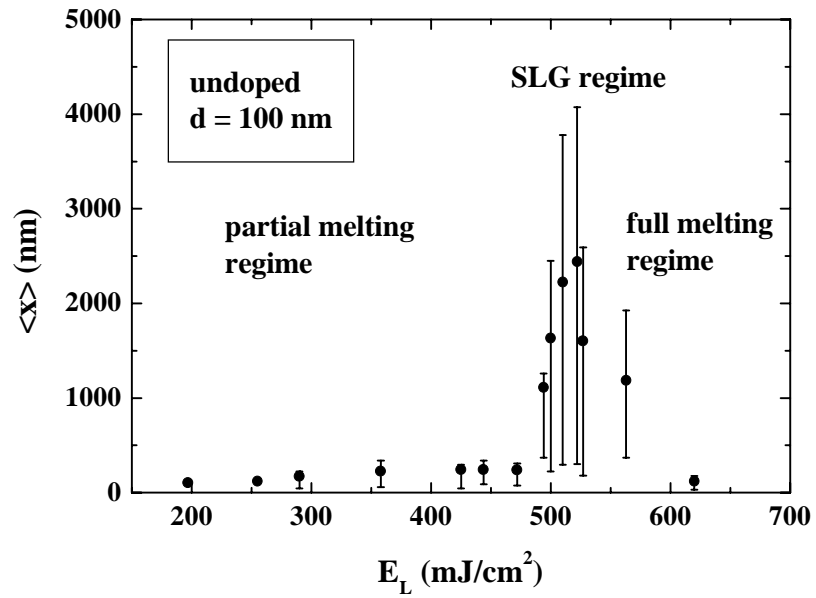


Fig. 5.8: Average grain size as a function of laser fluence. The three different crystallization regimes can be clearly distinguished. The vertical bars indicate the minimum and maximum grain size found in the samples.

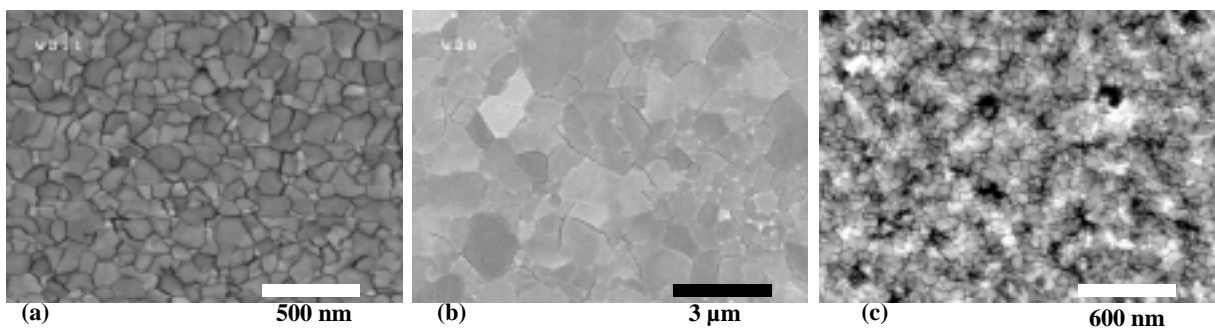


Fig. 5.9: SEM micrographs of samples crystallized in the different regimes: (a) partial melting regime, (b) SLG regime, and (c) full melting regime.

The grain size of the crystallized films has an influence on the integrated Raman intensity of the LO-TO phonon line as shown in Fig. 5.10. For $\langle x \rangle < 500$ nm the intensity of the LO-TO modes increases rapidly with increasing grain size. Once the average grain size exceeds 500 nm the increase becomes less pronounced. Eventually, when the grain size is comparable or larger than the laser spot of the Raman laser (diameter $\approx 1 \mu\text{m}$) the Raman intensity saturates. It should be noted, that the two films crystallized with $E_L > E_{SLG}$ (open symbols) show an integrated Raman intensity which does not follow the trend seen in the other samples (solid symbols). In case of the sample with $\langle x \rangle \approx 1200$ nm the reduction of the integrated Raman intensity is very likely due to a reduced sample thickness caused by ablation.

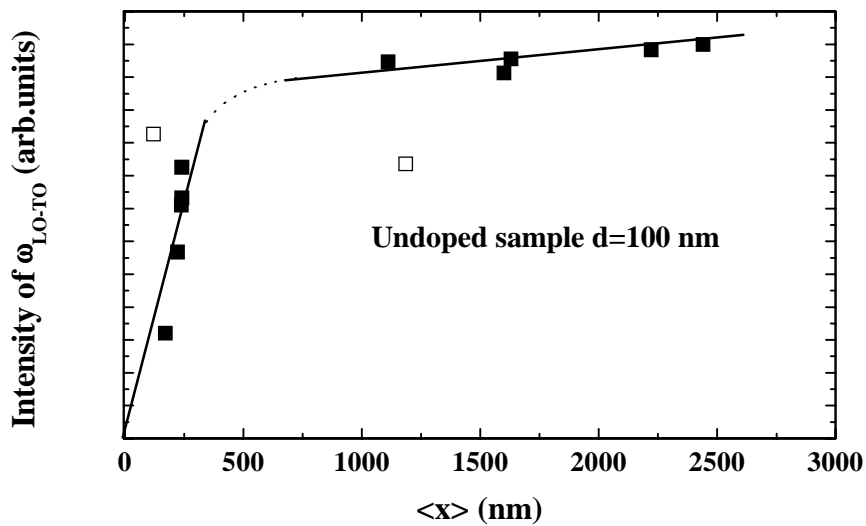


Fig. 5.10: Integrated intensity of ω_{LO-TO} Raman peak as a function of average grain size. Solid symbols are samples crystallized in the partial melting regime and the SLG regime. Open symbols are samples crystallized with $E_L > E_{SLG}$. The line is a guide to the eye.

The significantly enhanced Raman intensity in the case of the sample with the small average grain size of ≈ 120 nm, crystallized with the highest laser fluence (620 mJ/cm^2) in the full melting regime is probably caused by an increased roughness of the quartz surface. The increased roughness could modify the backreflection of the HeNe laser so that the optical path of the laser light through the sample is elongated, thus leading to stronger excitation and to an increase of the Raman signal intensity.

Raman spectra can provide information regarding the possible presence of stress in the poly-Si samples. A shift of the position of the LO-TO phonon line $\Delta\omega_{LO-TO}$ of a poly-Si sample with respect to its value for c-Si measured with the same Raman setup indicates the presence of stress in the investigated samples. A thorough review of this complex topic with the focus on experimental details and an extensive discussion of results on silicon integrated circuits can be found in Ref. [56]. A quantitative analysis of the stress depends critically on the type of stress present in the sample. An overview of the extensive theoretical work on the different types of stress and the resulting effects on the Raman spectra of poly-Si and poly-diamond is given by Anastassakis [71]. Generally, compressive uniaxial or biaxial stress results in an increase of ω_{LO-TO} while tensile stress causes a decrease. Stress can also lift the degeneracy of the LO-TO phonon in crystalline silicon [71], which is observed using polarized Raman excitation light.

As shown in Fig. 5.2 the position of the Lorentzian LO-TO phonon peak of undoped laser crystallized poly-Si is significantly shifted to lower wave numbers. For all undoped samples crystallized on quartz $\Delta\omega_{LO-TO}$ amounts to approximately -5 cm^{-1} , with respect to the position of the LO-TO phonon line in c-Si ($\omega_{LO-TO} = 521 \text{ cm}^{-1}$ in the case of the Raman setup used in this work)¹.

A significant local increase of temperature in the samples can cause a shift of the position of the phonon line. However, this is not the case for the Raman measurements of this work on undoped poly-Si. Fig. 5.11 (a) shows that the change of the intensity of the Raman excitation laser light by several orders of magnitude does not influence ω_{LO-TO} (circles in Fig. 5.11 (a)). For comparison, the results obtained for c-Si are given as well, which do not show a thermal influence either (stars in Fig. 5.11 (a)). The standard laser intensity for the Raman measurements performed in the course of this work was 0.66 mW.

¹ The exact position of the LO-TO phonon peak in silicon depends on the details of the Raman setup. Therefore, one can find values between $519\text{-}522 \text{ cm}^{-1}$ in the literature.

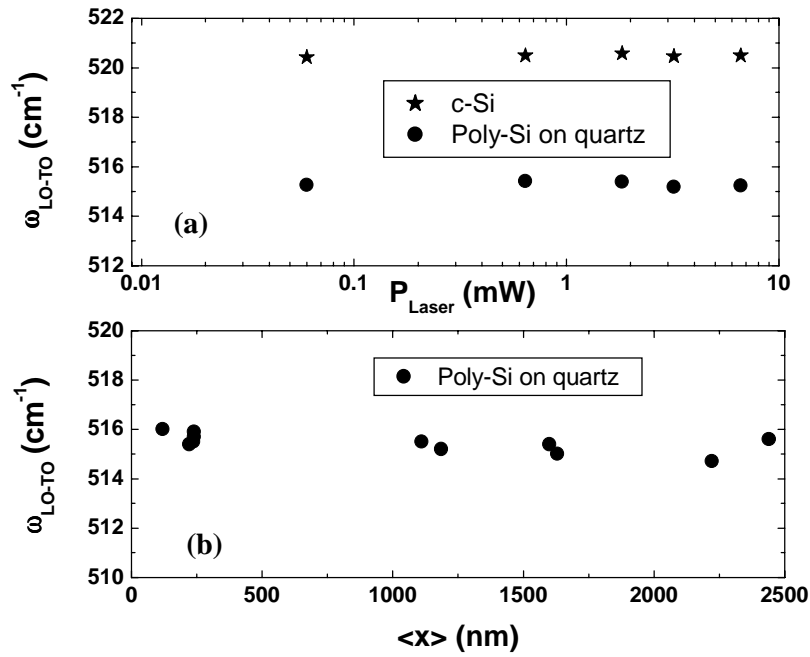


Fig. 5.11: ω_{LO-TO} as a function of the excitation laser intensity P_{Laser} (a), and ω_{LO-TO} as a function of the average grain size (b).

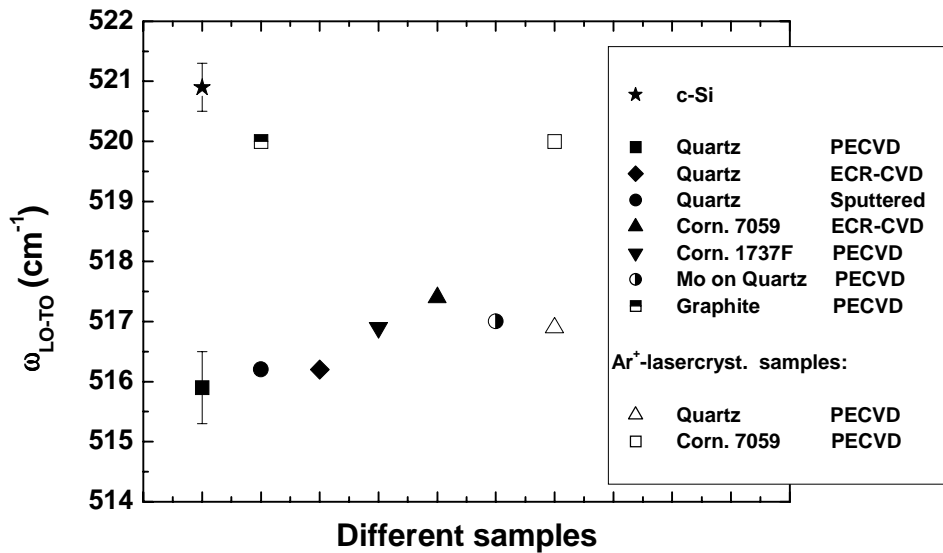


Fig. 5.12: ω_{LO-TO} for poly-Si on different substrates deposited by different deposition methods (solid symbols). Two poly-Si samples on different substrates crystallized with an Ar⁺ laser are also shown in the figure (open symbols).

In the range of $\langle x \rangle = 200 - 3000 \text{ nm}$ ω_{LO-TO} is independent of the grain size of the poly-Si as shown in Fig. 5.11 (b). All data shown in the figure are obtained by crystallizing different spots on the same α -Si:H film deposited on a $50 \text{ mm} \times 50 \text{ mm}$ quartz substrate with different final laser fluences resulting in different grain sizes. This suggests that the stress in the poly-Si originates from the sample-substrate interface.

A rough idea of the quantitative amount of tensile stress in the sample can be obtained from $\Delta\omega_{LO-TO}$ by applying the following equation, obtained theoretically by Anastassakis for pure isotropic stress in poly-Si [71]

$$\sigma_{bs} (\text{GPa}) = -0.27 \cdot \Delta\omega (\text{cm}^{-1}), \quad (5.5)$$

where σ_{bs} is the amount of isotropic stress in GPa. Taking the observed shift of $\Delta\omega_{LO-TO} \approx -5 \text{ cm}^{-1}$ ($\pm 1 \text{ cm}^{-1}$) for undoped laser crystallized poly-Si on quartz yields a stress on the order of $1.35 \text{ GPa} \pm 0.25 \text{ GPa}$.

The substrate can influence ω_{LO-TO} as shown in Fig. 5.12. The data points for poly-Si on quartz (solid square) and for c-Si (star) represent the mean values of a number of different measurements. The vertical bars are the standard deviations of these measurements. For undoped poly-Si crystallized with laser fluences below the full melting regime ω_{LO-TO} amounts to 516 cm^{-1} ($\pm 1 \text{ cm}^{-1}$) for samples on quartz. In case of poly-Si on high temperature alkaline earth aluminosilicate glass (Corning 1737F) (solid down-triangle), barium borosilicate glass (Corning 7059) (solid up-triangle), and quartz coated with molybdenum (half-solid circle) ω_{LO-TO} is only slightly different amounting to 517 cm^{-1} . It should be noted, that the use of different starting materials, such as α -Si:H deposited by ECR-CVD (diamond) and α -Si deposited by reactive magnetron sputtering in argon atmosphere (solid circle) also did not influence ω_{LO-TO} . However, in case of poly-Si on graphite ω_{LO-TO} amounts to $\approx 520 \text{ cm}^{-1}$ (half-solid square). Unfortunately, the experiment was performed using a graphite substrate, where no additional information regarding the thermal and structural properties were available. Hence, it is not possible to draw a reliable conclusion as to what actually causes the deviation of ω_{LO-TO} compared to the poly-Si samples on the other substrates. Table 5.1 summarizes the most important properties of the three different types of glasses used in the experiments. The thermal expansion coefficients α_{th} of the glasses are averages for the temperature range

of 100 - 600 °C. It has to be noted that the quoted data contain some ambiguities as it is not possible to give a reliable average temperature for the highly nonsteady-state laser crystallization process for either glass substrate or silicon.

Table 5.1: Properties of different glasses. Strain point T_{Strain} , softening point $T_{Softening}$, and thermal expansion coefficient α_{th} [72-74].

Glass	T_{Strain} (°C)	$T_{Softening}$ (°C)	α_{th} (K ⁻¹)
Quartz	787	1327	5.4×10^{-7}
Corning 7059	593	844	3.9×10^{-6}
Corning 1737F	666	975	3.1×10^{-6}
Silicon [75]	-	-	4.4×10^{-6} (0-1000 °C)

The total stress in a thin film σ_t is the sum of any external stress σ_{ext} , the intrinsic stress σ_{int} , and the thermal stress σ_{th} [76]

$$\sigma_t = \sigma_{ext} + \sigma_{int} + \sigma_{th}. \quad (5.6)$$

There is no source of external stress in the experiments described above ($\sigma_{ext} = 0$ in equation (5.6)). The experimental results strongly indicate that the tensile stress incorporated in laser crystallized poly-Si on glass substrates is mostly due to thermal stress which originates from the different α_{th} of the glasses compared to the value for c-Si. In case of thin film growth the thermal stress is given by [76]

$$\sigma_{th} = (\alpha_f - \alpha_s)(\Delta T)E_Y, \quad (5.7)$$

where α_f and α_s are the average thermal expansion coefficients of the film and the substrate, respectively. ΔT is the temperature of the film growth minus the temperature of the measurement and E_Y is the elastic (Young) modulus of the thin film. In the case $\alpha_f > \alpha_s$ the thermal stress incorporated in the films is tensile [76].¹ Thermal stress can explain the experimental findings for all the three different glass substrates (see Table

¹ This is valid for the condition $\Delta T > 0$ which is clearly met in the case of the laser crystallization experiments. E_Y is positive in the case of silicon [77].

5.1). A quantitative analysis using equation (5.7) holds some uncertainties due to the highly nonsteady-state nature of the laser crystallization. However, an order of magnitude estimation is possible. In the case of quartz taking the values from Table 5.1 for the thermal expansion coefficients, and values of $\Delta T = 1400$ K and $E_Y = 1.87 \times 10^{11}$ Pa (Young modulus of (111)-Si for a force along the [111]-direction [77]) equation (5.7) yields $\sigma_{th} \approx 1$ GPa.

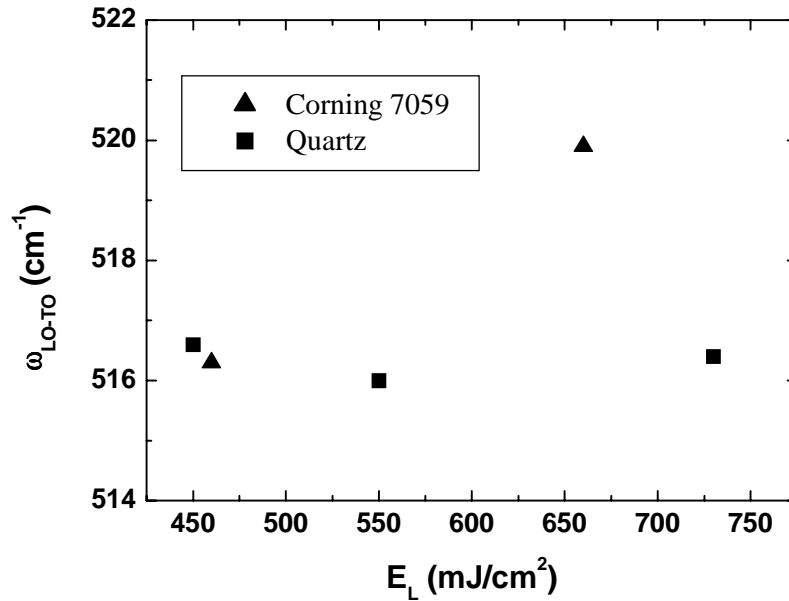


Fig. 5.13: ω_{LO-TO} for poly-Si on different glasses as a function of the laser fluence E_L .

This value is actually quite close to the value obtained from the Raman data analysis using equation (5.5) thus confirming the assumption that the stress in the poly-Si films is largely due to thermal stress. On the other hand, for the other two glasses the estimated values using equation (5.7) are considerably lower than the values obtained from the Raman data using equation (5.5) which shows the limitations of the analysis.

If the temperature of the glass during the laser crystallization approaches or exceeds the softening temperature the amount of stress incorporated in the poly-Si samples is influenced. This conclusion can be drawn from results obtained on poly-Si samples laser crystallized at the IPHT Jena, Germany, which are also shown in Fig. 5.12 (open symbols). These samples were crystallized employing an acousto-optically modulated cw

Ar⁺ laser ($\lambda = 514$ nm, pulse width > 1 ms) at a substrate temperature of 500 °C [16]. Under these conditions the thermal strain on the glass substrate is considerably higher as compared to excimer laser crystallization at room temperature. For poly-Si on quartz crystallized with the Ar⁺ laser ω_{LO-TO} amounts to 517 cm⁻¹ (open up-triangle). This value is quite similar to ω_{LO-TO} of poly-Si on quartz crystallized with excimer laser crystallization. On the other hand, for poly-Si on Corning 7059 crystallized with the Ar⁺ laser ω_{LO-TO} amounts to 520 cm⁻¹ (open square). This value is fairly close to ω_{LO-TO} of unstressed c-Si. It is likely, that the high thermal strain on the glass substrate due to the Ar⁺ laser crystallization results in a softening of Corning 7059 and thus, in a relaxation of the stress. In case of quartz no softening occurs, as the softening point of quartz is considerably higher than that of Corning 7059 (Table 5.1). In consequence, ω_{LO-TO} shifts to the value of unstressed c-Si for poly-Si on Corning 7059, while no stress relaxation occurs for the poly-Si on quartz. In case of excimer laser crystallization with laser fluences below the full melting regime a stress relaxation is not observed for poly-Si on Corning 7059. However, if E_L is much higher than E_{SLG} a reduction of the stress incorporated in poly-Si on Corning 7059 can also be observed (Fig. 5.13). Both samples shown in this figure were deposited in the same run. In case of poly-Si on Corning 7059 (up triangle) ω_{LO-TO} amounts to 516 cm⁻¹ and 520 cm⁻¹ for laser fluences of 460 mJ/cm² and 660 mJ/cm², respectively. In the case of poly-Si on quartz ω_{LO-TO} amounts to 516 cm⁻¹ for all laser fluences up to 730 mJ/cm².

The following paragraphs will focus on the structural properties of samples with maximum grain size. Fig. 5.14 shows an SEM micrograph of poly-Si ($d \approx 150$ nm) crystallized in the SLG regime. The grain size of this film is in the range of 3 - 4 μ m. Fig. 5.15 is an AFM image of a poly-Si sample crystallized in the SLG regime. The image was taken from the as-crystallized sample. The grains can be clearly distinguished. The reason for this is the ridge and hillock formation at the grain boundaries which occurs due to the freezing of capillary waves excited in the silicon melt during the crystallization [78]. At the point where two capillary waves meet silicon is accumulated due to the action of the expanding solid material on the remaining denser liquid material.

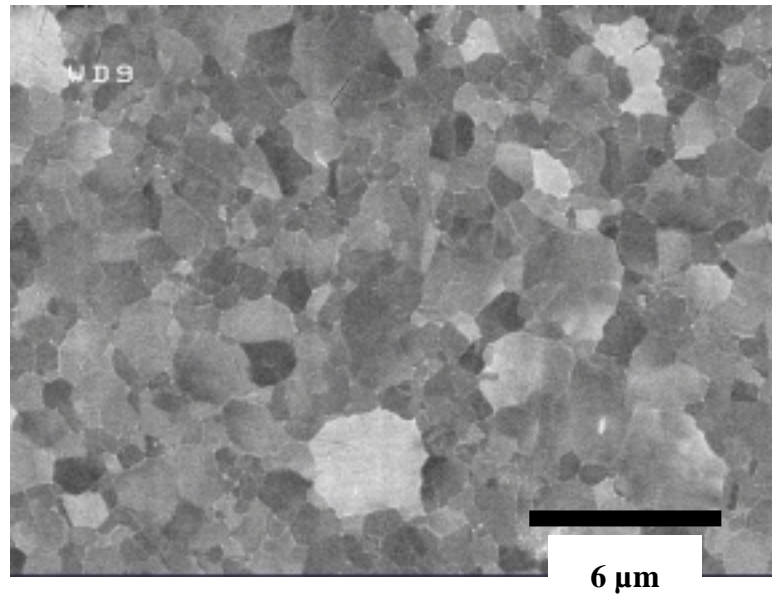


Fig. 5.14: SEM micrograph of poly-Si crystallized in the SLG regime.

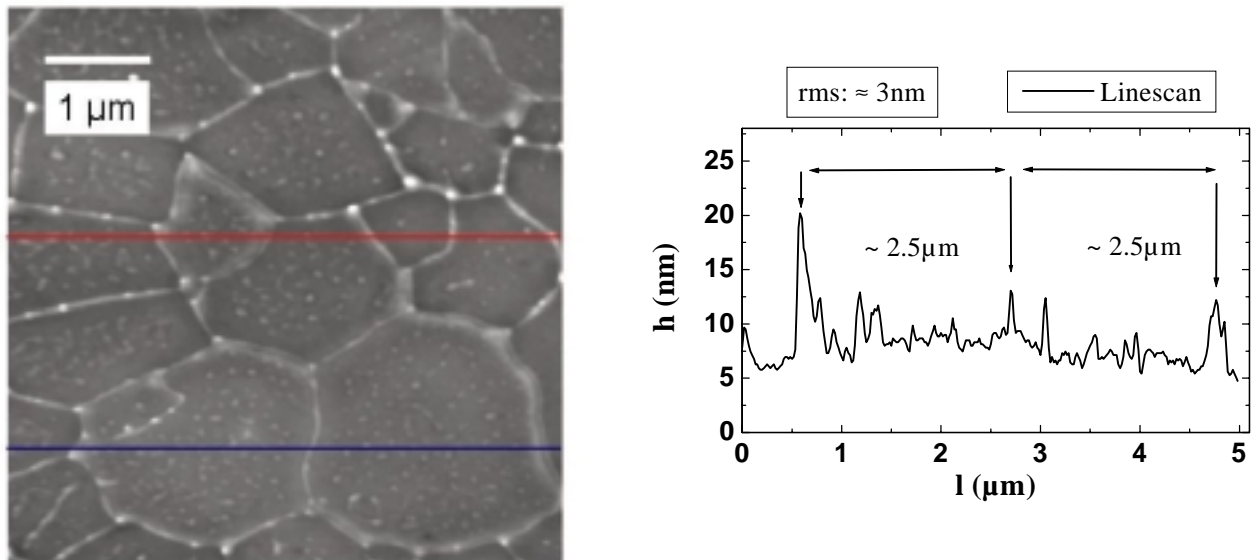


Fig. 5.15: AFM image of as-deposited poly-Si crystallized in the SLG regime (left). Linescan of the AFM measurement (right).

The freezing waves squeeze some liquid Si outwards. The material then freezes as well to form ridges and hillocks at the grain boundaries, which can be identified in the AFM micrographs. Still, the samples crystallized with the multiple shot successive crystallization possess a rather low roughness. The root-mean-square (rms) roughness of the film shown in Fig. 5.15 is ≈ 3 nm. Fig. 5.16 shows a cross-section TEM micrograph of a sample crystallized in the SLG regime. In this case the grain size is around $1 \mu\text{m}$. The reason for this is certainly the smaller film thickness of this sample of around 80 nm. According to the SLG model a reduced film thickness reduces the SLG distance and thus the achievable grain size. The CS-TEM measurement shows that the grains are columnar, starting from the interface and extending through the whole sample. One should also note, that in this micrograph no dislocations can be identified in the grains. Similar micrographs of columnar grains were obtained for fully crystallized poly-Si processed in the partial melting regime.

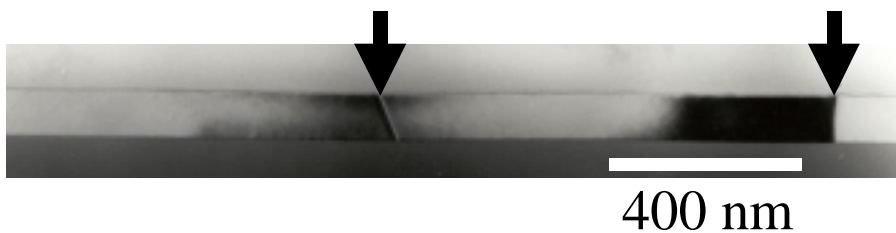


Fig. 5.16: Cross-section TEM micrograph of a poly-Si sample. The grain boundaries are marked with vertical arrows. The grains are free of dislocations.

TEM measurements were performed at the University of Erlangen to obtain detailed information on the fine structure of the grains. Fig. 5.17 is a plain view of a film crystallized in the SLG regime with an average grain size of $3.5 \mu\text{m}$. The majority of the grains are almost defect free. The average dislocations density in these grains amounts to less than $8 \times 10^6 \text{ cm}^{-2}$. Only a few grains contain a larger number of dislocations and twin lamellae (Fig. 5.18). They reveal an average dislocation density of $\approx 10^8 - 10^9 \text{ cm}^{-2}$. Twin lamellae consist of few atomic layers that are twinned with respect to the surrounding matrix.

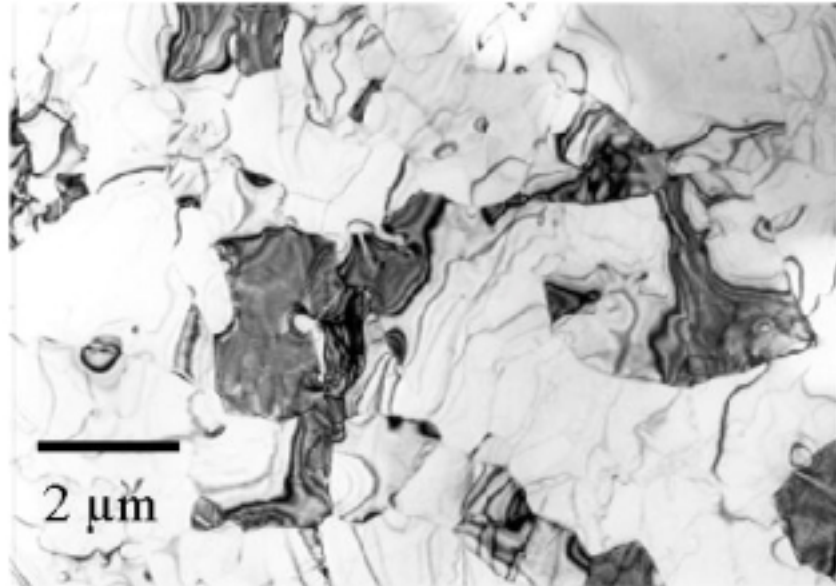


Fig. 5.17: Plan view TEM micrograph of poly-Si sample crystallized in the SLG regime. The grains can be distinguished as the areas of different gray contrast. Thin dark lines are bending contours, an unavoidable TEM artifact.

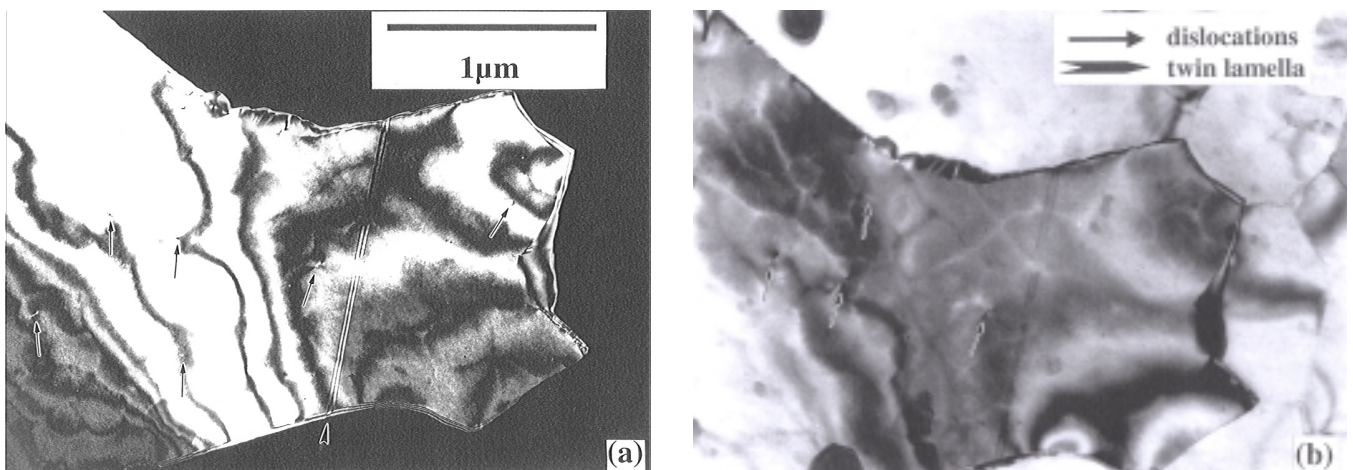


Fig. 5.18: TEM micrograph of a grain with a high dislocation density. (a) dark field, (b) bright field image.

Fig. 5.19 shows the summary of the analysis of the types of grain boundaries as measured with electron backscattering pattern (EBSP) analysis of a sample crystallized in the SLG regime. The grain boundary types are classified in the following way. Two main groups are distinguished: low- and high-angle grain boundaries. High-angle grain boundaries are either random grain boundaries, that can be described by the misorientation they cause, or coincidence grain boundaries. For coincidence grain boundaries a lattice common to both adjacent grains can be defined (coincidence site lattice [79]).

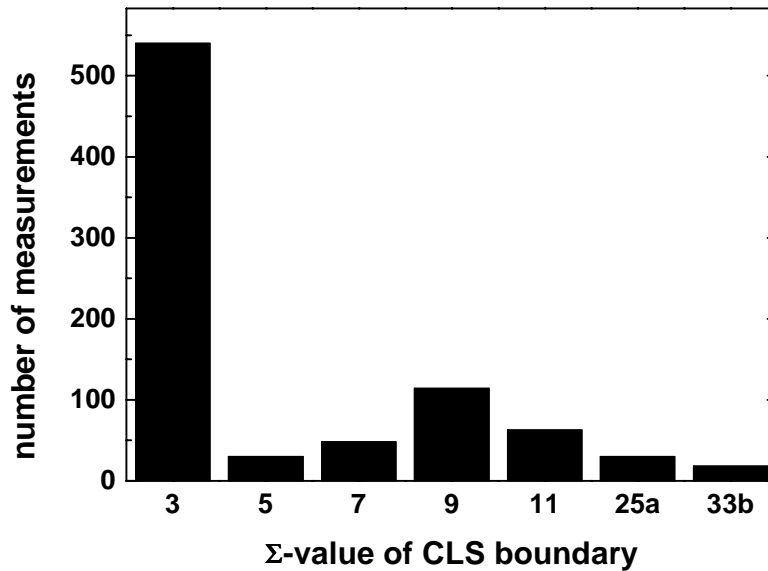


Fig. 5.19: Coincidence site lattice (CSL) parameter distribution of grain boundaries of poly-Si sample determined by electron backscattering pattern (EBSP) mapping analysis.

This purely geometric notion characterizes coincidence orientations by the Σ -parameter also called the coincidence site lattice (CSL) parameter which essentially is the reciprocal value of the coincidence sites occupied by the atoms. A full description of such a grain boundary additionally requires the identification of its contact plane in the adjacent grains. A large group of Σ -boundaries consist of twin boundaries of first order ($\Sigma 3$), second order ($\Sigma 9$), third order ($\Sigma 27$), and fourth order ($\Sigma 81$). Higher order twins form by subsequent twinning operations or by reaction of lower order twins, e.g. a $\Sigma 3$ and a $\Sigma 9$ boundary form a $\Sigma 27$ boundary, or a $\Sigma 27$ and a $\Sigma 3$ boundary form a $\Sigma 81$ boundary.

Most of the grain boundaries identified in the laser crystallized poly-Si samples are twin boundaries of first ($\Sigma 3$) or second order ($\Sigma 9$). In Fig. 5.19 roughly 65 % of all measured grain boundaries are $\Sigma 3$ boundaries, roughly 15 % are $\Sigma 9$ boundaries, and 20 % belong to other coincidence boundaries and random grain boundaries. The evaluation of other areas of the sample and other samples yield similar data. In general, 50–70 % of all grain boundaries are $\Sigma 3$ boundaries and 10–15 % are $\Sigma 9$ boundaries. $\Sigma 27$ boundaries are much less frequent and $\Sigma 81$ boundaries are rarely found. However, it has to be remembered that the EBSD analysis is limited to grains with a grain size > 500 nm. It is important to note, that low-angle grain boundaries were found only in a few cases in the form of dislocation networks superimposed on higher order twin boundaries.

In the course of this work a $\{111\}$ -preferential orientation of the grains in the direction of the surface normal was found for all undoped samples crystallized in the SLG regime. Fig. 5.20 shows a typical EBSD orientation mapping of an undoped poly-Si sample. The color code of the EBSD measurement is given as a reference. In Fig. 5.20 the blue code $[111]$ -surface normals are dominant.¹ Fig. 5.21 shows the results of several orientation mappings of this sample plotted into a stereographic triangle. Almost all surface normals are within 10° from the exact (111) -orientation, indicating a clear $\{111\}$ -preferential orientation of the grains. Again, it has to be remembered that EBSD only records the grains with a grain size larger than 500 nm. Fig. 5.22 shows a X-ray diffraction patterns of a sample, where the EBSD mappings indicated a clear $\{111\}$ -preferential orientation. The (111) -peak clearly dominates the diffractogram. The (220) - and (311) -peaks are barely visible and no signal was found at 69.1° where the (400) -peak should occur in a diffractogram of an untextured poly-Si powder. To get information on a possible preferential orientation of the grains one has to compare the ratios of the integrated intensities of the Si peaks in the measured diffractogram to literature values of these ratios in case of a completely randomly orientated poly-Si powder.

¹ In a cubic lattice such as silicon the **direction** $[hkl]$ is perpendicular to a **plane** with the identical three integers (hkl) . $\{hkl\}$ is the representation of all equivalent planes by one set of integers.

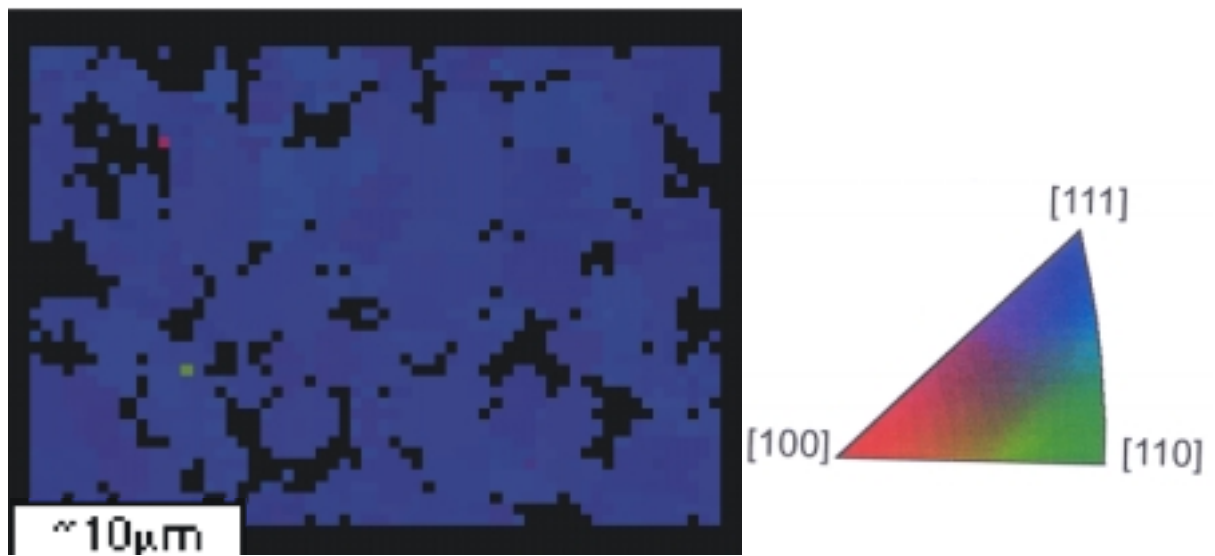


Fig. 5.20: EBSD mapping of poly-Si in surface normal direction. The color code of the measurement is given as a reference. The grains can be distinguished as patches of the same color. In the black areas the grain sizes are too small for an EBSD analysis.

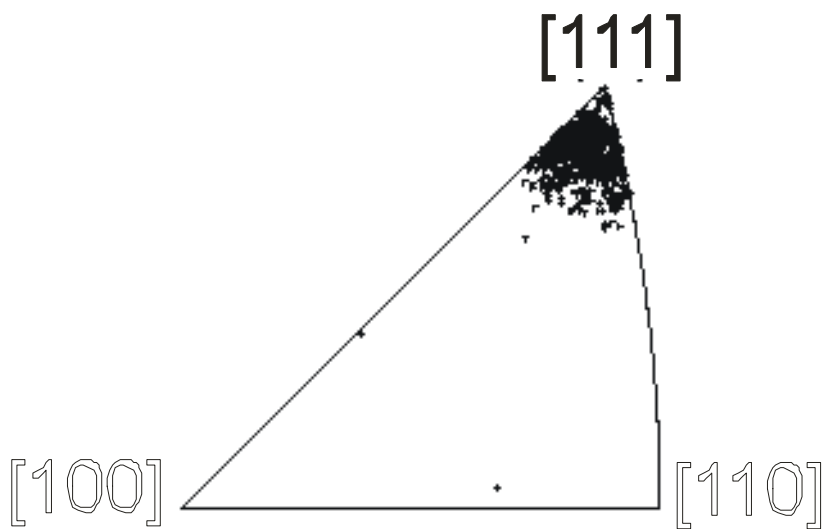


Fig. 5.21: EBSD mapping in surface normal direction summarized in a stereographic triangle. The grains possess a clear $\{111\}$ -preferential orientation.

The integrated intensities of the peaks were obtained from least squares fits of the background corrected data using splitted Lorentzian curves (also known as regular Pearson VII). However, due to the small thickness of the poly-Si samples the values of the integrated intensities of the different peaks have to be corrected to eliminate the Bragg angle dependent influence of finite absorption. This correction was performed using a thickness-dependent absorption factor A

$$A = 1 - \exp(-2\mu d / \sin\theta), \quad (5.8)$$

where $\mu = 148 \text{ cm}^{-1}$ is the absorption coefficient of $\text{CuK}\alpha$ radiation in Si [80], d is the film thickness, and θ is the Bragg angle. A derivation of A is given in the appendix of Ref. [81].

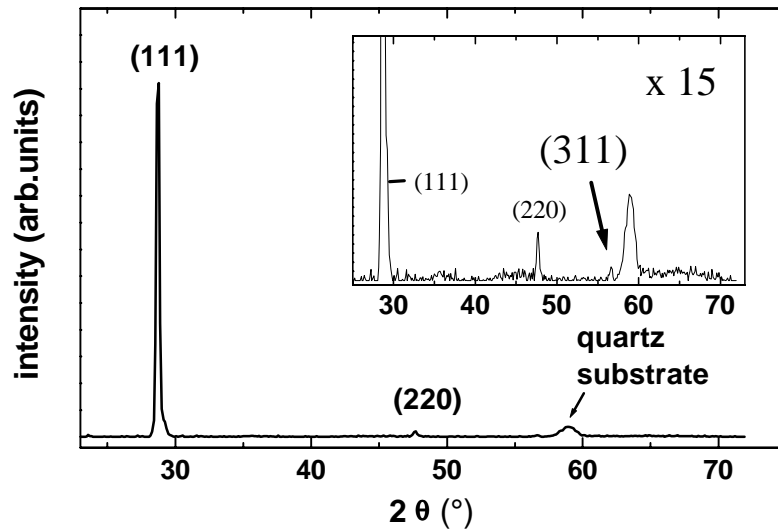


Fig. 5.22: XRD diffractogram of a poly-Si sample crystallized in the SLG regime. The (111)-peak clearly dominates the diffractogram.

The ratio of the integrated intensities of the Bragg reflections (111) and (220), $I_R = I_{(111)}/I_{(220)}$, amounts to $I_R = 32.5$. On the other hand, for a Si powder consisting of randomly orientated grains a value of $I_R = 1.82$ is obtained [82]. From the combined results of the EBSD and the XRD measurements obtained on the same sample it is evident that the grains of this sample show a dominant {111}-preferential orientation in the direction of the surface normal direction. The EBSD measurements gave no hints of a preferential orientations of the grains in any other direction than the surface normal. A

one-dimensional texture is also called fiber texture. The dominant {111}-fiber texture for undoped laser crystallized poly-Si films crystallized in the SLG regime was confirmed on several samples either by XRD or EBSP analysis. However, not all laser crystallized poly-Si samples did show a preferential orientation of the grains. For samples with a grain size smaller than 1 μm crystallized in the partial melting regime XRD measurement gave no indication of a preferential orientation of the grains (Table 5.2). Unfortunately, EBSP mapping cannot be performed on such samples because the grains are too small. Table 5.2 summarizes the XRD results obtained on undoped poly-Si. The ratios of the integrated intensities of the (220)- and (311)-reflections, $I_{(220)}/I_{(311)}$, and of the (111)- and (400)-reflections, $I_{(111)}/I_{(400)}$, are also listed in Table 5.2. It should be noted, that the (100)-peak could not be distinguished from the background for all measured samples.

Table 5.2: XRD results for different undoped samples.

Sample	Standard (Ref. [82])	Undoped poly-Si	Undoped poly-Si	Undoped poly-Si
Thickness (nm)	Powder	150	150	125
Grain size (nm)		> 3000	> 2000	200
I_{111}/I_{220}	1.82	32.46	52	1.83
I_{220}/I_{311}	1.83	2.74	2.18	1.77
I_{111}/I_{400}	16.6	$\gg 100$	$\gg 100$	$\gg 100$

Two results of the preceding section are of particular interest both regarding fundamental scientific questions and the technological relevance of the laser crystallization. These two questions are the dominance of low-order twin boundaries in the poly-Si films and the formation of a strong {111}-preferential orientation of the grains of the samples crystallized in the SLG regime. These two questions will be discussed in detail in section 6.2.

Summary

In summary, undoped poly-Si samples prepared by successive crystallization in the SLG regime have a grain size in the range of 3 - 4 μm and small roughness. Most grains possess a small dislocation density. The grain boundaries separating the grains are mostly $\Sigma 3$ and $\Sigma 9$ twin boundaries. The grains exhibit a $\{111\}$ -preferential orientation in the direction of the substrate normal. Poly-Si samples crystallized outside the SLG regime do not show a preferential orientation of the grains. According to Raman measurements a considerable amount of stress is incorporated in all the laser crystallized films originating from the glass substrates.

5.3 Influence of doping on the crystallization process and resulting material

This section presents the results on the crystallization of doped samples and the results of subsequent characterization of the doped poly-Si. There are three subsections. In the first subsection it will be shown how doping influences the crystallization process. It will be outlined how the alteration of optical and thermal properties of the heavily doped material can account for the observed changes in the crystallization process. In the second subsection the electrical properties of the doped poly-Si samples will be presented. The heavy doping of the silicon gives rise to very interesting physical effects as shown in the last subsection for the case of Raman measurements.

5.3.1 Influence of doping on the crystallization parameters

The subject of the following section is the influence of doping of the starting material *a*-Si:H on the crystallization process. The dopand concentration will in most cases be given as the nominal gas phase doping.¹ The key parameters for excimer laser crystallization are the threshold energy of crystallization or more generally the threshold energy of melting E_T and the energy to achieve super lateral growth E_{SLG} . It will be shown how these two crystallization parameters are influenced by doping.

In order to determine E_T *in situ* time resolved reflectivity (TRR) measurements were employed. Fig. 5.23 shows the TRR signals for an *a*-Si:H sample doped with a nominal gas phase doping of 1 % PH₃. Curve (a) is the signal obtained for E_L being just below E_T . The laser fluence is not high enough to induce crystallization. However, the laser light does alter the temperature in the film significantly which results in a change of the reflectivity. It should be noted, that the two distinct intensity peaks of the laser pulse are adumbrated in the shape of reflectivity curve. Curve (b) is the signal for $E_L \geq E_T$. The sharp rise of the reflectivity at $t \approx 18$ ns is caused by partial melting of the film. In the

¹ Example: A nominal gas phase doping of 1 % PH₃ means that silane was diluted with 1% PH₃.

case of a -Si the transformation process for $E_L \geq E_T$ is explosive crystallization [15]. The process is initiated by the melting of a thin a -Si layer near the surface, which resolidifies as poly-Si immediately. The latent heat released by the solidification is higher than that of melting of a -Si. As a result of the difference between the latent heat of the melting of a -Si and the latent heat of the crystallization of poly-Si a thin liquid layer propagates through the amorphous material. A brief review of explosive crystallization is given in Ref. [83].

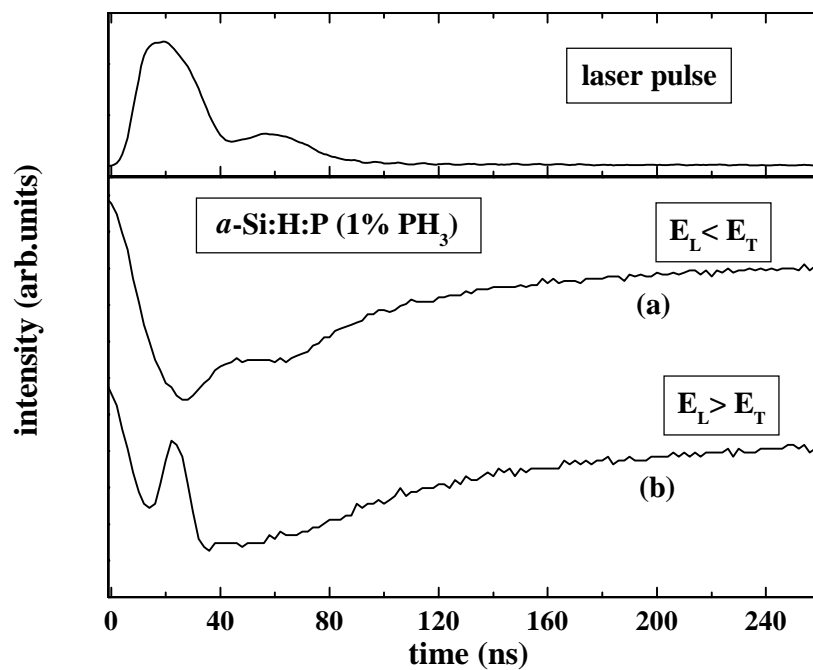


Fig. 5.23: Bottom: Time resolved reflectivity for a sample irradiated with a laser fluence below (a) and above (b) the threshold energy of melting E_T . Top: Time resolved laser pulse profile.

Fig. 5.24 shows a summary of the results obtained for E_T for various doped and undoped samples. E_T for a -Si:H is $\approx 135 \text{ mJ/cm}^2$ (solid circles). The value is independent of the film thickness in the range of 100 - 1000 nm [67]. This confirms recent theoretical calculations performed by Cerny and Prikryl for an experimental setup quite similar to ours [83]. These authors made calculations of the phase change process and its consequences on thermal and optical properties for the irradiation of a -Si layers on fused quartz substrates by a XeCl laser with a 28 ns FWHM pulse in vacuum. The cause of the thickness independence of E_T is basically that the thermal parameters of the amor-

phous films and the quartz substrate are quite similar. Cerny and Prikryl calculated a value of $E_T = 100 \text{ mJ/cm}^2$, which is slightly below the value observed in our experiments. This is not so surprising as the parameters of the calculations are close but not identical to the ones of our experimental setup.¹ More importantly, Cerny and Prikryl did not state explicitly whether they used the optical and thermal parameters of *a*-Si or *a*-Si:H. As can be seen in Fig. 5.24 E_T of dehydrogenated undoped *a*-Si (half solid circle)² has a value of 157 mJ/cm^2 , which is considerably higher than in the case of the *a*-Si:H samples.

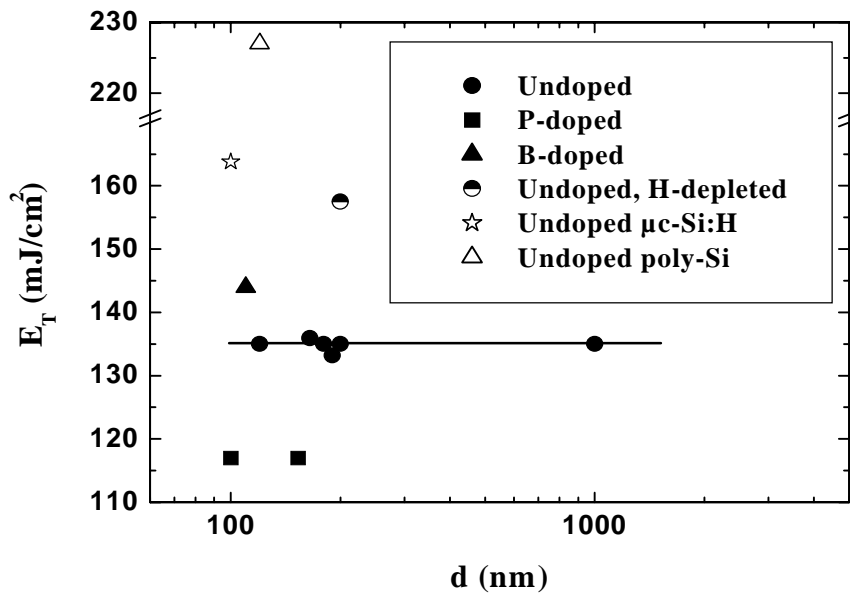


Fig. 5.24: Threshold energy of crystallization E_T for various samples. In case of undoped samples E_T is independent of the film thickness. The line is a guide to the eye. Heavy doping of *a*-Si influences E_T . The nominal gas phase doping of the doped samples shown in this figure is $\geq 0.5\%$.

E_T of an undoped hydrogenated microcrystalline silicon ($\mu\text{c-Si:H}$) sample (open star) and of an undoped poly-Si sample (open triangle) are also shown in Fig. 5.24. The values for E_T amount to 165 mJ/cm^2 and 227 mJ/cm^2 for $\mu\text{c-Si:H}$ and poly-Si, respectively. The main reason why E_T is higher for these materials than in the case of undoped *a*-Si:H is the difference in melting temperature and thermal conductivity of amorphous and

¹ Just to name one point, the actual pulse shape (Fig. 3.2) consisting of two peaks would have to be taken into account to get a precise copy of the experimental conditions of this work.

² The hydrogen was removed by a conventional vacuum furnace at 500°C for about four hours.

crystalline silicon. It should be noted, that if the starting material is crystalline no explosive crystallization can occur and the film is just molten by the laser light. As the $\mu\text{-Si:H}$ shown in Fig. 5.24 has a Raman crystallinity of $< 80\%$ it is reasonable, that the value E_T is smaller than that of the poly-Si sample.

Heavy doping of the starting material $a\text{-Si:H}$ has a considerable effect on E_T [84]. The nominal gas phase doping of the samples shown in this figure is $\geq 0.5\%$. In the case of phosphorous doping E_T is reduced to 117 mJ/cm^2 , while in the case of boron doping E_T increases to approximately 145 mJ/cm^2 .

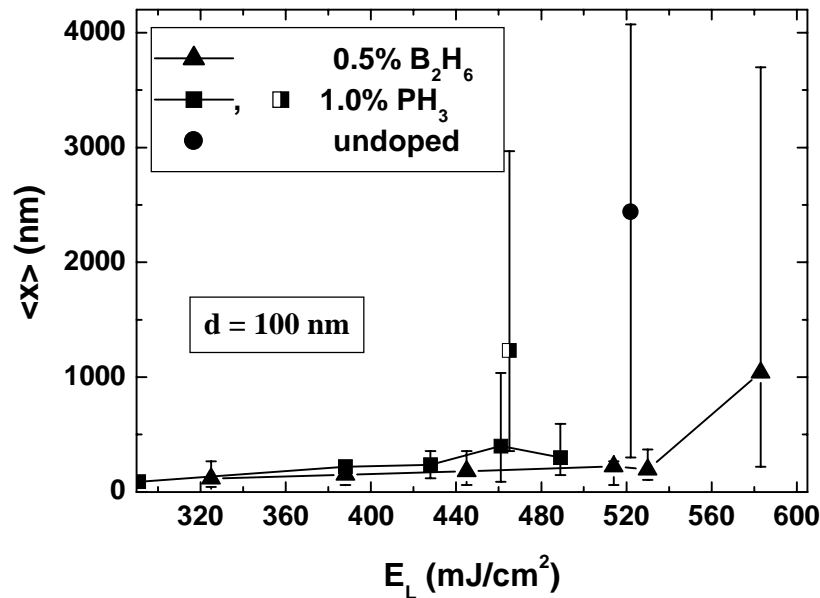


Fig. 5.25: Variation of the laser fluence to achieve super lateral growth E_{SLG} with doping.

The second key crystallization parameter, E_{SLG} , is also influenced by heavy doping as shown in Fig. 5.25 [84]. In this figure the dependence of the average grain size of the poly-Si samples on the laser fluence is shown for samples of identical film thickness but different doping. The squares represent heavily phosphorous doped samples, while the triangles represent the heavily boron doped sample. For P doping results from two samples are shown. For the second sample only the data point of E_{SLG} is given, to supplement the data of the first sample. The vertical bars in the figure indicate the minimum and maximum grain size found for the specified laser fluence. E_{SLG} of an un-

doped sample of identical thickness is included in Fig. 5.25 as a reference (solid circle; complete data set is shown in Fig. 5.8). As the data in Fig. 5.25 show, heavy doping influences the energy to achieve super lateral growth considerably. In case of heavy P doping E_{SLG} is reduced by about 60 mJ/cm^2 to a value of 460 mJ/cm^2 with respect to the undoped sample. In case of B doping the opposite is true. E_{SLG} is increased by about 60 mJ/cm^2 to a value of 580 mJ/cm^2 with respect to the undoped sample. The shift of E_{SLG} with doping is considerably higher compared with an observed shift of 35 mJ/cm^2 of E_{SLG} in case of excimer laser crystallization of 100 nm thick undoped a -Si at substrate temperatures of 673 K and 300 K [70]. It is interesting to notice that the influence of heavy doping is similar for E_{SLG} and E_T . Both crystallization parameters are decreased by heavy P doping and increased by heavy B doping compared to the case of an undoped sample. The data presented in Fig. 5.25 indicate that the grain size which can be achieved in heavily doped poly-Si is smaller than for undoped samples of identical film thickness. In heavily B and P doped poly-Si a maximum average grain size of approximately $1 \mu\text{m}$ is obtained, while the average grain size of the undoped poly-Si amounts to $3.5 \mu\text{m}$.

One possible origin of the variation of the crystallization parameters with doping could be a change of the optical properties. A significantly enhanced or reduced reflectivity for light of the wavelength of the excimer laser would result in a change of the amount of energy deposited in the film and thus to a change of the crystallization parameters E_T and/or E_{SLG} . E_T is influenced by the optical properties of a -Si:H, while E_{SLG} is influenced by the optical properties of poly-Si, as the films are already fully crystallized when the laser fluences reach the values for super lateral growth in the course of successive crystallization. To check the influence of the optical properties the reflectivity of heavily doped and undoped amorphous and crystallized samples were measured. The results of the reflectivity at the wavelength of the excimer laser are shown in Fig. 5.26 for a -Si:H (solid symbols) and for poly-Si (open symbols). The changes in the reflectivity are not significant enough to sufficiently account for all the observed changes in E_T and E_{SLG} . Additionally, the small changes of reflectivity which are observed have not the same trend as the changes of the crystallization parameters. On the other hand, the reflectivity of the H depleted a -Si is significantly enhanced compared to the reflectivity of undoped a -Si:H. The increase of the reflectivity of about 10% explains the

increase of E_T of the H depleted a -Si compared to the E_T of a -Si:H. The higher reflectivity of poly-Si in comparison to a -Si:H causes an additional increase of E_T for poly-Si compared to a -Si:H.

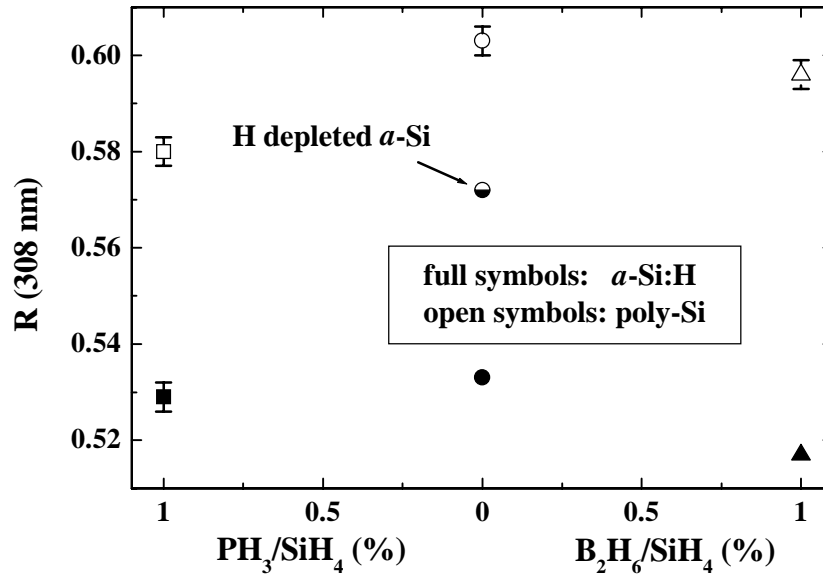


Fig. 5.26: Optical reflection data of undoped and doped a -Si:H and poly-Si at $\lambda = 308$ nm.

It is conceivable that the influence of doping on the crystallization process is due to a change of the thermal conductivity of the material. A change of the thermal parameters would alter the laser energy distribution in the films. A lower thermal conductivity of the material results in a higher temperature in the surface region of the material where the excimer light is absorbed. In consequence, the threshold energy of crystallization (melting) is reduced. Thus, a change of the thermal conductivity of heavily doped a -Si:H can explain the modification of E_T . In case of E_{SLG} the picture is similar, only that now the thermal conductivities of poly-Si and possibly molten Si are relevant. In the course of the successive crystallization procedure the samples are already crystallized in the crystallization steps prior to the last step, when the energy to achieve super lateral growth is reached.

A change of the thermal parameters of the starting material was not considered by Im *et al.* in the original model of the super lateral growth process [19]. Instead, a change of the thermal parameters of the substrate is considered. The model predicts that a de-

creased thermal conductivity of the substrate leads to a decrease of E_{SLG} [19]. The situation should be similar for the thermal properties of the films. A decreased thermal conductivity of poly-Si, and possibly of liquid silicon would lead to a reduction of E_{SLG} . Hence, the predictions from the above hypothesis is that heavy phosphorous and boron doping reduces and increases the thermal conductivity of poly-Si and/or molten silicon, respectively. Similarly, a reduced thermal conductivity of the film would decrease the threshold energy of melting E_T . In this case the prediction is that heavy phosphorous doping should lead to a decrease of the thermal conductivity of a -Si:H, while boron doping should result in an increases of the thermal conductivity.

Unfortunately, it was not possible to measure thermal conductivities of thin film silicon films in the course of this work. Experimentally this is challenging since the samples are very thin, so that the substrate will significantly influence any experiment. Experimental data by other groups on thermal conductivity of highly doped silicon is scarce. However, there is a work by Slack, who measured thermal conductivity of heavily doped crystalline silicon [85]. Slack investigated a c-Si sample with a P concentration of $1.7 \times 10^{20} \text{ cm}^{-3}$ and one with a B concentration of $5 \times 10^{20} \text{ cm}^{-3}$. In both cases the thermal conductivity at room temperature was significantly reduced compared to the case of undoped silicon. The physical reason for the observed decrease in thermal conductivity given by Slack is that the electrically active impurities cause scattering of the phonons responsible for the heat transport. Slack estimates that samples with maximum P and B impurity concentrations of $\approx 10^{21} \text{ cm}^{-3}$ will have a thermal conductivity K at room temperature of $K \approx 0.1 - 0.2 \text{ W}/(\text{cm}\cdot\text{K})$, which is about a factor of 10 smaller than the value for pure crystalline silicon of $K \approx 1.4 \text{ W}/(\text{cm}\cdot\text{K})$. However, Slack's data indicates that this difference becomes smaller with increasing temperature. The data by Slack support the interpretation of the influence of the heavy doping on E_{SLG} in case of P doping. As the undoped silicon samples used in this work contain considerably more impurities as high purity c-Si the decrease in K will probably be less than a factor of 10, but will most certainly be high enough to account for the experimental observations. In case of B doping the data by Slack indicate that the above hypothesis in this case is wrong. In consequence, the question of the influence of heavy B doping on the crystallization process can not be fully resolved with the existing experimental data. For

a-Si:H no reliable data for K of heavily doped samples are available, to the best of the authors knowledge. However, it is rather likely that there is also a significant influence of heavy doping on the thermal conductivity of *a*-Si:H.

According to the SLG model an increase or decrease of the thermal parameters of the substrate also influences the SLG distance, i.e. the grain size of the resulting films. The SLG distance increases as the thermal conductivity of the substrate decreases. So a decrease of K in case of P doping should result in an increase of the SLG distance resulting in larger grains with respect to undoped films of identical thickness. Experimentally a decrease of the average grain size is observed for both heavy P and B doping. However, the experimental results for the P doped samples also point to a reduced FWHM of the SLG peak. Hence, it is possible that the actual E_{SLG} was slightly missed.¹ Thus the experimentally observed average grain size might not reflect the actual SLG distance.

Moderate and heavy doping levels do not influence the preferred orientation of the grains of films crystallized in the super lateral growth regime. Fig. 5.27 shows the summary of EBSP-orientation mapping for moderately P- and B-doped films, which were crystallized in the super lateral growth regime. Fig. 5.28 shows the corresponding EBSP results for heavy doping. The EBSP mapping results show clearly that for moderately and heavily doped poly-Si samples crystallized in the super lateral growth regime a pronounced {111}-preferential orientation of virtually all large grains is achieved.

¹ This does not significantly change the value of E_{SLG} .

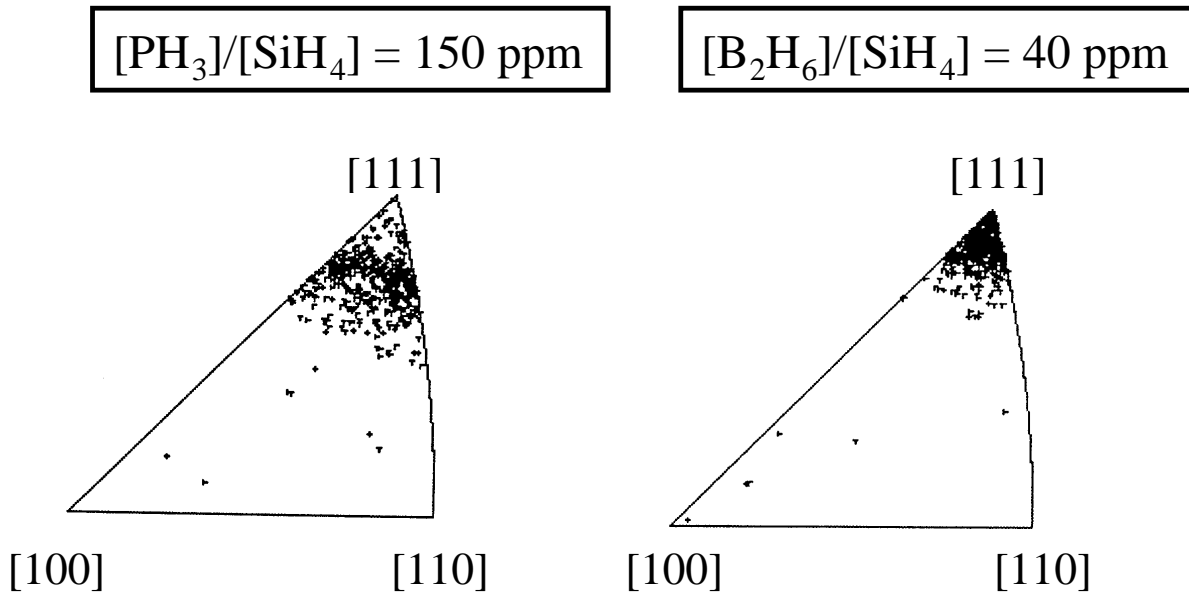


Fig. 5.27: Grain orientations in surface normal direction as measured by EBSD mapping for moderately doped poly-Si samples.

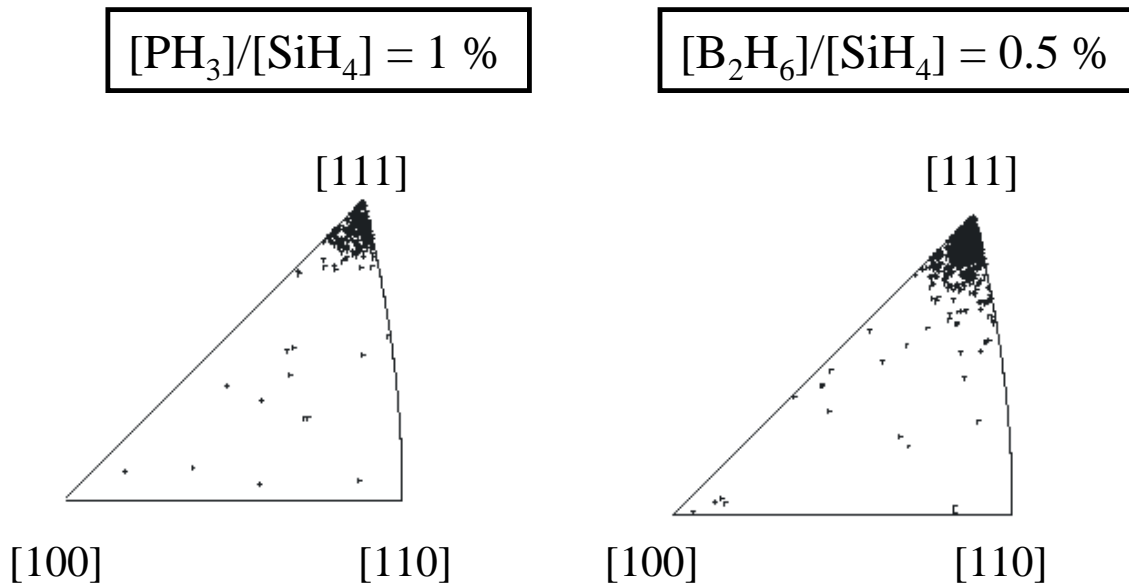


Fig. 5.28: Grain orientations in surface normal direction as measured by EBSD mapping for heavily doped poly-Si samples.

5.3.2 Electrical properties of doped poly-Si

The room temperature electrical data for various P and B doped poly-Si samples are summarized in Table 5.3. Doping in the gas phase leads to deposition of amorphous material with a high concentration of phosphorous or boron atoms. As shown by the Hall measurements after the laser crystallization a large fraction of the donor or acceptor atoms are electrically active, thus leading to a very high concentration of free carriers in the crystallized samples.

Table 5.3: Hall results for different heavily doped laser crystallized poly-Si samples

Type	[PH ₃]/[SiH ₄] [B ₂ H ₆]/[SiH ₄] (ppm)	σ (S/cm)	n/p (cm ⁻³)	μ_H (cm ² /Vs)
n	500	3.6×10^1	5.2×10^{19}	4.3
n	2000	6.7×10^2	3.8×10^{20}	11
n	10000	2.6×10^3	1.7×10^{21}	9.7
p	100	2.7×10^0	8×10^{18}	2
p	1000	1.0×10^2	8.6×10^{19}	7
p	5000	1.6×10^3	3.3×10^{20}	12

The free carrier concentration of the samples with a nominal doping of 1 % PH₃ appear to be very high. It is possible that the Hall measurements are to some extent influenced by the rather small thickness of the samples ($d = 100 - 130$ nm). A second possible source of error is the so-called Hall scattering factor, which was set to 1 for the determination of the free carrier concentrations in these experiments. On the other hand, the Hall scattering factor for ionized impurity scattering is 1.93 [54] which would result in an even higher free carrier concentration. The increase of the free carrier concentrations clearly follows the trend of the nominal gas phase doping.

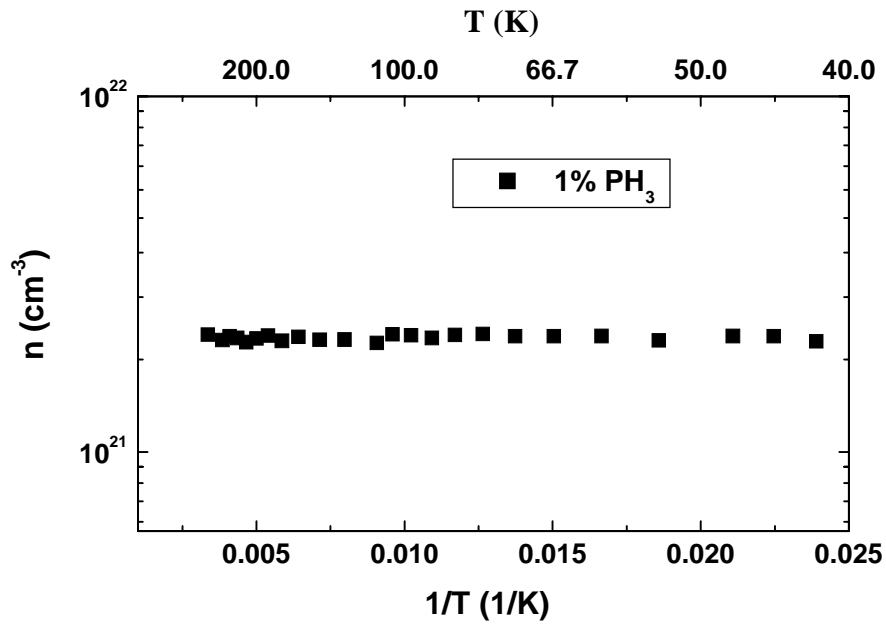


Fig. 5.29: Temperature dependence of free carrier concentration. The free carrier concentration is not dependent on temperature. The poly-Si is degenerate.

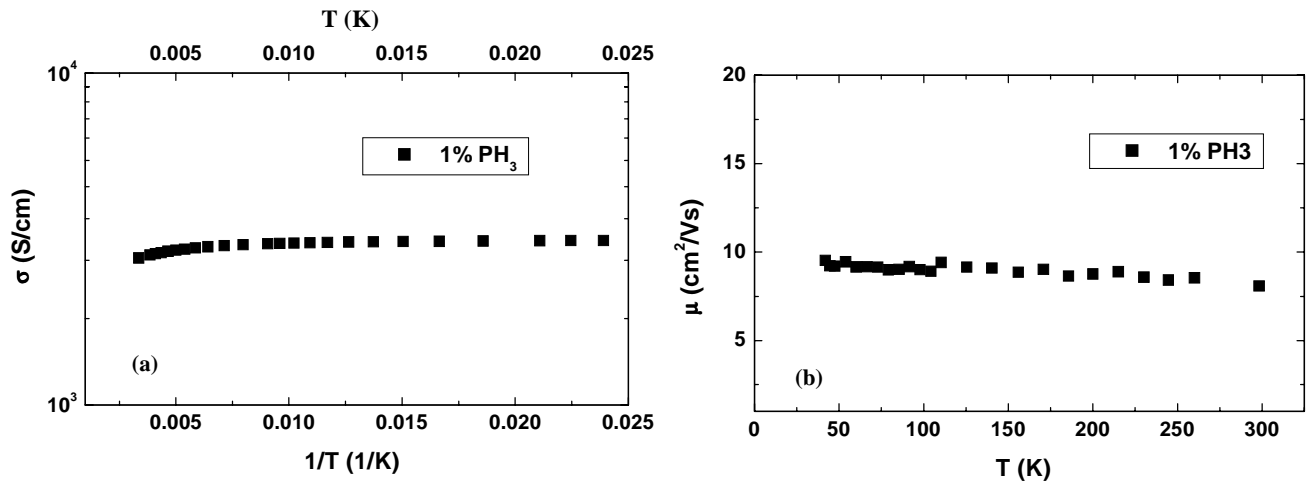


Fig. 5.30: Temperature dependence of conductivity (a), and Hall mobility (b).

EDS measurements on two samples with a nominal gas phase doping of 1 % PH_3 and a thickness of 100 nm and 1000 nm indicated a concentration of P atoms of approximately $9.5 \times 10^{20} \text{ cm}^{-3}$. So it can be assumed that the Hall measurements do actually reflect the correct free carrier concentration with a possible maximum error of factor 2 for the highest P concentrations. According to the Hall measurements the doping efficiency for this process, i.e. the ratio of the supply of dopand atoms in the gas phase to the amount of electrically active atoms in the poly-Si is larger than 1, being about 1.5 in case of B and larger than 2 in case of P doping.

For the highest doping levels the concentration of free carriers shifts the Fermi energy into the conduction and valence band for n- and p-type doping, respectively. The poly-Si samples are degenerate and should exhibit quasi-metallic electric properties. This is confirmed by temperature-dependent Hall effect measurements for a heavily P doped sample (Fig. 5.29, Fig. 5.30 (a),(b)). The concentration of free electrons n (Fig. 5.29), the conductivity σ (Fig. 5.30 (a)) and consequently the Hall mobility μ_H (Fig. 5.30 (b)) are independent of the temperature in the range of 40 - 300 K.

The very high concentrations of free carriers and the resulting high conductivities on the order of several 10^3 S/cm should make it possible to use the heavily doped poly-Si samples as contact layers in solar cells without an additional metal contact. This assumption was tested by fabricating a solar cell using highly P doped poly-Si as a seed layer for a subsequent deposition. The solar cell worked showing an efficiency of about 1 %. The poor efficiency is most certainly caused by the high defect density of the absorber. CS-TEM images of the solar cell showed that no significant epitaxial growth was achieved on the seed layer. This is not surprising given the lack of a {100}-preferential orientation of the grains and the results of low-temperature epitaxy using ECR-CVD on crystalline silicon wafers [27].

5.3.3 Influence of doping on Raman spectra of poly-Si

Fig. 5.31 and Fig. 5.32 show the Raman spectra of a successive crystallization sequence of a heavily phosphorous and heavily boron doped film, respectively. In both cases the nominal doping was 1 %. In case of the P doped sample the crystalline LO-TO phonon peak emerges just as in the case of the successive crystallization of undoped a -Si:H. However, the LO-TO phonon line is asymmetrically broadened which can be clearly seen in the spectra of the samples crystallized with higher final laser fluences.

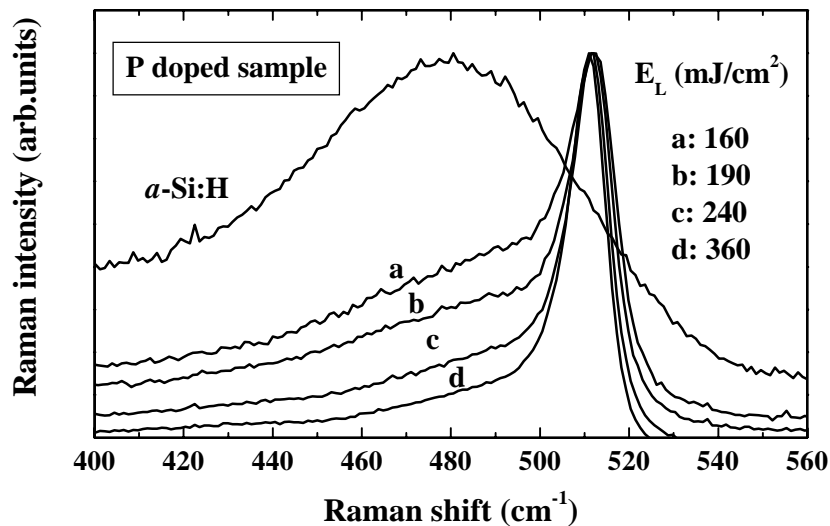


Fig. 5.31: Raman spectra of successive crystallization sequence of heavily P doped a -Si:H.

The curve of the sample crystallized with the highest final laser fluence is similar to a spectrum of undoped μ c-Si:H suggesting the presence of a residual amorphous phase. This, however, is not the case here. As demonstrated in section 5.1 undoped amorphous samples with a thickness of 120 nm are fully crystallized for laser fluences ≥ 330 mJ/cm². Thus, the asymmetric broadening of the LO-TO phonon mode are caused by the phosphorous doping. The successive crystallization of a heavily boron doped amorphous sample (Fig. 5.32) reveals an even more unusual line shape of the LO-TO phonon. The emerging LO-TO phonon line is strongly asymmetric and the curve of the

fully crystallized samples exhibits a pronounced minimum. The only difference between the samples shown in Fig. 5.31 and Fig. 5.32 and the standard samples of this work are the high doping concentrations. Therefore, this section is devoted to a detailed study of the influence of the free carrier concentration on the Raman spectra of the poly-Si films.

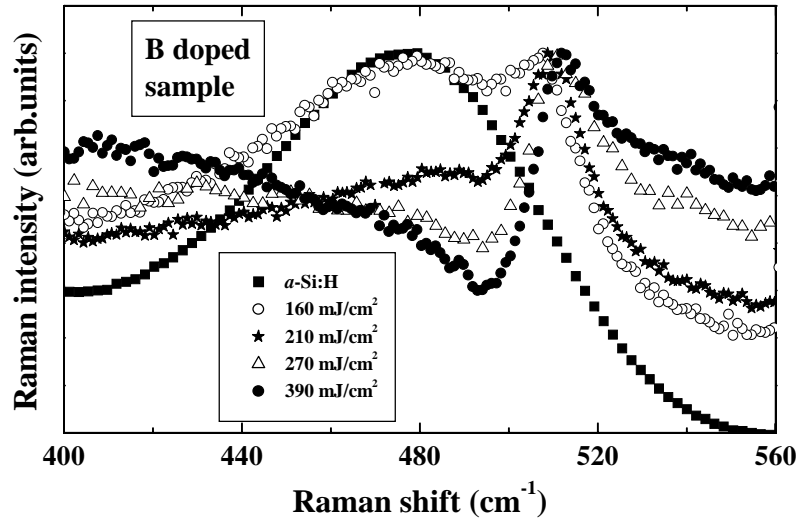


Fig. 5.32: Raman spectra of successive crystallization sequence of heavily B doped *a*-Si:H.

In Fig. 5.33 Raman backscattering data of the LO-TO phonon mode of phosphorous doped polycrystalline silicon are shown as a function of the P concentration. Fig. 5.33 shows the original Raman spectra, recorded under identical conditions. For clarity the spectra are shifted horizontally. All samples shown in Fig. 5.33 have a thickness in the range of 100 - 110 nm and an average grain size of approximately $\langle x \rangle \approx 400$ nm.

The line shape of the LO-TO phonon line is significantly altered by the phosphorous doping [86]. With increasing P concentration a broad low-energy tail extending from 400 cm^{-1} to 500 cm^{-1} develops. In undoped microcrystalline silicon this broad low-energy tail is commonly attributed to the presence of a residual amorphous phase. All samples shown in Fig. 5.33 were crystallized with a laser fluence of $\geq 400 \text{ mJ/cm}^2$ high enough to obtain single phase poly-Si.

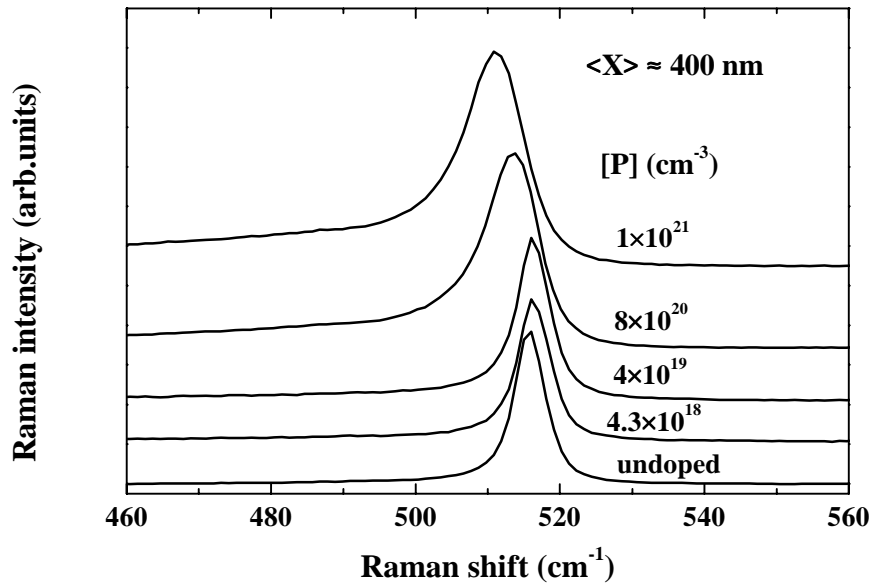


Fig. 5.33: Dependence of asymmetry on phosphorous concentration. Raman spectra were recorded under identical conditions. For clarity the spectra are shifted horizontally.

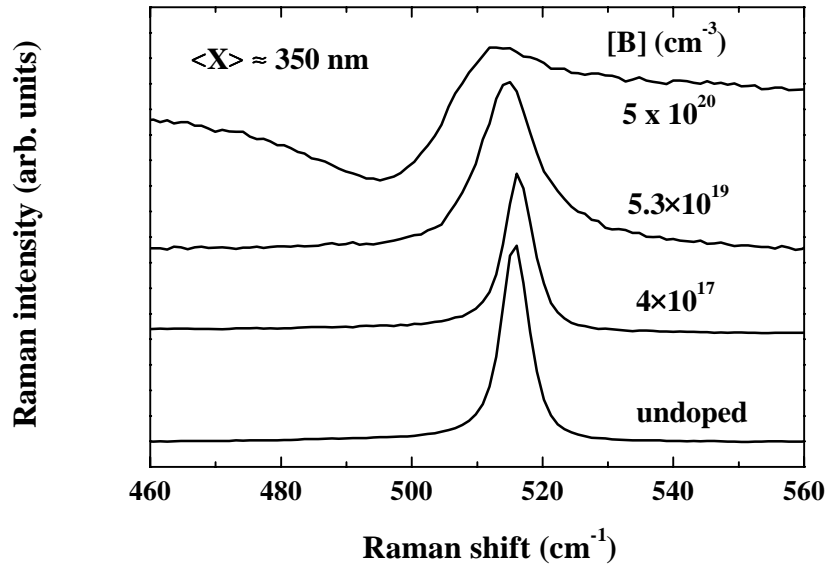


Fig. 5.34: Dependence of asymmetry on boron concentration. Raman spectra were recorded under identical conditions. For clarity the spectra are shifted horizontally.

As shown in section 5.2 the peak position of the LO-TO phonon line of undoped laser crystallized films on quartz is shifted with respect to the position of the LO-TO phonon of c-Si (521 cm^{-1}) by about 5 wave numbers to 516 cm^{-1} . With increasing P concentration an additional shift of the LO-TO phonon line is observed. For the highest P concentration the LO-TO phonon line is centered at 511 cm^{-1} . The asymmetric broadening of the LO-TO phonon mode, as well as the additional peak shift are caused by the P doping.

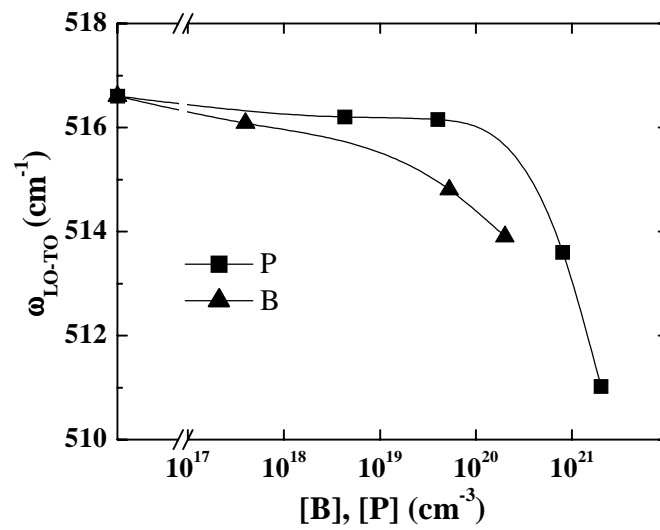


Fig. 5.35: Dependence of the (apparent) LO-TO phonon peak positions on P and B concentrations. The lines are guides to the eye.

Raman backscattering spectra of boron doped laser crystallized poly-Si are compiled in Fig. 5.34 as a function of the B concentration [86]. All samples shown in Fig. 5.34 have a thickness in the range of 100 - 110 nm and an average grain size of approximately $\langle x \rangle \approx 350 \text{ nm}$. For a B concentration exceeding $5 \times 10^{19} \text{ cm}^{-3}$ the LO-TO phonon mode is asymmetrically broadened. However, this time the tail is situated on the high-energy side of the peak. For the sample with a B concentration of about $5 \times 10^{20} \text{ cm}^{-3}$ the spectrum exhibits a pronounced minimum centered at 494 cm^{-1} in addition to a maximum centered at 514 cm^{-1} .

Fig. 5.35 shows the shift of the apparent peak of the LO-TO phonon as a function of the P (squares) and B (triangles) doping concentration. For the strongly asymmetric B doped poly-Si sample the maximum of the asymmetric spectrum was taken as the apparent peak position of the LO-TO phonon mode. Also in the case of B doping the peak position of the LO-TO phonon exhibits an additional shift with respect to the undoped samples which becomes more pronounced with increasing doping level.

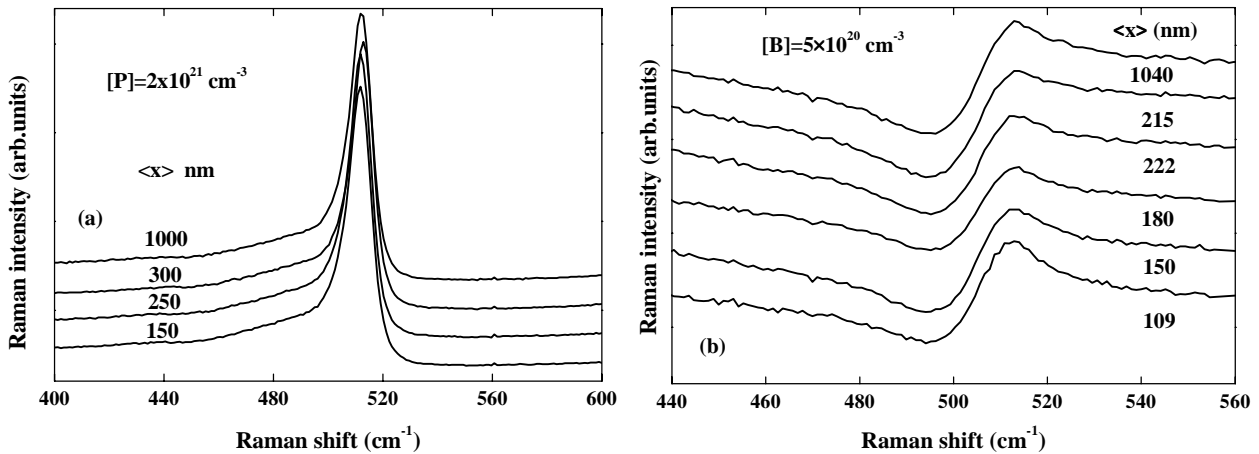


Fig. 5.36: Dependence of asymmetry on grain size for P (a) and B (b) doping. The grain size does not influence the asymmetric broadening.

The grain size of the laser crystallized samples does not influence the asymmetric broadening as shown in Fig. 5.36 (a) and Fig. 5.36 (b) for a heavily phosphorous and a heavily boron doped sample, respectively. No significant influence on either the apparent peak position of the LO-TO phonon mode or on the asymmetry of the curve can be seen.

The asymmetric broadening of the LO-TO phonon line depends strongly on the wavelength of the Raman excitation laser. This is shown in Fig. 5.37 for a heavily boron doped poly-Si sample. In case of the excitation with the 633 nm HeNe laser the asymmetry is very strong, while it is clearly diminished in the spectrum taken with the 458 nm Ar⁺ laser line.

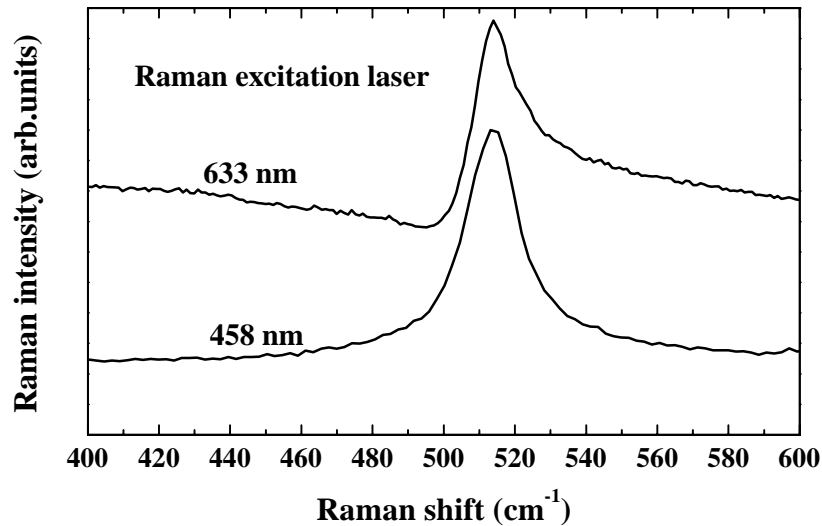


Fig. 5.37: Influence of different Raman excitation laser wavelengths on the asymmetry of the LO-TO phonon in case of heavily B doped poly-Si. The asymmetric broadening is diminished in case of the Raman excitation with $\lambda = 458$ nm.

As the Raman spectra of all heavily doped poly-Si samples show a strong asymmetric broadening of the LO-TO phonon the question arises, whether one can observe a similar effect in as-deposited heavily doped microcrystalline silicon. Fig. 5.38 shows the Raman spectrum of a heavily P doped $\mu\text{c-Si:H}$ film (nominal gas phase doping $> 1\%$ PH_3 , $d = 230$ nm). For comparison, the spectrum of the same film is shown after laser crystallization.¹ The fully crystallized sample shows the asymmetric broadening analogous to the highly P doped poly-Si samples crystallized with $a\text{-Si:H}$ as starting material. If one just considers the region around 500 cm^{-1} in the vicinity of the LO-TO phonon mode the spectrum of the as-deposited P doped $\mu\text{c-Si:H}$ does show some similarities to the asymmetrically broadened spectrum of the crystallized sample.

¹ All Raman measurements shown in this paragraph were performed with the HeNe laser.

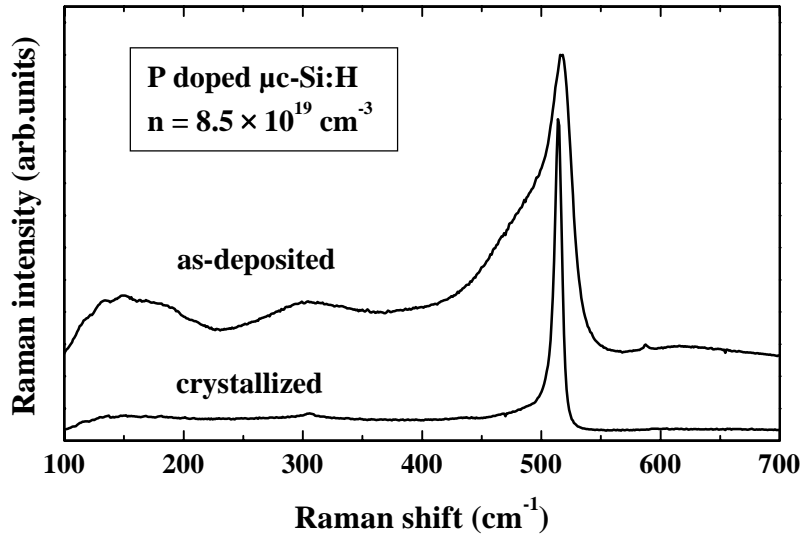


Fig. 5.38: Raman spectrum of highly P doped $\mu\text{c-Si:H}$ in the as-deposited state and after laser crystallization. The asymmetry of the LO-TO phonon line seen in the crystallized sample is obscured by the amorphous contribution in case of the as-deposited sample.

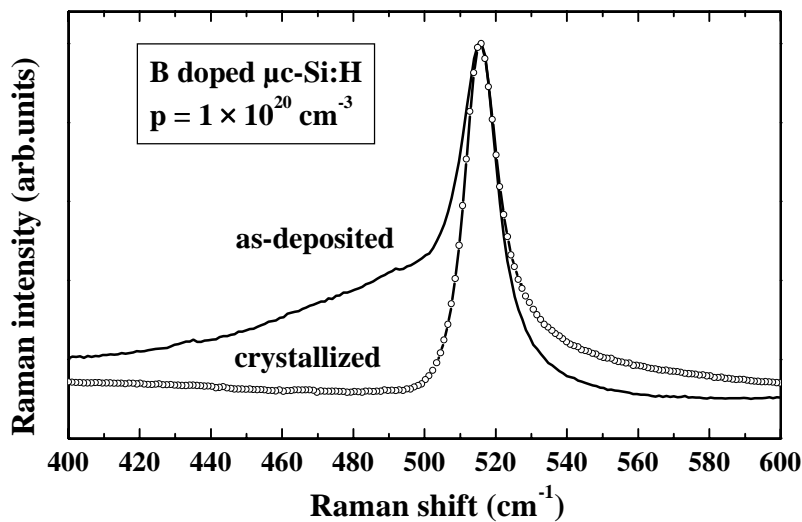


Fig. 5.39: Raman spectrum of highly B doped $\mu\text{c-Si:H}$ in the as-deposited state and after laser crystallization. While the curve of the crystallized sample shows a strong asymmetric broadening on the high-energy side of the LO-TO phonon line, no such feature can be found in the as-deposited sample.

However, as can clearly be seen at lower wave numbers the spectrum of the $\mu\text{c-Si:H}$ contains a considerable amount of amorphous contributions (broad features at 150 cm^{-1} and 300 cm^{-1}). Hence, it is not surprising that the LO-TO-peak near 521 cm^{-1} is asymmetrically broadened, since the residual amorphous phase contributes the broad TO phonon line around 480 cm^{-1} .

The Raman spectrum of a highly boron doped $\mu\text{c-Si:H}$ sample (nominal doping $> 0.3\%$ B_2H_6 , $d \approx 160\text{ nm}$) is shown in Fig. 5.39. For comparison, the spectrum of the same sample is shown after laser crystallization. The fully crystallized sample shows the asymmetric broadening analogous to highly boron doped poly-Si crystallized with $\alpha\text{-Si:H}$ as starting material. On the other hand, the as-deposited B doped $\mu\text{c-Si:H}$ sample shows no significant broadening on the high energy side of the LO-TO phonon peak (Fig. 5.39). Again, the sample contains a considerable amount of amorphous silicon as indicated by the broad features around 480 cm^{-1} , as well as in the vicinity of 150 cm^{-1} and 300 cm^{-1} .

At the end of this subsection, the explanation of the asymmetric broadening of the LO-TO phonon lines in heavily P and B doped poly-Si shall be mentioned. The asymmetric broadening of the LO-TO phonon lines of the heavily doped poly-Si are caused by the Fano effect [31]. Cerdeira *et al.* [29] and Chandrasekhar *et al.* [30] investigated the Fano effect in Raman measurements for heavily p- and n-type crystalline silicon, respectively. The subject will be discussed in full detail in section 6.3.

Summary

Doping has a significant influence on the crystallization process. Heavy P and B doping lead to a decrease and an increase of the two characteristic crystallization parameters E_T and E_{SLG} , respectively. The influence of heavy doping on the two characteristic crystallization parameters is assumed to be mainly caused by a change of the thermal properties of the material. The free carrier concentration in heavily doped films exceeds $5 \times 10^{20}\text{ cm}^{-3}$ for P and B doping. The high doping levels have a strong impact on the Raman spectra of the poly-Si, leading to asymmetric broadening of the LO-TO phonon line caused by the Fano effect.

6 Discussion

In the preceding section it was shown that it is possible to produce high-quality undoped and doped poly-Si with successive laser crystallization. Several results obtained in the course of this work have to be discussed in detail. The first is the experimental observation that the hydrogen local vibrational mode at 2000 cm^{-1} decreases faster in the course of successive crystallization than the hydrogen mode at 2100 cm^{-1} . This result will be discussed in terms of the hydrogen cluster model and it will be shown that the assignment of the hydrogen mode at 2100 cm^{-1} to platelet-like hydrogen clusters leads to an explanation of this observation. In the second part the dominance of first and second order twin boundaries in laser crystallized poly-Si will be discussed. A model for the texture formation of the laser crystallized poly-Si is developed. The last section contains a detailed treatment of the Raman spectra of heavily doped poly-Si in terms of Fano resonances. The question of whether such Fano broadenings can also be observed in the spectra of heavily doped as-deposited $\mu\text{c-Si}$ will be addressed. It will be shown that the Raman spectra of heavily doped samples can give a strong indication on whether the investigated material should be regarded as microcrystalline or polycrystalline silicon.

6.1 Si-H dissociation during successive crystallization

In the course of the successive crystallization an enhanced dissociation of the local vibrational mode at 2000 cm^{-1} in comparison with the dissociation of the mode at 2100 cm^{-1} was observed (Fig. 5.6, section 5) leading to an increase of the microstructure parameter R^* from 0.37 to 0.6 [67]. Such a result has not been reported before to the best of the authors knowledge. However, there is a report by Zellama *et al.* on annealing experiments of *a-Si:H* prepared under different deposition conditions [87]. In these experiments *a-Si:H* samples were annealed at various temperatures up to $600\text{ }^\circ\text{C}$ for 30 min and IR absorption measurements were performed before and after the annealing.

Zellama *et al.* found that in case of *a*-Si:H deposited under standard conditions the hydrogen concentration c_{HI} obtained from the integrated intensity of the IR hydrogen mode at 2000 cm^{-1} started to decrease at lower temperatures than the concentration of c_{H2} obtained from the integrated intensity of the mode at 2100 cm^{-1} .

In order to explain these experimental results it is necessary to understand the origin of the two local vibrational modes at 2000 cm^{-1} and 2100 cm^{-1} . Already in the late 1970's the modes at 2000 cm^{-1} and 2100 cm^{-1} were assigned to stretching vibrations of Si-H and Si-H₂ based on detailed IR analysis of gaseous silanes in comparison with spectra of *a*-Si:H and *a*-Si:D samples [88]. The assignment of the 2000 cm^{-1} -mode to isolated monohydride is undisputed in the literature. On the other hand, the dihydride assignment for the mode near 2100 cm^{-1} has been subject of discussion for some years. Various groups relate the mode at $\approx 2100\text{ cm}^{-1}$ to clustered Si-H_x groups (predominately dihydride) residing in larger cavities (voids) [89-91]. Several investigations clearly demonstrate that the H bonding configurations are significantly influenced by the absolute hydrogen concentrations in the sample and by the deposition conditions ([91] and references therein). Depending on the type of material the microstructure parameter R^* can increase significantly ($R^* > 0.6$) with increasing hydrogen content, typically as a result of a decreased deposition temperature. The strong increase of R^* is accompanied by the appearance of IR dihydride bending modes at 840 cm^{-1} and 880 cm^{-1} , see e.g. Ref. [92, 93]. Such material is considered to contain a significant amount of interconnected voids. The clustered Si-H_x in these interconnected voids is believed to be the cause of a characteristic low-temperature peak in H effusion experiments [91, 94, 95], indicating that the H in these voids is loosely bonded.

At face value the attribution of the mode at 2100 cm^{-1} to loosely bonded Si-H_x in interconnected voids seems to be in contrast to the results obtained in this work and to the results reported by Zellama *et al.* [87]. However, this need not be the case. All *a*-Si:H samples investigated in this work were prepared under standard PECVD conditions with substrate temperatures in the range of 200 - 250 °C. The total hydrogen content of these samples is in the region of 10 - 16 at. % as measured by SIMS. The microstructure parameter obtained from Raman data is less than 0.4 and H effusion experiments show no characteristic void-related low-temperature peak [69], in full compliance to experimental results of Beyer obtained on his standard PECVD *a*-Si:H samples, where the

low-temperature peak appeared only for samples deposited at substrate temperature ≤ 150 C [91]. The results of this work are confined to high-quality *a*-Si:H and the discussion will be limited to such material as well. The investigation of the successive crystallization of *a*-Si:H containing large amounts of interconnected voids will be subject of future studies.

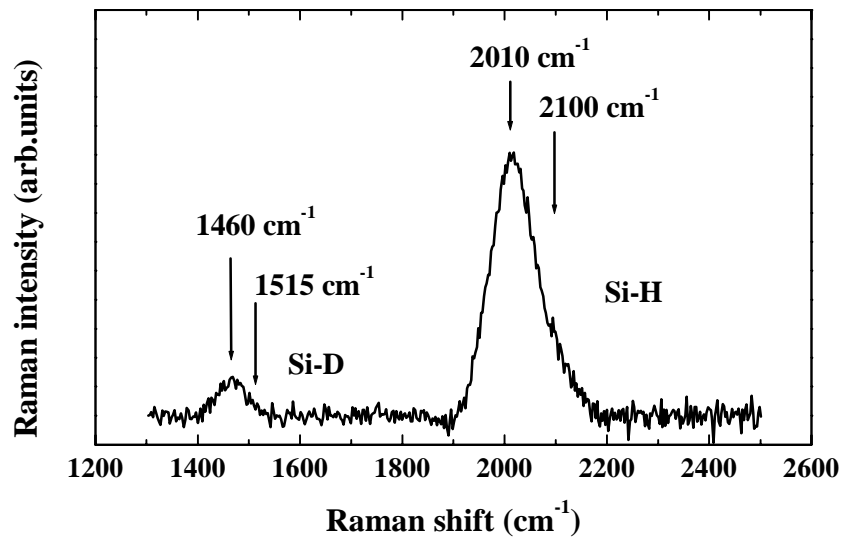


Fig. 6.1: Hydrogen modes of *a*-Si:H:D. Hydrogen modes around 2000 cm^{-1} (Si-H) and 2100 cm^{-1} and corresponding D modes at 1460 cm^{-1} (Si-D) and 1510 cm^{-1} are found. No modes are found in the region $1600 - 1800\text{ cm}^{-1}$ which should arise if the sample contains Si-HD. This vitiates the thesis that the mode at 2100 cm^{-1} arises from Si-H₂ in case of these standard quality samples.

Beyer concedes that there are a number of *a*-Si:H samples that are compact according to H effusion experiments, i.e. containing no interconnected voids and thus no low-temperature H effusion peak, which have a value of R^* in the range of 0 - 0.7 according to IR measurements [91]. These samples do not show any dihydride bending modes. Beyer attributes the mode at 2100 cm^{-1} for these samples to H in isolated voids. A slightly more specific interpretation assumes that the mode at $\approx 2100\text{ cm}^{-1}$ is caused by platelet-like H clusters [96]. Restricting this hypotheses to high-quality compact *a*-Si:H, there are two experimental results that we obtained recently which support this interpretation.

In the first set of experiments Raman measurements were performed on deuterated amorphous silicon (*a*-Si:H:D). Fig. 6.1 presents the Raman backscattering data on

a-Si:H:D in the frequency range of 1300 - 2500 cm^{-1} . The Si-H and Si-D stretching modes are clearly resolved. The Si-D mode is asymmetric and deconvolutes to two Gaussian peaks centered at 1460 cm^{-1} and $\approx 1515 \text{ cm}^{-1}$. These peaks roughly correspond to the expected downshift by a factor of 1.38 [97, 98] of the H modes at 2010 cm^{-1} and 2100 cm^{-1} . This shift of 1.38 approximately agrees with the square root of the reduced mass ratio of 1.394 which is expected for Si-H relative to Si-D vibrations in a simple diatomic molecule. If the mode near 2100 cm^{-1} in Fig. 6.1 would originate from silicon dihydride (Si-H_2) the spectrum should also reveal a stretching vibration for Si-HD around 1715 cm^{-1} . Since this mode is not observed it can be concluded that the mode near 2100 cm^{-1} is not due to Si-H_2 . Similar experiments have been performed for $\mu\text{c-Si:H:D}$ and poly-Si:H:D. The lack of a vibrational mode between 1500 cm^{-1} and 2000 cm^{-1} in all of these samples indicates that the observed modes around 2100 cm^{-1} ($\approx 2110 \text{ cm}^{-1}$ for poly-Si:H and $\approx 2130 \text{ cm}^{-1}$ for $\mu\text{c-Si:H}$) are not related to silicon dihydride [99].

The second set of experiments supporting the assignment of the mode at 2100 cm^{-1} to clustered hydrogen are Raman backscattering measurements performed on heavily P and B doped *a*-Si:H. The influence of doping on the H-bonding configurations is shown in Fig. 6.2, where Raman backscattering data in the range of 1800 - 2200 cm^{-1} are presented for undoped and heavily P and B doped *a*-Si:H. In case of the undoped *a*-Si:H sample the parameter R^* being an indicator for the ratio of the modes at 2000 cm^{-1} and 2100 cm^{-1} (defined in equation (5.4) in section 5.1) amounts to about 0.15. For a nominal gas phase doping of 1 % PH_3 R^* increases to a approximately 0.3. On the other hand, in the case of high diborane concentrations there is only a mode at 2000 cm^{-1} and $R^* = 0$.¹ A similar observation was reported by Gleason *et al.* who performed IR spectroscopy and nuclear magnetic resonance (NMR) measurements on doped and undoped *a*-Si:H [102]. The influence of doping on the hydrogen bonding configurations in *a*-Si:H is reminiscent of the Fermi energy dependence of hydrogen platelet formation in *c*-Si. Nickel *et al.* show in a detailed analysis, that the hydrogen platelet formation in

¹ All samples were deposited with similar H dilution of silane only with different levels of doping. All other deposition parameters were identical and correspond to deposition conditions which lead to high quality *a*-Si:H. This point is important as several investigations show that the value for R^* in *a*-Si:H depends critically on the deposition conditions such as H dilution [87, 100, 101].

c-Si depends on the Fermi energy [103]. Platelet formation is only observed for Fermi energies of $E_C - E_F \leq 0.3$ eV. Moreover, the platelet concentration increases monotonically as E_F moves closer to the conduction band [103].

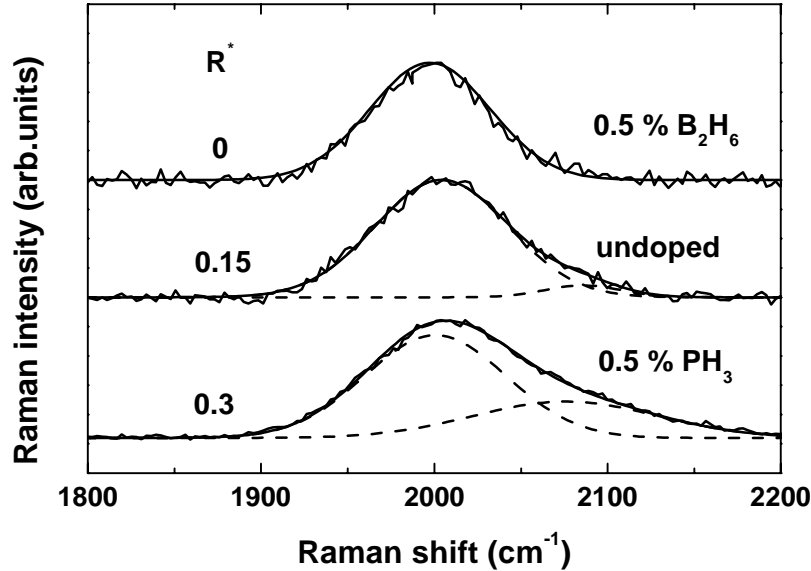


Fig. 6.2: Influence of doping on hydrogen bonding of *a*-Si:H. In case of heavy boron doping the mode at 2100 cm^{-1} decreases, while in case of heavy phosphorous doping the mode increases with respect to the undoped sample deposited under identical conditions.

A possible microscopic configuration for the clustered hydrogen atoms are H_2^* complexes [96]. A model based on the idea that the formation of these H complexes requires charge neutrality explains the observed Fermi energy dependence of the platelets [103]. The doping level dependence of the hydrogen bonding configurations shown in Fig. 6.2 suggests that for amorphous silicon a similar Fermi energy dependent platelet-like cluster formation mechanism is at work like in polycrystalline and crystalline silicon [99]. Poly-Si and c-Si containing platelets show local vibrational modes at around 2130 cm^{-1} [99, 104]. These observations support the assignment of the mode at 2100 cm^{-1} to clustered hydrogen and suggest that this clustered hydrogen is consistent with hydrogen stabilized platelets observed in crystalline and polycrystalline silicon.

Jackson *et al.* postulate that whenever the H concentration in any form of Si (c-Si, poly-Si, or *a*-Si) is high ($c_H > 4 \times 10^{20}\text{ cm}^{-3}$) a considerable amount of H resides in

platelet-like clusters [105]. The microscopic model for these H clusters in c-Si and poly-Si is the so-called $(H_2^*)_n$ complex. $(H_2^*)_n$ is an aggregation of H_2^* complexes. A H_2^* complex (Fig. 6.3) is formed in a two-step process. In the first step one H atom is placed in a bond centered side (BC). The H(BC) breaks the Si-Si bond and forms an Si-H bond. In the following step the unbonded Si atom moves towards its back bonded neighbors yielding an almost planar sp^2 bonding configuration with its silicon backbond neighbors, and the remaining p_z orbital bonds with the H in the T_D site [106]. Hence, two relatively strong Si-H bonds are formed.

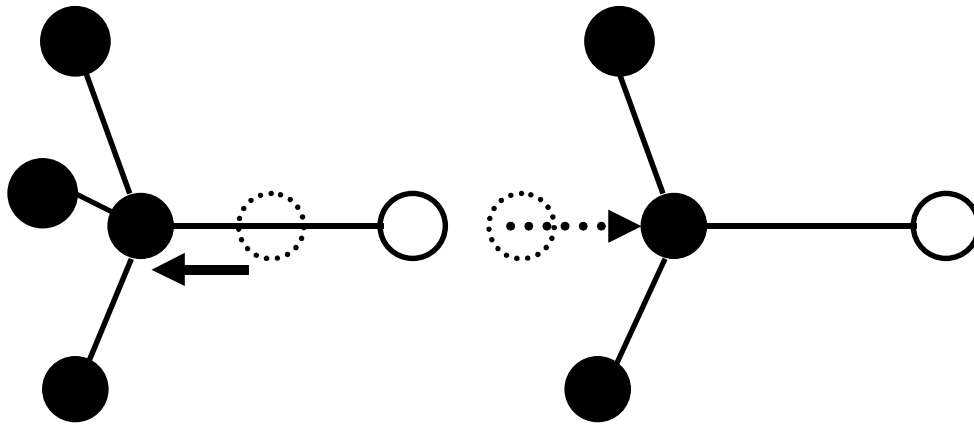


Fig. 6.3: The H_2^* -complex [106]. Solid spheres are Si atoms and open spheres are H atoms. The dashed circles indicate the positions of the Si atom prior to H insertion.

Taking all the other experimental evidence and the existing models on H platelet formation in silicon together the following picture can be drawn to explain the observed enhanced dissociation of the Si-H during the successive laser crystallization procedure. The vibrational mode at 2100 cm^{-1} in the case of high-quality $a\text{-Si:H}$ without extended void structures is attributed to clustered hydrogen, which has a microstructure similar to the $(H_2^*)_n$ complex. According to the cluster nucleation and growth model, in the $(H_2^*)_n$ complex the average binding energy per H atom depends on the number of H pairs in the cluster due to the perimeter strain energy [96, 105]. With an increasing number of H pairs in a cluster the average H binding energy increases [105]. A variation of cluster sizes results in a distribution of binding energies in the range of 2 - 3 eV [96]. A variation of the cluster size is a reasonable assumption for both the amorphous and the partially crystallized films. On the other hand, the binding energy of H at an isolated silicon dangling bond is 2.17 eV according to theoretical results based on local-density

pseudopotential calculations [107]. In consequence, the binding energy of most of the clustered hydrogen will be larger than the binding energy of Si-H.

With this model the enhanced dissociation of the Si-H in the course of the successive crystallization can be explained. The successive crystallization leads to a dehydrogenation of the samples. The difference in the binding energies of Si-H and H accommodated in clusters of varying size explains why the ratio of the modes at 2000 cm^{-1} and 2100 cm^{-1} changes in the course of the successive crystallization, as the more weakly bonded Si-H is removed more easily [67].

6.2 Structure of laser crystallized poly-Si

Grain boundary types

According to the EBSD analysis the grain boundaries of undoped films crystallized in the SLG regime are essentially twin boundaries of first and second order. A small contribution of higher order twin boundaries exists, some of which may contain a superimposed network of secondary dislocations. Generally, the grains have a low intra-grain dislocation density of less than $8 \times 10^6 \text{ cm}^{-2}$.

The solidification of silicon is known to produce stacking faults and twin boundaries. These planar defects have a rather low interfacial energy [108-110] and form to accommodate very small incompatibilities that arise at the solidification front. This can explain the dominance of first and second order twin boundaries in laser crystallized poly-Si. Higher order twin boundaries form by reaction between lower order ones. Obviously, small deviations from the exact coincidence orientation can be adapted by secondary dislocation networks attached to the coincidence grain boundaries. As the interfacial energy of higher order twin boundaries is comparably high the attachment of secondary dislocations presents only a relatively small change in energy. Therefore, this process is more likely to occur than the attachment of secondary dislocations to first order twins possessing a low interfacial energy that would result in a much greater change of energy. This conclusion is consistent with the fact that secondary dislocations are mainly observed at higher order twin boundaries in case of the samples investigated in this work. Similar observations are reported for edge defined film-fed grown Si ribbons [111]. It is even possible that these boundaries sweep the grain interiors free of dislocations, because the secondary networks can assume low-energy configurations analogous to small angle grain boundaries. In any case, these superimposed dislocation networks make up only a few percent of the entire grain boundaries of the laser crystallized poly-Si films.

The CSL-distribution found in the films prepared in this work are not influenced by heavy doping. For heavily P and B doped poly-Si first and second order twin boundaries

are dominant. In fact, the dominance of first and second order twin boundaries was also found in TEM investigations for other laser crystallized samples produced by a variety of lasers, such as a copper vapor laser, excimer lasers operating with other wavelengths, and a frequency doubled Nd:YAG laser [112] using different crystallization procedures [16-18, 113]. From these results it was concluded that the predominant formation of first and second order twin boundaries is a general feature of laser crystallization [114]. On the other hand, previous reports by Im *et al.* suggest that grain boundaries created during excimer laser crystallization are essentially low angle grain boundaries [19, 23]. However, the conclusions drawn by these authors are based only on a few TEM micrographs and they did not employ EBSD analysis, which gives information on the grain boundary types with much more reliable statistics.

It is a well known fact that the nature of the grain boundaries in poly-Si strongly influences the electrical characteristics of the material. Reports in the literature show that coherent first order twins are electrically inactive [111, 115, 116]. Higher order twins and faceted twin boundaries, e.g. coherent first order twins with incoherent segments, are in most cases only weakly electrically active [117]. A secondary dislocation network leads to electronic levels in the band gap that can act as recombination centers [118]. Random grain boundaries are generally electrically active [117, 119]. From these results it can be concluded that the dominance of first and second order twin boundaries in laser crystallized poly-Si should be favorable regarding the electrical properties of the material. Clearly, more detailed investigations are necessary to proof this assumption.

Texture formation

A preferential orientation of the grains in laser crystallized poly-Si films was already observed by others [120, 121]. Loreti *et al.* confirmed a {111}-texture of excimer laser crystallized poly-Si films crystallized in the SLG regime by employing texture analysis in XRD [120]. However, in this work it is demonstrated that the presence of a texture sensibly depends on the experimental details of the laser crystallization process. From the assembled data it can be concluded that under the given experimental conditions (see section 5.2) a {111}-texture is obtained for all samples crystallized in the SLG regime. Samples crystallized with laser fluences too low to reach the SLG regime exhibit

random grain orientations. Moderate and heavy doping does not influence the texture formation. This is an important information since doping can strongly influence the texture formation in as-deposited micro- or polycrystalline thin films (e. g. see review by Kakinuma [122]).

For solid phase crystallization (SPC) of Si Haji *et al.* [119] showed that the texture formation depends on the ratio of the mean distance between nuclei H , and the film thickness d . For $H \gg d$ a $\{111\}$ -texture is obtained while for $H \ll d$ no preferential orientation develops [119]. This is shown schematically in Fig. 6.4.

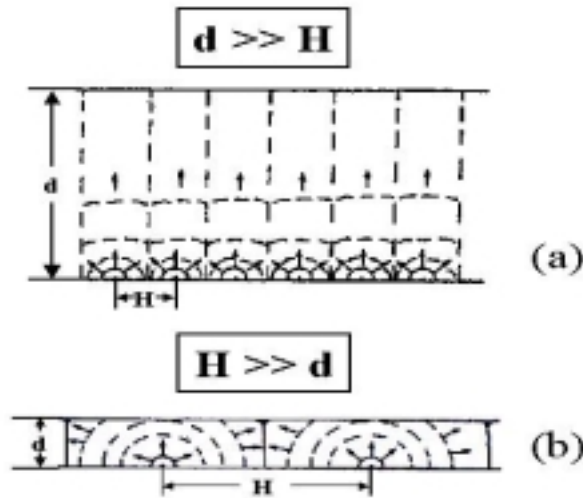


Fig. 6.4: Texture formation according to Haji *et al.* [119]. In case (a) with the film thickness d being larger than the mean distance between nuclei H no texture evolves, while situation (b) with H being larger than d leads to the formation of a $\{111\}$ -texture.

The basic assumption of the model are the different growth rates v_r perpendicular to the substrate of the low index planes in silicon, with $v_r\{111\} < v_r\{110\} < v_r\{100\}$ due to the difference of the surface free energies of these planes [123]. According to this model, a $\{111\}$ -texture is obtained for $H \gg d$ (Fig. 6.4 (b)) because the nuclei with an orientation that permits a fast growth rate parallel to the substrate (i.e. $\langle 111 \rangle$ grains) are extended laterally at the expense of the differently orientated nuclei. In case of $H \ll d$ (Fig. 6.4 (a)) no preferential orientation develops because the crystallites have the same chance to grow in any direction. In this work it was found that laser crystallized poly-Si

is {111}-textured if crystallized in the SLG regime, while no texture develops if the samples are not crystallized in the SLG regime. In fact, the situation is identical to the situations sketched in Fig. 6.4. In the SLG regime the grain growth occurs in the lateral direction (super *lateral* growth). In the partial melting regime as well as in the complete melting regime the grain growth is to a large extent perpendicular to the surface, starting from a high density of nucleation centers either from unmolten silicon (partial melting regime) or from homogenous nucleation in the supercooled melt (complete melting regime)(see review by Im. *et al.* [19]). Thus, the conditions of the SLG regime correspond to the situation $H \gg d$ and consequently a {111}-texture develops. The very idea of the super lateral growth model is that the nucleation starts from unmolten silicon islands, which occur at a distance H that is several times larger than the film thickness [23]. On the other hand, for the poly-Si crystallized with laser fluences outside the SLG regime the situation corresponds to $H < d$ and thus, no texture develops. It seems, that the model of the texture formation for SPC developed by Haji *et al.* can be applied to excimer laser crystallization even though the experimental conditions are completely different.

The question of what kind of texture laser crystallized poly-Si samples possess is important for device fabrication. Si homoepitaxy depends on the texture of the Si-substrate ([27] and references therein). Platen *et al.* show that the dependence of the critical thickness d_{epi} up to which a low temperature (325 °C) ECR-CVD Si-homoepitaxy is possible follows the sequence $d_{epi}(100) > d_{epi}(311) > d_{epi}(111) > d_{epi}(110)$, with $d_{epi}(100) > 1.6 \mu\text{m}$, $d_{epi}(111) \approx 35 \text{ nm}$ and $d_{epi}(110) \approx 0 \text{ nm}$ [27]. With increasing deposition temperature d_{epi} increases for all substrate orientations except for epitaxy on (110) for which epitaxy has not been achieved so far. Thus, to use laser crystallized poly-Si as seed layers for Si homoepitaxy at low temperatures the films should exhibit a {100}-texture. On the other hand, the {111}-texture does not exclude subsequent epitaxy. Si homoepitaxy on (111) wafers can be achieved by employing ion assisted deposition (IAD) at temperatures of about 700 - 800 °C [124]. Since these temperatures are well below the softening point of quartz, homoepitaxy experiments could be performed on poly-Si samples described in this work.

Almost any texture can be achieved for vapor-grown poly-Si depending on the experimental parameters and the deposition method used [122]. Therefore, there is proba-

bly a fair chance that in the case of laser crystallization a set of parameters can be found where the crystallized films exhibit a {100}-preferential orientation.

In conclusion, the model of Haji *et al.* explaining the texture formation in poly-Si prepared by SPC can account for the {111}-texture of poly-Si crystallized in the SLG regime. It can also explain why no texture develops for poly-Si samples with smaller grains crystallized with laser fluences outside the SLG regime. The {111}-texture of the laser crystallized poly-Si is not optimal for a subsequent low-temperature Si homoepitaxy.

6.3 Raman spectra of heavily doped poly-Si: Fano effect revisited

Fano effect in c-Si and poly-Si

The characteristic change of the Lorentzian line shape of the phonon peaks in the spectra of heavily doped poly-Si can be explained by the Fano effect. The Fano effect is a general effect arising from the coherent interference of a discrete and a continuous excitation. Fano first proposed this mechanism to explain asymmetries in atomic absorption spectra [31]. In Raman scattering experiments the Fano effect arises if a coherent interaction V exists between a discrete scattering source (such as a phonon) and a continuous scattering source (such as electrons). The coherent interaction leads to destructive and constructive interference, which will influence the line shape of the spectra. This results in a Fano line shape [31]

$$F(q, \varepsilon) = \frac{(q + \varepsilon)^2}{1 + \varepsilon^2}. \quad (6.1)$$

In this equation the Fano parameter q defines the strength of the asymmetry of the line shape and the parameter ε determines the position and strength of the line. In the case of Raman spectra the sign of q determines, on which energy side the light-scattering rate is enhanced and on which it is reduced. For negative q the light-scattering is enhanced on the low-energy side and reduced on the high-energy side, while for a positive q the reverse is true.

Cardeira *et al.* were the first to explain asymmetric broadenings of the LO-TO phonon line of heavily boron doped c-Si on the basis of the Fano effect [29]. The authors applied the Fano formalism to an approximately flat, energy-independent electronic continuum background interfering with a discrete phonon state, thus giving a theoretical foundation for the interpretation of Fano broadening in heavily doped c-Si. The key idea of this explanation is, that a (quasi-)continuum of Raman active electronic excitations is produced by inter-valence band transitions, whose energy overlaps with that of the

LO-TO phonon.¹ The coherent interaction between the two scattering mechanisms, the electronic Raman scattering (continuous) and the one-phonon Raman scattering (discrete) leads to Fano line shapes as described generally by equation (6.1). In case of Raman scattering in silicon the precondition for the occurrence of the Fano effect is a high concentration of free carriers that shift the Fermi energy into the conduction or valence band. Fig. 6.5 shows the band structure for heavily B doped c-Si according to Ref. [125]. The Fermi energy E_F is indicated in the figure. ω_m is the low-energy cutoff of the inter-valence-band continuum. Owing to the anisotropy of the valence band, the continuum extends from ω_m to very high energies due to the flatness of the heavy hole band in certain direction in \mathbf{k} space. Since in Si the spin-orbit splitting Δ_0 is 44 meV, the continuum overlaps in energy with the LO-TO phonon for almost any value of carrier concentration.

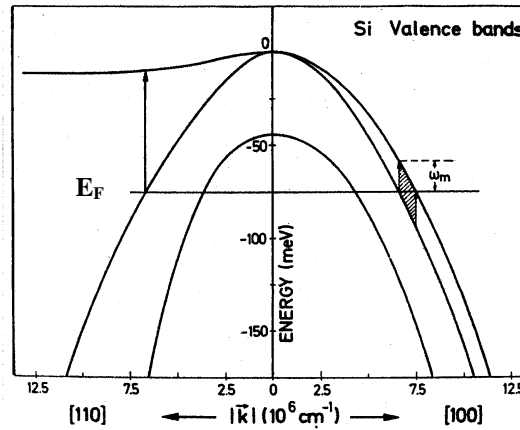


Fig. 6.5: Band structure of p-Si according to Ref. [125]. The vertical arrows indicate inter-valence-band transitions of the electronic continuum. The shaded region between the arrows corresponds to the total number of transitions for a given direction in \mathbf{k} space. E_F is the Fermi energy and ω_m the low-energy cutoff of the inter-valence-band continuum.

Following the explanation of asymmetric broadenings in the spectra of heavily B doped c-Si similar phenomena were discovered for heavily doped n-type silicon as well [30, 126]. The Fano broadening is weaker in n-type c-Si and of opposite sign. Thus, the asymmetric broadening occurs on the low energy side of the LO-TO phonon. A detailed experimental and theoretical investigation of the Fano effect in Raman scattering measurements of n-type Si can be found in Ref. [30]. Similar to the case of p-type c-Si, the

¹ The energy of LO-TO phonon in Si is approximately 65 meV.

principal idea is, that a continuum of Raman allowed electronic transitions exists between the Δ_1 and Δ_2 conduction bands (inter-conduction band transitions). The energy range of these transitions overlaps with the energy of the discrete optical phonon state. Hence, coherent interference between the discrete and continuum can take place.

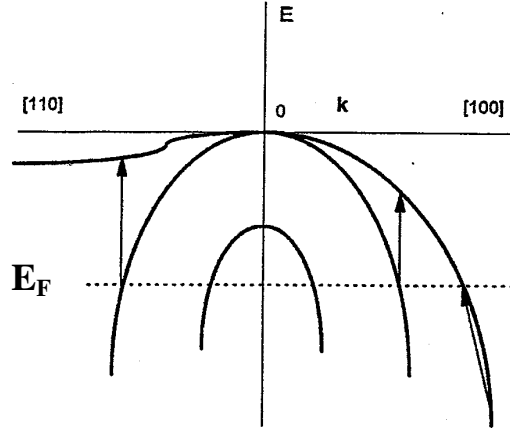


Fig. 6.6: Difference between *intraband* (oblique arrow) and *interband* transitions (vertical arrows).

In the discussion of Raman scattering on heavily doped Si it is important to clearly distinguish between *interband* and *intraband* transitions. *Interband* transitions in this context describe either inter-valence- or inter-conduction-band transitions. A graphical reference for the two types of transitions is given in Fig. 6.6 for p-type silicon. The *interband* transitions give rise to the Fano line shapes in the Raman spectra. Raman active *intraband* transitions can give rise to a broad low-frequency tail ($\omega < 200 \text{ cm}^{-1}$) for *polarized* Raman laser excitation in case of n- [127] and p-type silicon [128].

In the following paragraph all relevant equations for the case under study will be given. The theoretical derivations can be found in Refs. [29, 31, 129]. The Raman cross section $\alpha(\omega)$ is given by

$$\alpha(\omega) = \alpha_0 \frac{(q + \varepsilon(\omega))^2}{1 + \varepsilon(\omega)^2}, \quad (6.2)$$

where α_0 is a prefactor. The Fano parameter q is defined as

$$q = T_p / \pi \rho V T_e. \quad (6.3)$$

T_p and T_e are the phonon transition-matrix element and the constant transition-matrix element of the electronic continuum, respectively. ρ is the density of electronic excitations (per unit energy) and is assumed to be constant, while V denotes the coherent interaction between the two scattering sources. The parameter ε as a function of ω is given by

$$\varepsilon(\omega) = (\omega - \omega_p) / \Gamma, \quad (6.4)$$

where ω_p is the bare phonon frequency, and Γ is the linewidth contribution to the total linewidth (Γ is the HWHM of the limiting Lorentzian for $q^{-1} \approx 0$). Fig. 6.7 and Fig. 6.8 show a number of curves calculated from equation (6.1).

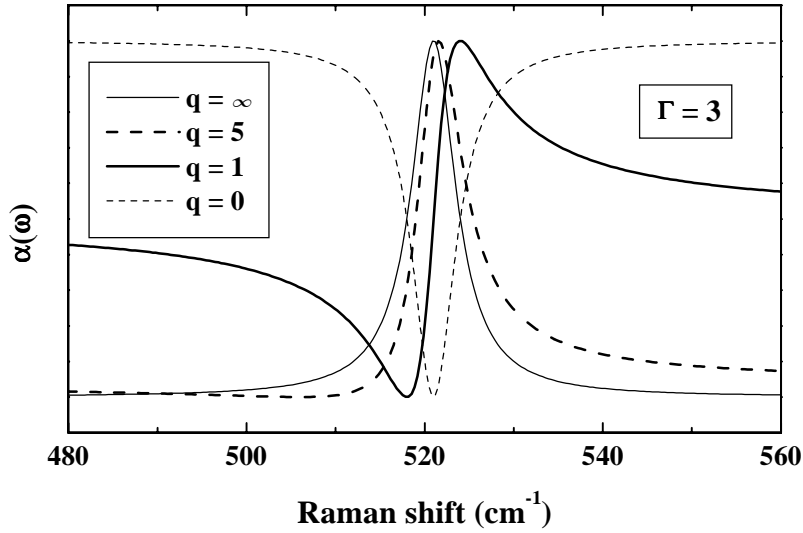


Fig. 6.7: Fano curves calculated with different values of q using equation (6.2).

In both figures a value of $\omega_p = 521 \text{ cm}^{-1}$ was used for the bare phonon frequency. In case of Fig. 6.7 q was varied and Γ was kept constant at $\Gamma = 3$. In the limiting case $q^{-1} \rightarrow 0$ a Lorentzian line shape is recovered. This case corresponds to $\rho VT_e \rightarrow 0$, i.e. if ρT_e is not vanishing this means that there is no coherent interaction ($V \rightarrow 0$). For decreasing q the asymmetry of the phonon line shape becomes more apparent. In the special case $|q| = 1$ the asymmetry of the line shape is maximized with respect to ω_p . The analytic expressions for the extrema are

$$\begin{aligned}\omega_{\max} &= \omega_p + \Gamma/q, \\ \omega_{\min} &= \omega_p - \Gamma/q.\end{aligned}\tag{6.5}$$

The zero crossing of the Fano line shape occurs at

$$\omega = \omega_p + \Gamma(1 - q^2)/2q.\tag{6.6}$$

A useful method for the geometric extraction of ω_p from the Fano line shape was given by Piao *et al.*, who noted that a line connecting the maximum and minimum crosses the Fano curve at ω_p [130]. If q changes sign the curves are reflected at ω_p .

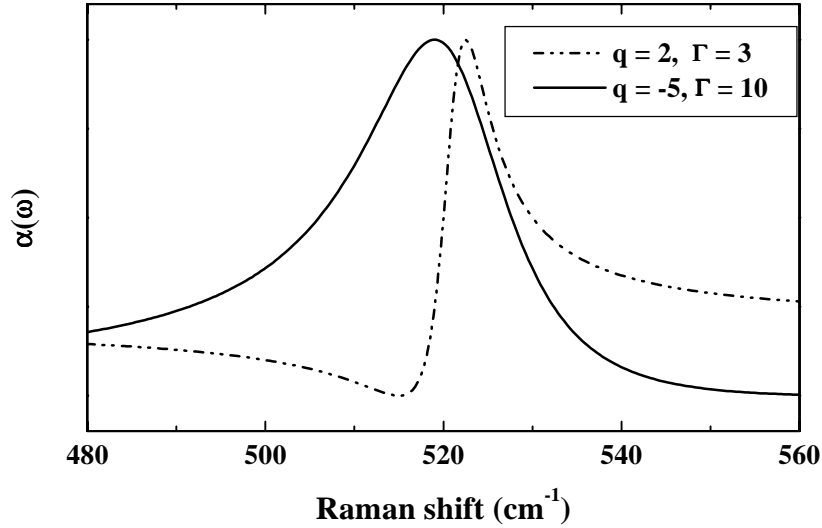


Fig. 6.8: Fano curves calculated using equation (6.2) with q 's of opposite sign and different Γ 's.

In Fig. 6.8 a curve with a negative q and a larger value of Γ is shown. A very important point concerning the Fano effect in silicon is the fact that the Fano parameter q has the opposite sign for p- and n-type silicon. It is positive for p- and negative for n-type silicon. A theoretical explanation for the sign of q was given by Chandraskhar *et al.* [30]. In this paper the signs of T_e and V were derived to be negative for the case of n-type Si. Since the sign of T_p is negative as well [131] this leads to a negative sign of q for n-type Si according to equation (6.3).

Cerdeira *et al.* [29] found by numerical fits to their data on heavily boron doped c-Si that the Fano parameter $q \sim |T_p/T_e|$ scales with the laser frequency ω_L

$$q \propto (\omega' - \omega_L)^{-1}, \quad (6.7)$$

where ω' is a critical point in the band structure of Si ($\omega' = 3.3$ eV). The critical point is the E'_0 transition at and in the neighborhood of the Brillouin zone center. The influence of two different Raman excitation wavelength λ_1 and λ_2 ($\lambda_1 < \lambda_2$) is described by the ratio β ,

$$\beta = q(\lambda_1) / q(\lambda_2). \quad (6.8)$$

Theoretically, the value of β was predicted to be $\beta \approx 1.83$ independent of the free carrier concentration for $\lambda_1 = 488$ nm and $\lambda_2 = 647.1$ nm. Experimentally, Cerdeira *et al.* found values for β in the range from 1.5 to 2.3 for free hole concentrations ranging from $6 \times 10^{18} \text{ cm}^{-3}$ to $1.6 \times 10^{20} \text{ cm}^{-3}$ with no systematic dependence on the carrier concentration [29].

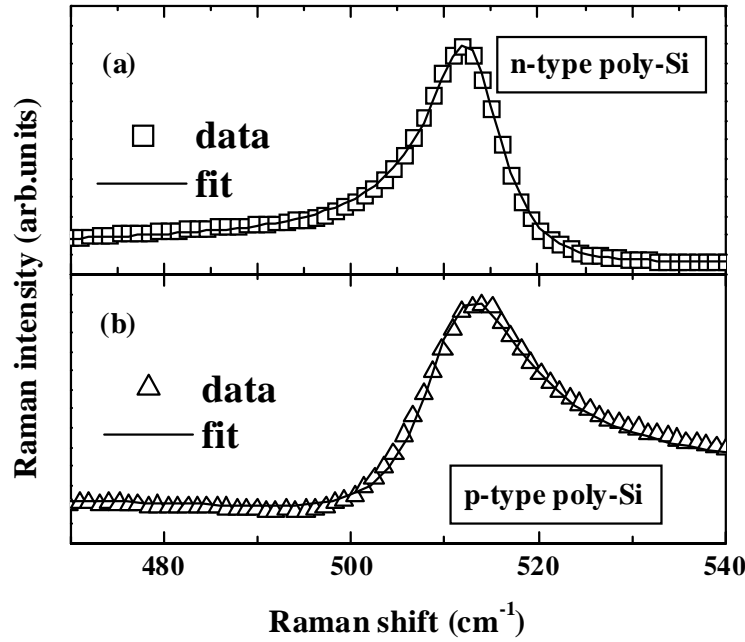


Fig. 6.9: Raman spectra of heavily doped poly-Si. The data were fitted using equation (6.2).

With this theoretical and experimental background all the results of section 5.3.3 for Raman measurements on heavily n- and p-type laser crystallized poly-Si can be explained [86]. For samples with a free carrier concentration of more than 10^{19} cm^{-3} the Fano broadening of the LO-TO phonon line is observed. The sign of the Fano parameter

q is negative for n- and positive for p-type poly-Si thin films which is consistent with results reported on c-Si. The dependence of q on the free carrier concentration is also similar to c-Si, i.e. the asymmetry becomes more pronounced as the concentration of free carriers increases. Using equation (6.2) numerical least squares fits can be performed on the experimental Raman data. The obtained fits are excellent (Fig. 6.9). From the fits the quantities q , Γ , ω_p are obtained and summarized in Table 6.1.

Table 6.1: Fano parameter for various P and B doped samples.

carrier type	n/p (cm ⁻³)	q	ω_p (cm ⁻¹)	Γ
n	5.2×10^{19}	-19	516	2.5
n	3.8×10^{20}	-8.7	516	3.2
n	1.7×10^{21}	-4.6	513	5.3
p	8.6×10^{19}	19	514	5.3
p	3.3×10^{20}	2.3	510.5	5.7
p	6.0×10^{20}	2.0	508	6

It should be noted that the bare phonon frequencies ω_p obtained from the fits of the Raman data are not identical to the apparent positions of the LO-TO phonon line shown in Fig. 5.35. The high concentration of the doping atoms in the poly-Si samples causes an additional shift of the bare phonon frequency to lower wave numbers. Finally, the Raman spectra of heavily doped laser crystallized poly-Si show the dependence on the excitation wavelength of the Raman laser, characteristic for the Fano effect in case of c-Si, as can be seen in Fig. 5.37 in section 5.3.3. The value of β in this case ($\beta = q(458 \text{ nm})/q(633 \text{ nm})$) amounted to approximately 2.8.

The appearance of the Fano effect and its strength does not depend on the grain size of the poly-Si investigated in this work ($\langle x \rangle = 0.1 - 5 \mu\text{m}$). It is reasonable to assume, that for poly-Si with grain sizes exceeding $5 \mu\text{m}$ the same will apply. However, the question remains whether the Fano effect can be observed in Raman measurements of heavily

doped microcrystalline silicon as well, where the grain size is smaller than 50 nm. This problem will be discussed in the following section.

Fano effect in $\mu\text{c-Si}$?

As already shown in section 5.3.3 the Raman spectra of heavily doped $\mu\text{c-Si:H}$ samples do not show the same behavior as the spectra of heavily doped poly-Si samples. Still, it is worth to take a closer look at the results in order to elucidate, whether Fano broadenings can be observed in $\mu\text{c-Si:H}$. For clarity this problem will be discussed separately for P and B doped $\mu\text{c-Si:H}$ samples.

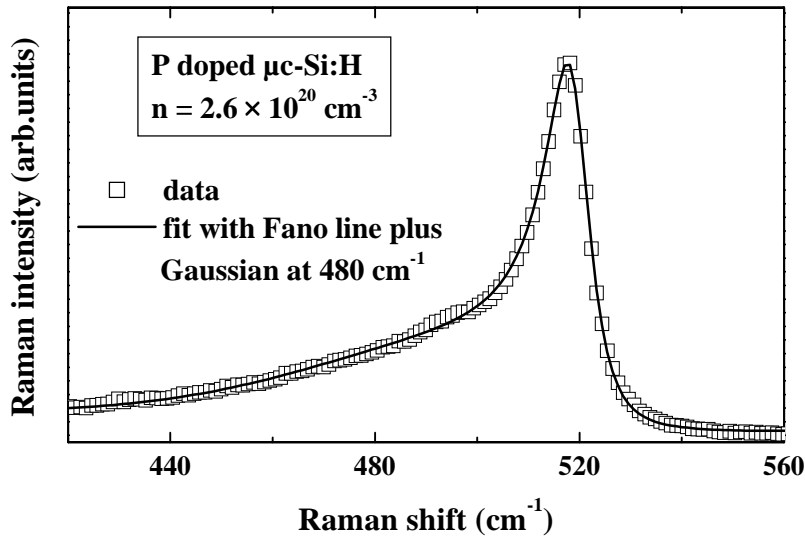


Fig. 6.10: Raman spectrum of P doped $\mu\text{c-Si:H}$ fitted with a Fano line plus a Gaussian centered at 480 cm^{-1} .

In Fig. 5.38 of section 5.3.3 the Raman spectrum of a heavily P doped $\mu\text{c-Si:H}$ sample is shown. According to Hall effect measurements the free electron concentration of this sample amounts to $2.6 \times 10^{20}\text{ cm}^{-3}$. The free electron concentration is independent of temperature in the range of 20 – 300 K which is indicative of a degenerate semiconductor with the Fermi energy residing in the conduction band [132]. Furthermore, detailed electron spin resonance (ESR) measurements performed on heavily P doped $\mu\text{c-Si:H}$ with electron concentrations ranging from $2 \times 10^{19}\text{ cm}^{-3}$ to $2 \times 10^{20}\text{ cm}^{-3}$ show that the temperature dependence of the susceptibility can only be explained by taking

into account two contributions, one resulting from Curie paramagnetism and the other resulting from Pauli magnetism. The Pauli magnetism contribution is attributed to a degenerate electron gas [133]. Therefore, the experimental evidence suggests, that the precondition for the occurrence of the Fano effect in the Raman spectra of heavily P doped $\mu\text{c-Si:H}$ samples is met. However, is a Fano broadening really observed in Fig. 5.38? The unsatisfactory answer to this question is „maybe“!

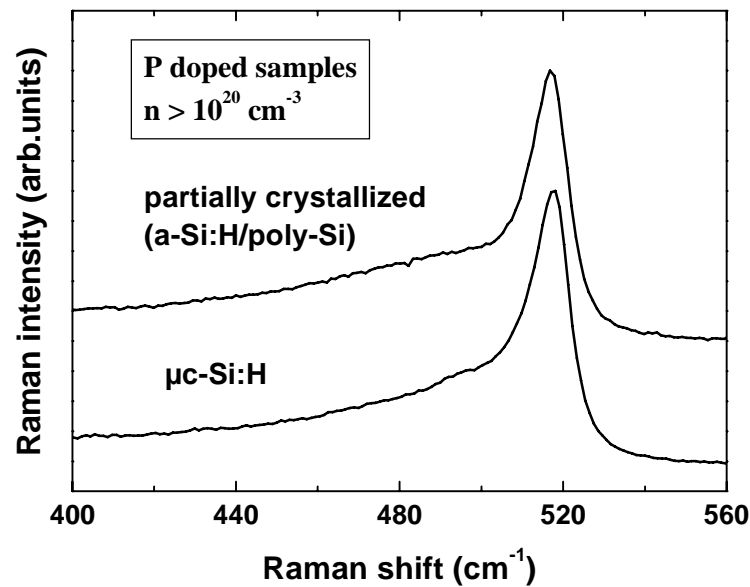


Fig. 6.11: Raman spectra of partially crystallized P doped $a\text{-Si:H}$ and as-deposited P doped $\mu\text{c-Si:H}$. There are no unique features of the two curves, which would make a clear distinction between the spectra possible.

Fig. 6.10 shows that the background corrected Raman spectrum of heavily P doped $\mu\text{c-Si:H}$ can be fitted perfectly with a Gaussian contribution at 480 cm^{-1} and a Fano broadened line at $\approx 519\text{ cm}^{-1}$. Since the TO phonon line of $a\text{-Si:H}$ at 480 cm^{-1} is rather broad ($\text{FWHM} \approx 60\text{ cm}^{-1}$) the distinct features of the Fano line shape in the case of a negative q and $\omega_p \approx 521\text{ cm}^{-1}$ are blurred.¹ In Fig. 6.11 the Raman spectra of a partially crystallized heavily P doped $a\text{-Si:H}$ sample and an as-deposited heavily P doped $\mu\text{c-Si:H}$ sample are shown. There are no unique features in the two spectra which allow

¹ To further complicate the picture it is possible to perform a similar fit on Raman spectra of *undoped* $\mu\text{c-Si:H}$. Again, the background corrected spectrum can be fitted fairly correctly using a Fano line shape with a negative q and an additional Gaussian centered at 480 cm^{-1} .

a clear distinction.¹ In consequence, although there are strong experimental hints from Hall and EPR measurements that in P doped $\mu\text{c-Si:H}$ the precondition for the occurrence of the Fano effect is met, it is not possible from the existing experimental data, to provide clear evidence either for or against the occurrence of Fano broadening in the Raman spectra of heavily P doped $\mu\text{c-Si:H}$ samples.

In case of heavily boron doped $\mu\text{c-Si:H}$ the picture is different. The Raman spectrum of an as-deposited B doped $\mu\text{c-Si:H}$ sample (Fig. 5.39 in section 5.3.3) does not show the Fano broadening one would expect from a degenerately doped p-type silicon film. However, Hall effect measurements performed on this sample indicate that the free hole concentration amounts to $1 \times 10^{20} \text{ cm}^{-3}$. Moreover, the free hole concentration is independent of temperature indicating again, that the sample is degenerate. The lack of a Fano broadening with a positive q in the Raman spectra of as-deposited B doped $\mu\text{c-Si:H}$ is evident from Fig. 6.12. In this figure the background corrected Raman spectrum of an as-deposited B doped $\mu\text{c-Si:H}$ sample and a calculated curve of the superposition of a Fano line with a positive q and a Gaussian are shown. The parameters of the Fano broadening were obtained from the fit of the Raman spectrum of the crystallized sample (curve (b) in Fig. 5.39). The Gaussian contribution was adjusted so that it roughly has the same intensity ratio (I_{486}/I_{515}) as in the case of the Raman spectrum of the as-deposited B doped $\mu\text{c-Si:H}$ sample (curve (a) in Fig. 5.39). Although the calculated curve contains some uncertainties the main message is reliable. The features of the Raman spectrum of the as-deposited highly B doped $\mu\text{c-Si:H}$ sample clearly do not resemble a superposition of a Gaussian contribution and a Fano line with a positive q . This can also be seen by comparing the spectra of as-deposited B doped $\mu\text{c-Si:H}$ and partially crystallized B doped $a\text{-Si:H}$ (Fig. 5.32 in section 5.3.3). On the contrary, the Raman spectra of highly B doped $\mu\text{c-Si:H}$ do show significant similarities to the spectra of undoped and highly P doped $\mu\text{c-Si:H}$. Especially, one observes the typical low-

¹ The only significant difference results from the position of the LO-TO peak, which is shifted in case of the partially crystallized film to lower wavenumbers. However, this feature alone can not be taken as an indication for the presence of the Fano effect.

energy broadening of the crystalline LO-TO peak, reminiscent of a Fano broadening with a negative q .¹

A possible explanation of the behavior of the highly B doped $\mu\text{c-Si:H}$ samples is at the moment mere speculation. Most certainly, the answer to this problem lies in the specific structural properties of $\mu\text{c-Si:H}$, especially the small grain size. The typical grain size of undoped $\mu\text{c-Si:H}$ amounts to less than 20 nm.

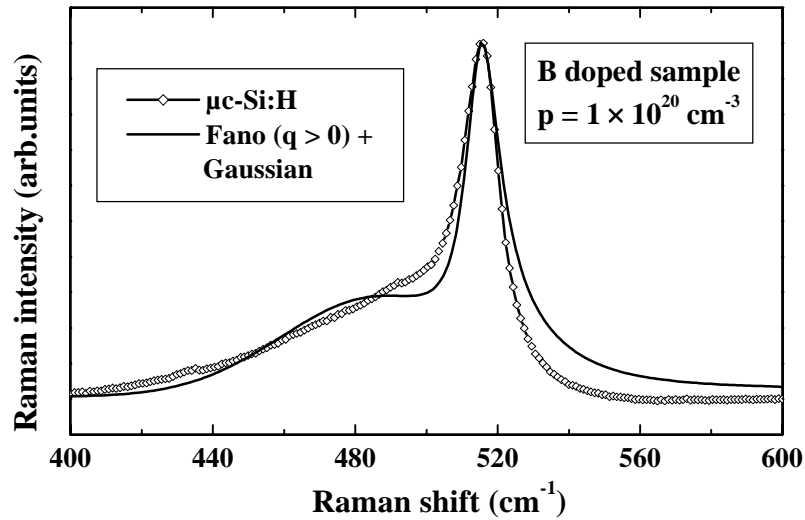


Fig. 6.12: Background corrected Raman spectrum of a B doped $\mu\text{c-Si:H}$ sample. For comparison a calculated curve of a Fano line ($q > 0$) with an additional Gaussian centered at 480 cm^{-1} is given as well (details are described in the text).

As the Hall effect measurements indicate that the highly P and P doped $\mu\text{c-Si:H}$ samples are degenerate the precondition for the occurrence of Fano broadening should be met. On the other hand, investigations on heavily B doped c-Si show that the application of stress diminishes the Fano broadening [29]. In the limit of high stress q^{-1} tends to 0, i.e. the Fano broadening is no longer observed. According to Cerdeira *et al.* the stress moves the continuum into energy regions where it no longer overlaps with the phonon energy [29]. The values for the uniaxial compressive stress, where the Fano broadening vanishes ($q^{-1} \approx 0$) amount to $\approx 1 - 2 \text{ GPa}$ in case of a free hole concentration of

¹ It should be noted that the investigation on heavily P and B doped $\mu\text{c-Si:H}$ are limited to films with a thickness smaller than 500 nm. Deposition of thicker films was not possible due to the extremely low deposition rates in case of the heavy doping.

$7 \times 10^{19} \text{ cm}^{-3}$ [29]. A considerable amount of intrinsic stress in the $\mu\text{c-Si:H}$ samples, possibly caused by the small grain size, could serve as an explanation for the lack of a Fano broadening with a positive q in the Raman spectra of highly B doped $\mu\text{c-Si:H}$. On the other hand, the non-occurrence of a Fano broadening with a positive q in B doped $\mu\text{c-Si:H}$ cannot be separated from the question of what actually causes the asymmetric broadening of the LO-TO phonon line in all the $\mu\text{c-Si:H}$ samples, regardless of their doping level and the free carrier type. As already mentioned this asymmetric broadening closely resembles a Fano broadening with a negative q .

To summarize this section the following two points shall be made. Firstly, the problem of the Fano effect in highly doped $\mu\text{c-Si:H}$ is not fully resolved regarding the experimental evidence and even more regarding the need for a consistent explanation of the Raman spectra of undoped and heavily doped $\mu\text{c-Si:H}$. However, the results presented in this work show the significance of the question and hopefully will stimulate further research in this field. Secondly, these findings add a new aspect to the problem of the distinction between microcrystalline and polycrystalline samples, which was indicated in section 4. As shown in the section 5.3.3 and discussed above heavily P and B doped thin poly-Si samples with a grain size $> 100 \text{ nm}$ show the Fano broadening of the LO-TO phonon line similar to c-Si with comparable doping levels. Hence, Raman spectra of heavily doped samples can be a criterion for the distinction between microcrystalline and polycrystalline silicon. Only material which shows a clear Fano broadening of the LO-TO phonon line with a negative q for heavy P doping and a positive q for heavy B doping can be regarded as polycrystalline silicon.

7 Summary

In this work the successive crystallization of undoped and doped amorphous silicon on glass substrates and the properties of the resulting films are investigated. The most important results are the following.

- In the course of successive crystallization a two-layer system is formed. At the surface a crystallized layer is created which extends into the film. The crystallinity of this top layer exhibits a strong depth dependence. Close to the substrate a residual amorphous layer remains.
- The successive crystallization is accompanied by a dehydrogenation of the samples. In the course of this dehydrogenation the dissociation of Si-H is enhanced compared to the dissociation of differently bonded hydrogen, which manifest itself in the mode at 2100 cm^{-1} . Fully crystallized samples can still contain a residual H concentration of up to 4 at. %.
- The enhanced dissociation of Si-H can be explained by the assumption that in the case of standard amorphous silicon the hydrogen mode at 2100 cm^{-1} is caused by platelet-like hydrogen clusters. In these clusters most of the hydrogen is more tightly bonded than Si-H.
- Undoped polycrystalline silicon (poly-Si) samples prepared by successive crystallization in the super lateral growth (SLG) regime have a grain size in the range of 3-4 μm and small roughness. Most grains possess a small dislocation density. The grains exhibit a $\{111\}$ -preferential orientation in the direction of the substrate normal. Poly-Si samples crystallized outside the SLG regime do not show a preferential orientation of the grains. The texture formation is explained using a model previously developed for solid phase crystallization. According to Raman measurements a considerable amount of stress is incorporated in all the laser crystallized films originating from the glass substrates.
- Doping has a significant influence on the crystallization process. Heavy P and B doping lead to a decrease and an increase of the two characteristic crystallization

parameters E_T and E_{SLG} , respectively. The influence of heavy doping on the two characteristic crystallization parameters is assumed to be mainly caused by a change of the thermal properties of the material.

- Heavily doped poly-Si samples crystallized in the SLG regime exhibit a {111}-texture of the grains similar to the undoped samples. The free carrier concentration in heavily doped films exceeds $5 \times 10^{20} \text{ cm}^{-3}$ for P and B doping.
- The high free carrier concentrations have a strong impact on the Raman spectra of the poly-Si, leading to asymmetric broadenings of the LO-TO phonon lines caused by the Fano effect.
- The Raman spectra of heavily B doped as-deposited $\mu\text{c-Si:H}$ films do not show the type of Fano broadening which occurs in heavily B doped c-Si and poly-Si.

8 References

- [1] S. D. Brotherton, J. R. Ayres, M. J. Edwards, C. A. Fisher, C. Glaister, J. P. Gowers, D. J. McCulloch, and M. Trainor, *Thin Solid Films* **337**, 188 (1999).
- [2] R. B. Bergmann, *Appl. Phys. A* **69**, 187 (1999).
- [3] R. A. Street, *Hydrogenated amorphous silicon*. (Cambridge University Press, Cambridge, 1991).
- [4] *Hydrogenated Amorphous Silicon I*, edited by J. D. Joannopoulos and G. Lucovsky (Springer, Berlin, 1984).
- [5] R. E. I. Schropp and M. Zeman, *Amorphous and Microcrystalline Silicon Solar Cells. Modeling, Materials and Device Technology*. (Kluwer, Dordrecht, 1998).
- [6] N. Yamauchi and R. Reif, *J. Appl. Phys.* **75**, 3235 (1994).
- [7] R. B. Bergmann, G. Oswald, M. Albrecht, and V. Gross, *Sol. Energy Mater. Sol. Cells* **46**, 147 (1997).
- [8] S. R. Herd, P. Chaudhari, and M. H. Brodsky, *J. Non-Cryst. Solids* **7**, 309 (1972).
- [9] O. Nast, Ph.D.-Thesis, Marburg, Germany (2000).
- [10] O. Nast and A. J. Hartmann, *J. Appl. Phys.* **88**, 716 (2000).
- [11] O. Nast and S. R. Wenham, *J. Appl. Phys.* **88**, 124 (2000).
- [12] S. D. Brotherton, *Semicond. Sci. Technol.* **10**, 721 (1995).
- [13] J. B. Boyce, P. Mei, R. T. Fulks, and J. Ho, *phys. stat. sol. (a)* **166**, 729 (1998).
- [14] *Laser Annealing of Semiconductors*, edited by J. M. Poate and J. W. Mayer (Academic Press, New York, 1982).
- [15] M. O. Thomson, G. J. Galvin, J. W. Mayer, P. S. Percy, J. M. Poate, D. C. Jacobson, A. G. Cullis, and N. G. Chew, *Phys. Rev. Lett.* **52**, 2360 (1984).
- [16] G. Andrä, J. Bergmann, F. Falk, and E. Ose, *Thin Solid Films* **318**, 42 (1998).

-
- [17] C. E. Nebel, S. Christiansen, H. P. Strunk, B. Dahlheimer, U. Karrer, and M. Stutzmann, *phys. stat. sol. (a)* **166**, 667 (1998).
- [18] J. R. Köhler, R. Dassow, R. B. Bergmann, J. Krinke, H. P. Strunk, and J. H. Werner, *Thin Solid Films* **337**, 129 (1999).
- [19] J. S. Im, M. A. Crowder, R. S. Sposili, J. P. Leonard, H. J. Kim, J. H. Yoon, V. V. Gupta, H. J. Song, and H. S. Cho, *phys. stat. sol. (a)* **166**, 603 (1998).
- [20] M. Matsumura, *phys. stat. sol. (a)* **166**, 715 (1998).
- [21] W. Staudt, S. Borneis, and K.-D. Pippert, *phys. stat. sol. (a)* **166**, 743 (1998).
- [22] J. S. Im, H. J. Kim, and M. O. Thomson, *Appl. Phys. Lett.* **63**, 1969 (1993).
- [23] J. S. Im and H. J. Kim, *Appl. Phys. Lett.* **64**, 2303 (1994).
- [24] *Hydrogen in Semiconductors II*, edited by N. H. Nickel (Academic Press, San Diego, 1999).
- [25] N. H. Nickel, N. M. Johnson, and W. B. Jackson, *Appl. Phys. Lett.* **62**, 3285 (1993).
- [26] P. Mei, J. B. Boyce, M. Hack, R. A. Lujan, R. I. Johnson, G. B. Anderson, D. K. Fork, and S. E. Ready, *Appl. Phys. Lett.* **64**, 1132 (1994).
- [27] J. Platen, B. Selle, I. Sieber, U. Zeimer, and W. Fuhs, *Mater. Res. Soc. Symp. Proc.* **570**, 91 (1999).
- [28] F. Cerdeira and M. Cardona, *Phys. Rev. B* **5**, 1440 (1972).
- [29] F. Cerdeira, T. A. Fjeldy, and M. Cardona, *Phys. Rev. B* **8**, 4734 (1973).
- [30] M. Chandrasekhar, J. B. Renucci, and M. Cardona, *Phys. Rev. B* **17**, 1623 (1978).
- [31] U. Fano, *Phys. Rev.* **124**, 1866 (1961).
- [32] P. Mei, J. B. Boyce, M. Hack, R. A. Lujan, D. L. Smith, S. E. Ready, D. K. Fork, G. B. Anderson, and R. I. Johnson, *Mater. Res. Soc. Symp. Proc.* **297**, 151 (1993).
- [33] P. Mei, J. B. Boyce, M. Hack, R. Lujan, S. E. Ready, D. K. Fork, R. I. Johnson, and G. B. Anderson, *J. Appl. Phys.* **76**, 3194 (1994).

-
- [34] S. R. Stiffler, M. O. Thompson, and P. S. Peercy, *Phys. Rev. Lett.* **60**, 2519 (1988).
- [35] D. Dutartre, *J. Appl. Phys.* **59**, 1977 (1986).
- [36] H. J. Song and J. S. Im, *Mater. Res. Soc. Symp. Proc.* **397**, 459 (1996).
- [37] G. B. Anderson, J. B. Boyce, D. K. Fork, R. I. Johnson, P. Mei, and S. E. Ready, *Mater. Res. Soc. Symp. Proc.* **343**, 709 (1994).
- [38] J. B. Boyce, G. B. Anderson, D. K. Fork, R. I. Johnson, P. Mei, and S. E. Ready, *Mater. Res. Soc. Symp. Proc.* **321**, 671 (1994).
- [39] S. R. I. Johnson, G. B. Anderson, J. B. Boyce, D. K. Fork, P. Mei, S. E. Ready, and S. Chen, *Mater. Res. Soc. Symp. Proc.* **297**, 533 (1993).
- [40] M. Hatano, S. Moon, M. Lee, K. Suzuki, and C. P. Grigoropoulos, *J. Appl. Phys.* **87**, 36 (2000).
- [41] T. Eiumchotchawalit and J. S. Im, *Mater. Res. Soc. Symp. Proc.* **321**, 725 (1994).
- [42] H. J. Kim and J. S. Im, *Mater. Res. Soc. Symp. Proc.* **321**, 665 (1994).
- [43] H. Kuriyama, K. Sano, S. Ishida, T. Nohda, Y. Aya, T. Kuwahara, S. Noguchi, S. Kiyama, S. Tsuda, and S. Nakano, *Mater. Res. Soc. Symp. Proc.* **297**, 657 (1993).
- [44] S. D. Brotherton, D. J. McCulloch, J. P. Gowers, J. R. Ayres, and M. J. Trainor, *J. Appl. Phys.* **82**, 4086 (1997).
- [45] W. Kern, *J. Electrochem. Soc.* **137**, 1887 (1990).
- [46] I. Kaiser, Ph.D.-Thesis, Marburg, Germany (1998).
- [47] M. J. Thomson, in *Hydrogenated Amorphous Silicon I*, edited by J. D. Joannopoulos and G. Lucovsky, (Springer, Berlin, 1984), p. 119.
- [48] F. Secco d'Aragona, *J. Electrochem. Soc.* **119**, 948 (1972).
- [49] R. Wiesendanger, *Scanning Probe Microscopy and Spectroscopy: Methods and Applications*. (Cambridge University Press, Cambridge, 1994).
- [50] B. E. Warren, *X-Ray Diffraction*. (Dover Publications, New York, 1990).

-
- [51] B. L. Adams, S. I. Wright, and K. Kunze, *Metallurgical Transactions A* **24A**, 819 (1993).
- [52] H. Düsterhöft, M. Riedel, and B.-K. Düsterhöft, *Einführung in die Sekundärionenmassenspektroskopie -SIMS-*. (Teubner, Leipzig, 1999).
- [53] C. Williams and D. Carter, *Transmission Electron Microscopy: A Textbook for Materials Sciences*. (Plenum Press, New York, 1996).
- [54] P. Blood and J. W. Orton, *The electrical characterisation of Semiconductors: Majority Carriers and Electron States*. (Academic Press, London, 1992).
- [55] M. Cardona and G. Güntherodt, *Light scattering in solids II, Basic Concepts and Instrumentation*. (Springer, Berlin, 1982).
- [56] I. de Wolf, *Semicond. Sci. Technol.* **11**, 139 (1996).
- [57] M. Birkholz, B. Selle, E. Conrad, K. Lips, and W. Fuhs, *J. Appl. Phys.* **88**, 4376 (2000).
- [58] I. Kaiser, N. H. Nickel, W. Fuhs, and W. Pilz, *Phys. Rev. B* **58**, R1718 (1998).
- [59] J. H. Zhou, K. Ikuta, T. Yasuda, T. Umeda, S. Yamasaki, and K. Tanaka, *Appl. Phys. Lett.* **71**, 1534 (1997).
- [60] P. Y. Yu and M. Cardona, *Fundamentals of Semiconductors*. (Springer, Berlin, 1996).
- [61] N. M. Johnson, D. K. Biegelson, and M. D. Moyer, *Appl. Phys. Lett.* **40**, 882 (1982).
- [62] T. I. Kamins and P. J. Marcoux, *IEEE Electron Devices Lett.* **EDL-1**, 159 (1980).
- [63] P. M. Smith, P. G. Carey, and T. W. Sigmon, *Appl. Phys. Lett.* **70**, 342 (1997).
- [64] A. T. Voutsas, M. K. Hatalis, J. Boyce, and A. Chiang, *J. Appl. Phys.* **78**, 6999 (1995).
- [65] P. Hapke, Ph.D.-Thesis, Aachen, Germany (1995).
- [66] S. D. Brotherton, D. J. McCulloch, J. B. Clegg, and J. P. Gowers, *IEEE Trans. Electron Devices* **40**, 407 (1993).

-
- [67] P. Lengsfeld, N. H. Nickel, and W. Fuhs, *Appl. Phys. Lett.* **76**, 1680 (2000).
- [68] P. Lengsfeld, N. H. Nickel, and W. Fuhs, *J. Non-Cryst. Solids* **266-269**, 659 (2000).
- [69] H. Heise, Personal communication.
- [70] N. H. Nickel, G. B. Anderson, and R. I. Johnson, *Phys. Rev. B* **56**, 12 065 (1997).
- [71] E. Anastassakis, *J. Appl. Phys.* **86**, 249 (1999).
- [72] Data sheet for Corning 7059 supplied by Corning Inc., Corning, NY, USA.
- [73] Data sheet for Suprasil 1 supplied by Hereaus Quarzglas, Hanau, Germany.
- [74] Data sheet for Corning 1737F supplied by Corning Inc., Corning, NY, USA.
- [75] *Semiconductors - Basic Data*, edited by O. Madelung (Springer, Berlin, 1996).
- [76] S. Wolf and R. N. Taubner, *Silicon Processing for the VLSI era. Vol. I: Process Technology*. (Lattice Press, Sunset Beach , California, 1986).
- [77] W. C. O'Mara, R. B. Herring, and L. P. Hunt, *Handbook of Semiconductor Silicon Technology*. (Noyes Publications, Park Ridge, New Jersey, 1990).
- [78] D. K. Fork, G. B. Anderson, J. B. Boyce, R. I. Johnson, and P. Mei, *Appl. Phys. Lett.* **68**, 2138 (1996).
- [79] W. Bollmann, *Crystal Defects and Crystalline Interfaces*. (Springer, Berlin, 1970).
- [80] D. C. Creagh and J. H. Hubbel, in *International Tables for Crystallography, Vol. C*, edited by A. J. C. Wilson, (Kluwer, Boston, 1992), p. 189.
- [81] M. Birkholz, S. Fiechter, A. Hartmann, and H. Tributsch, *Phys. Rev. B* **43**, 11 926 (1991).
- [82] Natl. Bur. Stand. (US), Monogr. **13**, 35 (1976).
- [83] R. Cerny and P. Prikryl, *Phys. Rev. B* **57**, 194 (1998).
- [84] P. Lengsfeld, S. Christiansen, M. Nerding, N. H. Nickel, W. Henrion, M. Rebien, I. Sieber, and N. H. Nickel, in *Polycrystalline Semiconductors VI-Bulk*

- Materials, Thin Films, and Devices*, edited by O. Bonnaud, T. Mohammed-Brahim, H. P. Strunk, and J. H. Werner, (Scitech. Publ., Üttikon am See, Switzerland, in the press), .
- [85] G. A. Slack, *J. Appl. Phys.* **35**, 3460 (1964).
- [86] N. H. Nickel, P. Lengsfeld, and I. Sieber, *Phys. Rev. B* **61**, 15 558 (2000).
- [87] K. Zellama, L. Chahed, P. Sládek, M. L. Thèye, J. H. von Bardeleben, and P. Roca i Cabarrocas, *Phys. Rev. B* **53**, 3804 (1996).
- [88] M. H. Brodsky, M. Cardona, and J. J. Cuomo, *Phys. Rev. B* **16**, 3556 (1977).
- [89] H. Wagner and W. Beyer, *Solid State Comm.* **48**, 585 (1983).
- [90] C. Manfredotti, F. Fizzotti, M. Boero, P. Pastorino, P. Polesello, and E. Vittone, *Phys. Rev. B* **50**, 18 046 (1994).
- [91] W. Beyer, in *Hydrogen in Semiconductors II*, edited by N. H. Nickel, (Academic Press, San Diego, 1999), p. 165.
- [92] A. A. Langford, M. L. Fleet, B. P. Nelson, W. A. Lanford, and N. Maley, *Phys. Rev. B* **45**, 13 367 (1992).
- [93] J. C. Knights, G. Lucovsky, and R. J. Nemanich, *Philos. Mag. B* **37**, 469 (1978).
- [94] W. Beyer, in *Tetrahedrally Bonded Amorphous Semiconductors*, edited by D. Adler and H. Fritzsche, (Plenum Press, New York, 1985), p. 129.
- [95] W. Beyer and H. Wagner, *J. Appl. Phys.* **53**, 8745 (1982).
- [96] W. B. Jackson and S. B. Zhang, in *Transport, Correlation and Structural Defects*, edited by H. Fritzsche, (World Scientific, Singapore, 1990), p. 63.
- [97] H. J. Stein, *J. Electron. Mater.* **4**, 159 (1975).
- [98] N. M. Johnson, *Phys. Rev. B* **31**, 5525 (1985).
- [99] N. H. Nickel and P. Lengsfeld, *Mater. Res. Soc. Symp. Proc.* (2000).
- [100] H. Tourir, K. Zellama, and J.-F. Morhange, *Phys. Rev. B* **59**, 10 076 (1998).
- [101] G. Amato, G. Della Mea, F. Fizzotti, C. Manfredotti, R. Marchisio, and A. Paccagnella, *Phys. Rev. B* **43**, 6627 (1991).

-
- [102] K. K. Gleason, M. A. Petrich, and J. A. Reimer, *Phys. Rev. B* **36**, 3259 (1987).
- [103] N. H. Nickel, G. B. Anderson, N. M. Johnson, and J. Walker, *Phys. Rev. B* **62**, 8012 (2000).
- [104] N. M. Johnson, C. Herring, C. Doland, J. Walker, G. B. Anderson, and F. Ponce, *Mater. Science Forum* **83-87**, 33 (1992).
- [105] W. B. Jackson, P. V. Santos, and C. C. Tsai, *Phys. Rev. B* **47**, 9993 (1993).
- [106] K. J. Chang and D. J. Chadi, *Phys. Rev. Lett.* **62**, 937 (1989).
- [107] C. G. Van de Walle, *Phys. Rev. B* **49**, 4579 (1994).
- [108] I. L. F. Ray and D. J. H. Cockayne, *Proc. Roy. Soc.* **A325**, 543 (1971).
- [109] H. Gottschalk, G. Patzer, and H. Alexander, *phys. stat. sol. (a)* **45**, 207 (1978).
- [110] S. Takeuchi and K. Suzuki, *phys. stat. sol. (a)* **171**, 99 (1999).
- [111] B. Cunningham, H. P. Strunk, and D. G. Ast, *Appl. Phys. Lett.* **40**, 237 (1982).
- [112] Results of the group of Prof. Strunk from the university of Erlangen-Nürnberg. The specimen have been provided by G. Andrä, IPHT Jena, J. H. Werner, IHP Stuttgart, M. Geiger, Bayerisches Laserzentrum, P. V. Santos, PDI Berlin, and Ch. Nebel, WSI Munich (all towns in Germany).
- [113] G. Aichmaier, D. Toet, M. Mulato, P. V. Santos, A. Spangenberg, S. Christiansen, M. Albrecht, and H. P. Strunk, *J. Appl. Phys.* **85**, 4010 (1999).
- [114] S. Christiansen, P. Lengsfeld, J. Krinke, M. Nerding, N. H. Nickel, and H. P. Strunk, *J. Appl. Phys.* **89**, 5348 (2001).
- [115] J. H. Werner, in *Structure and Properties of Dislocations in Semiconductors*, edited by S. G. Roberts, (Institute of Physics, Bristol, 1989), p. 63.
- [116] T. Serikawa, *IEEE Trans. Electron Devices* **36**, 1929 (1989).
- [117] A. Voigt, *Blockgeossenes Silizium für die Photovoltaik: Struktur und elektrische eigenschaften von Defekten*. (Lehrstuhl für Mikrocharakterisierung Friedrich-Alexander-Universität Erlangen-Nürnberg, Erlangen, 1996).
- [118] A. Bary, B. Thercey, G. Poullain, J. L. Chermant, and G. Nouet, *Revue Phys. Appl.* **22**, 597 (1987).

-
- [119] L. Haji, P. Joubert, J. Stoemenos, and N. A. Economou, *J. Appl. Phys.* **75**, 3944 (1994).
- [120] S. Loreti, M. Vittori, L. Mariucci, and G. Fortunato, *Solid State Phenomena* **67-68**, 181 (1999).
- [121] N. Sridhar, D. D. L. Chung, W. A. Anderson, and J. Coleman, *J. Appl. Phys.* **79**, 1569 (1996).
- [122] H. Kakinuma, *J. Vac. Sci. Technol. A* **13**, 2310 (1995).
- [123] L. Csepregi, E. F. Kennedy, J. W. Mayer, and T. M. Sigmon, *J. Appl. Phys.* **49**, 3906 (1978).
- [124] T. A. Wagner, L. Oberbeck, R. B. Bergmann, and J. H. Werner, in *Polycrystalline Semiconductors VI-Bulk Materials, Thin Films, and Devices*, edited by O. Bonnaud, T. Mohammed-Brahim, H. P. Strunk, and J. H. Werner, (Scitech Publ., Üttikon am See, Switzerland, in the press), .
- [125] M. Cardona and F. H. Pollak, *Phys. Rev.* **142**, 530 (1966).
- [126] M. Jouanne and R. Beserman, *Solid State Commun.* **16**, 1047 (1975).
- [127] M. Chandrasekhar, M. Cardona, and E. O. Kane, *Phys. Rev. B* **16**, 3579 (1977).
- [128] M. Chandrasekhar, U. Rössler, and M. Cardona, *Phys. Rev. B* **22**, 761 (1980).
- [129] C. Thomson, in *Light Scattering in Solids IV*, edited by M. Cardona and G. Güntherodt, (Springer-Verlag, Berlin, 1991), p. 306.
- [130] G. Piao, R. A. Lewis, and P. Fisher, *Solid State Commun.* **75**, 835 (1990).
- [131] M. Cardona, F. Cerdeira, and T. A. Fjeldly, *Phys. Rev. B* **10**, 859 (1974).
- [132] S. Brehme, P. Kanschä, K. Lips, I. Sieber, and W. Fuhs, *Mat. Sci. Eng. B* **69-70**, 232 (2000).
- [133] P. Kanschä, Ph.D.-Thesis, Marburg, Germany (2000).

List of abbreviations and symbols

a-Si	Amorphous silicon
a-Si:H	Hydrogenated amorphous silicon
AFM	Atomic force microscope
B	Boron
c-Si	Crystalline silicon
CS-TEM	Cross-section TEM
CSL	Coincidence site lattice
CVD	Chemical vapor deposition
EBSP	Electron backscattering pattern
H	Hydrogen
P	Phosphorous
PECVD	Plasma enhanced CVD
Poly-Si	Polycrystalline silicon
SEM	Scanning electron microscopy
SIMS	Secondary-ion mass spectroscopy
SLG	Super lateral growth
SPC	Solid phase crystallization
TEM	Transmission electron microscopy
TFT	Thin film transistor
TRR	Time resolved reflectivity
XRD	X-ray diffraction

$\mu\text{c-Si}$	Microcrystalline silicon
$\mu\text{c-Si:H}$	Hydrogenated microcrystalline silicon
c_{H}	Concentration of hydrogen (cm^{-3})
d_{P}	Penetration depth (nm)
E_{L}	Laser fluence (mJ/cm^2)
E_{T}	Threshold laser fluence of crystallization (mJ/cm^2)
E_{SLG}	Laser fluence to achieve super lateral growth (mJ/cm^2)
n (p)	Concentration of free electrons (holes) (cm^{-3})
R	Reflectivity
R^*	Microstructure parameter
$\langle x \rangle$	Average grain size (nm)
X_{C}	Crystallinity (%)
α	Absorption coefficient (cm^{-1})
α_{th}	Thermal expansion coefficient (K^{-1})
λ	Wavelength (nm)
μ_{H}	Hall mobility (cm^2/Vs)
σ	Conductivity (S/cm)
σ_{th}	Thermal stress
τ	Laser pulse width (ns)
ω	Raman shift (cm^{-1})
ω_{L}	Wavelength of Raman laser (nm or eV)
$\omega_{\text{LO-TO}}$	Raman shift of LO-TO phonon line (cm^{-1})

Acknowledgments

I would like to thank Prof. W. Fuhs from the Hahn-Meitner-Institut, Berlin for the possibility to conduct the research in his group, for his constant support during my time at the HMI, and during the time I wrote this thesis. Thanks are due to the two professors who enabled me to present this thesis at the TU Berlin: Prof. D. Zimmermann who chaired my disputation and Prof. W. Richter who accepted to referee this work. My very special thanks go to Dr. N. H. Nickel, my guide and adviser in the complicated field of disordered thin film silicon. It was a great time working together!

I would like to thank all my colleagues from the HMI in Adlershof for the pleasant and fruitful working atmosphere. Especially, I thank Dr. J. Schwarzkopf for her constant interest in the work, helpful discussions and a critical reading of the manuscript. I thank H. Heise for being a wonderful roommate and that she always lend me a helping hand, in case of need. J. Krause and E. Conrad supported me in deposition matters and prepared some films for this work. For the same reason I would like to thank P. Reinig and S. von Aichberger (HMI Wannsee), Dr. H. Mell (University of Marburg), as well as CIS Erfurt and Dr. M. Schmidt. Thanks are due to G. Andrä from the IPHT Jena for supplying me with two interesting samples at short notice.

I would like to acknowledge the intensive and fruitful cooperation with the group of Prof. H. P. Strunk at the university of Erlangen. Dr. S. Christiansen and M. Nerding contributed very important TEM, CS-TEM and EBSP measurements to this work. Three CS-TEM measurements were also carried out at the Labor für Elektronenmikroskopie in Halle (Saale).

Many thanks go to I. Sieber for the exhaustive SEM measurements. I thank R. Würz for the AFM measurements and Dr. S. Brehme for some of the Hall measurements. I'm indebted to Dr. W. Henrion and M. Rebien for optical measurements. Dr. M. Birkholz and H.-J. Muffler helped me carrying out the XRD measurements. Dr. T. Dittrich and Dr. J. Rappich added the *in situ* TRR setup to the laser crystallization apparatus. Dr. L. Elstner carried out the solar cell characterization.

I would like to thank U. Mazur, G. Keiler, M. Schmidt, K. Jacob, H. Mai, D. Patzek, G. Winkler, and R. Linke for technical support. I would like to thank C. Schulze for his invaluable help in all matters of organization and purchasing of equipment. K. Brendel and C. Matthäus helped me to remove spelling mistakes and form errors from this manuscript.

Above all I thank my wife Martina for her constant support during the last three years. My daughter Therese and my son Ferdinand, who only arrived in the course of my time at the HMI, were a constant source of joy for me.

List of Publications

Some of the results presented in this work have been or will be published in scientific journals. These publications are listed below.

- P. Lengsfeld, N. H. Nickel, and W. Fuhs, "Step-by-step excimer laser induced crystallization of a -Si:H" *Appl. Phys. Lett.* **76**, 1680 (2000).
- P. Lengsfeld, N. H. Nickel, and W. Fuhs, "The role of hydrogen in the process of successive laser crystallization of hydrogenated amorphous silicon", *J. Non-Cryst. Solids* **266-269**, 659 (2000).
- P. Lengsfeld, S. Christiansen, M. Nerding, N. H. Nickel, W. Henrion, M. Rebien, I. Sieber, and N. H. Nickel, "Excimer laser crystallization of doped and undoped a -Si:H for solar cells", in *Polycrystalline Semiconductors VI-Bulk Materials, Thin Films, and Devices*, edited by O. Bonnaud, T. Mohammed-Brahim, H. P. Strunk, J. H. Werner, (Scitech. Publ., Üttikon am See, Switzerland, in the press).
- N. H. Nickel, P. Lengsfeld, and I. Sieber, "Raman spectroscopy of heavily doped polycrystalline silicon thin films", *Phys. Rev. B*, **61**, 15 558 (2000).
- S. Christiansen, P. Lengsfeld, M. Nerding, J. Krinke, M. Nerding, N. H. Nickel, and H. P. Strunk, "The Nature of Grain Boundaries in laser crystallized polycrystalline silicon thin films", *J. Appl. Phys.* **89**, 5348 (2001).
- N. H. Nickel and P. Lengsfeld, "The influence of the Fermi Energy on Si-H Vibrational Modes in Amorphous and Microcrystalline Silicon", *Mater. Res. Soc. Symp. Proc.* (2000).